



Theory of parametrically amplified electron-phonon superconductivity

Mehrtash Babadi,^{1,2,*} Michael Knap,³ Ivar Martin,⁴ Gil Refael,¹ and Eugene Demler⁵

¹*Institute for Quantum Information and Matter, Caltech, Pasadena, California 91125, USA*

²*Broad Institute of MIT and Harvard, Cambridge, Massachusetts 02138, USA*

³*Department of Physics, Walter Schottky Institute, and Institute for Advanced Study, Technical University of Munich, 85748 Garching, Germany*

⁴*Materials Science Division, Argonne National Laboratory, Argonne, Illinois 60439, USA*

⁵*Department of Physics, Harvard University, Cambridge, Massachusetts 02138, USA*

(Received 11 April 2017; published 19 July 2017)

Ultrafast optical manipulation of ordered phases in strongly correlated materials is a topic of significant theoretical, experimental, and technological interest. Inspired by a recent experiment on light-induced superconductivity in fullerenes [M. Mitrano *et al.*, *Nature (London)* **530**, 461 (2016)], we develop a comprehensive theory of light-induced superconductivity in driven electron-phonon systems with lattice nonlinearities. In analogy with the operation of parametric amplifiers, we show how the interplay between the external drive and lattice nonlinearities lead to significantly enhanced effective electron-phonon couplings. We provide a detailed and unbiased study of the nonequilibrium dynamics of the driven system using the real-time Green's function technique. To this end, we develop a Floquet generalization of the Migdal-Eliashberg theory and derive a numerically tractable set of quantum Floquet-Boltzmann kinetic equations for the coupled electron-phonon system. We study the role of parametric phonon generation and electronic heating in destroying the transient superconducting state. Finally, we predict the transient formation of electronic Floquet bands in time- and angle-resolved photoemission spectroscopy experiments as a consequence of the proposed mechanism.

DOI: [10.1103/PhysRevB.96.014512](https://doi.org/10.1103/PhysRevB.96.014512)

I. INTRODUCTION

In recent years, the rapid progress of the field of ultrafast pump-probe spectroscopy experiments has enabled an unprecedented exploration of many-body quantum dynamics in far-from-equilibrium states (for reviews, see Refs. [1,2]). The application of strong ultrafast laser pulses can dramatically alter the equilibrium state, outreach the linear response regime, and enable the induction of novel ordered states and stimulation of phase transitions via transient nonequilibrium states.

One of the main motivations behind these experiments is to shed light on the interplay between competing orders in strongly correlated superconductors, along with the tantalizing outlook of stimulating the superconducting transition at temperatures above the critical temperature T_c . An early experimental evidence proving the possibility of stimulating superconductivity via external fields is the Wyatt-Dayem effect [3,4], where microwave radiation of superconducting microbridges in the MHz to GHz frequency range was found to increase T_c by a few percent. This effect was explained theoretically by Eliashberg [5] on the basis of the nonequilibrium shift of the quasiparticle occupation to high energies. Subsequent theoretical work [6] and experiments in double-barrier tunnel junctions and strips [7–10] found a much larger effect up to several times larger than the equilibrium T_c . An experimental proposal for investigating this effect using ultracold fermionic atoms has also been given [11].

Recently, Mitrano *et al.* [12] have reported a large increase in carrier mobility and the opening of an optical gap upon stimulating the intercalated fullerene superconductor K_3C_{60} with a femtosecond mid-infrared light pulse in the frequency range 80–200 meV (19–48 THz). These effects persist for

several picoseconds after pumping, and remarkably for initial temperatures up to $T_i \sim 100$ K, much higher than the equilibrium $T_c \sim 20$ K, providing a compelling evidence for a possibly light-induced superconducting state. The experimentally observed resonance with several C_{60} vibrational modes suggests that the underlying mechanism for enhanced Cooper pairing in this experiment stems from lattice distortions and is distinct from the Wyatt-Dayem effect.

The application of a strong pump pulse alters the initial equilibrium state in various ways and is a complex function of the strength of the drive, strength of coupling to different degrees of freedom, and energetic proximity to resonances. The accurate theoretical modeling of light-stimulated superconductivity in K_3C_{60} is exacerbated by the structural complexity of K_3C_{60} , including the threefold degeneracy of the conduction t_{1u} bands and their coupling to eight H_g intramolecular Jahn-Teller phonons [13], strong electron-phonon coupling $\lambda \sim 0.5–1$, narrow conduction band $\omega_{ph}/W_{el} \sim 0.1–0.25$ (ω_{ph} is the typical phonon energy scale and W_{el} is the conduction bandwidth), and strong Coulomb interaction $U_c/W_{el} \sim 1.5–2.5$ [14]. A reliable material-specific analysis must combine state-of-the-art *ab initio* modeling including nonlinear interactions and beyond-Migdal vertex corrections [15] into the framework of nonequilibrium field theory. We do not pursue this formidable goal here; rather, *inspired* by the experiment and embracing the Occam's razor tradition, we explore a simplified model with fairly generic electron-phonon interaction which retains the essential features observed in experiments with light-stimulated superconductivity in K_3C_{60} .

At the simplest level, the pumping pulse with frequency $\Omega_{drv} \sim 100$ meV strongly drives near-resonant infrared (IR) active lattice vibrational mode, such as T_{1u} modes in fullerenes. As a first approximation, one may average out fast oscillations at the scale of Ω_{drv}^{-1} . The presence of lattice anharmonicities

*Corresponding author: mehrtash@broadinstitute.org

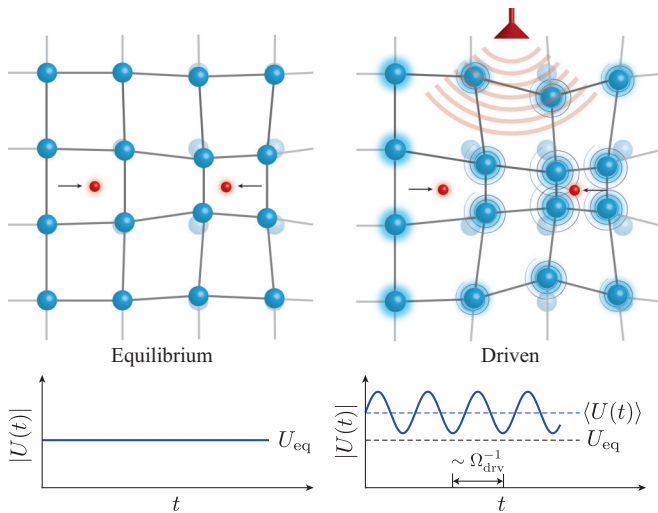


FIG. 1. Parametric amplification of the phonon response. (Left) Phonon-mediated electron attraction in the absence of external drive. (Right) The external drive and lattice nonlinearities parametrically amplify lattice distortions which in turn mediate stronger attraction between the electrons.

and nonlinear coupling between vibrational modes results in the expansion and contraction of time-averaged lattice constants and electronic orbital configurations. The time-averaged electron-phonon coupling constants and electronic density of states are consequently renormalized. This approach is adopted in Ref. [12] where an *ab initio* analysis in the static “frozen-phonon” approximation is performed and it is shown that time-averaged lattice deformations exhibit a favorable trend toward increasing T_c .

In this paper, we aim to show that the implications of a strong periodic drive and its interplay with lattice nonlinearities reaches beyond statically renormalized model parameters. In fact, we will show that the mechanism which yields the most striking enhancement of electron-phonon coupling is purely dynamical in nature and is not described by time-averaged Hamiltonians.

The phonon-mediated electron-electron attraction U is usually understood using second-order perturbation theory: an electron distorts the lattice and the other electron is attracted to the lattice distortion [see Fig. 1 (left)]. In other words, this attractive potential is proportional to the retarded phonon response function. We will show that the enhancement of superconductivity in a driven nonlinear lattice is conceptually similar to the operation of a parametric amplifier circuit: the “nonlinear capacitor” is realized by the lattice nonlinearity, the “ac pump source” is realized by an excited lattice vibrational mode, the “input signal” is the phonon excitation caused by a momentum kick from an electron, and the “output signal” is the parametrically amplified phonon response observed by the other electron. In essence, lattice nonlinearities *convert* the coherent motion of the driven mode into a source of parametric drive for the phonon that couples to conduction electrons. When this drive is near parametric resonances, the retarded response will be significantly amplified, leading to a much stronger electron-electron attraction. Parametric driving also induces strong temporal oscillations in the effective electron-electron attraction, allowing it to visit very large values during

each cycle. We will show that such temporal oscillations can significantly enhance T_c even if the time-averaged attraction remains constant [see Figs. 1 (right) and 6].

A rigorous quantitative analysis of this simple mechanism and its consequences in a realistic electron-phonon model goes beyond the amplifier analogy as one must take into account several competing effects. Most importantly, the nearly resonant drive also results in parametric generation of high-energy phonons that dissipate their excess energy to electrons, leading to higher scattering rates and heating. It is not *a priori* clear which subset of these phenomena prevails, even for short times, without resorting to an unbiased and rigorous framework. Ultimately, we find that without an external cooling mechanism, Cooper pairing may only be enhanced for a short time similar to the experiments, and the normal state takes over as high-energy phonon excitations equilibrate their energy with electrons.

Our goal in this paper is twofold. First and foremost, we wish to present a transparent and physical analysis of the role of parametric resonances of the lattice in enhancing electron-phonon interactions and stimulating Cooper pair formation. The major part of this goal is achieved in the first part of the paper using perturbation theory, BCS theory, classical dynamics, along with a number of common-sense simplifications. Second, we aim to develop a rigorous theoretical formalism for analyzing the nonequilibrium dynamical nature of light-stimulated superconductivity experiments, a formalism that takes into account the detailed driven-dissipative evolution of phonons and heating of electrons while being flexible enough to include material-specific properties and paving the way for future investigations. To this end, we develop an extension of the Migdal-Eliashberg theory [16,17] to periodically driven electron-phonon systems with lattice nonlinearities, and utilize it to substantiate the results of the first part as an immediate application.

The conventional Migdal-Eliashberg theory is a cornerstone of the modern theory of superconductivity, both for qualitative understandings and accurate *ab initio* calculations. The existing attempts at the real-time extension of the Migdal-Eliashberg theory are known to be intractably difficult to work with due to the complicated temporal structure of the equations [18–20]. Here, we combine ideas from effective actions, Floquet theory, dynamical mean-field theory, and quantum kinetic theory to develop a formalism that is well suited for numerical and analytical studies of periodically driven systems. The Floquet quantum kinetic formalism trades fast drive-induced oscillations of nonequilibrium propagators with slowly varying Floquet components, and memory convolution integrals with algebraic products along with derivative corrections [21–24]. These controlled approximations effectively reduce the two-time Kadanoff-Baym integrodifferential equations [25] to (implicit) ordinary differential equations which are much easier to solve numerically. The extension of the quantum kinetic formalism to periodically driven systems has been considered before in Ref. [24] in a different context and in the Boltzmann “quasiparticle” approximation. The latter is obtained by neglecting off-shell processes [26,27]. We do not adopt this approximation here. As we pointed out earlier, suppression of electronic and phononic quasiparticle coherence is an important factor in the analysis of transient superconductivity. Hence, a detailed study of the changes in the spectral functions of Floquet quasiparticles will be an important ingredient of our theory.

The experimental observation of the light-induced superconducting state in K_3C_{60} [12] has inspired several theoretical works. Sentef *et al.* [20] have studied the transient dynamics of the superconducting gap following a change in the coupling constants. In an earlier work, we outlined the role of parametric driving in enhancing the electron-phonon coupling [28] and analyzed the problem using a Floquet extension of the BCS theory. Komnik *et al.* [29] have recently worked out a similar BCS framework using a more concise analytical approach. More recently, Kennes *et al.* [30] have suggested nonlinear electron-phonon couplings as another plausible source of enhancing T_c in a highly pumped state. The model is also studied in a nonequilibrium setting in Ref. [31]. Last but not least, Kim *et al.* [32] have suggested light-induced changes in the screened Coulomb matrix elements as a factor for enhancing superconductivity in intercalated fullerenes. We would like to mention that none of these works, except for Ref. [28], have studied the role of undesirable competing factors within their respective models. The electrons are always assumed to remain in the initial thermal state and heating is ignored. Given that superconductivity in fullerenes is mediated by high-frequency optical phonons, the issue of heating is a crucial aspect of the phenomenology even for short times. Another important goal of our paper is to provide a first complete and unbiased analysis of the competition between processes that enhance and suppress Cooper pairing.

Finally, we would like to emphasize that the parametric amplification of electron-phonon coupling is not limited to enhancing Cooper pairing and is expected to find similar applications to other systems. For example, the same framework can be employed to study the recently observed enhancement of electron-phonon coupling in periodically distorted graphene [33] and driven optomechanical cavities [34–37].

Organization of the paper

This paper is organized as follows. We describe the model in Sec. II as the first step, and present its analysis in two separate stages. Before delving into the detailed formalism, we give a more intuitive account using perturbation theory, classical dynamics, and the BCS theory to demonstrate the idea of parametric amplification in nonlinear lattices and its implications in Sec. III. Many of the relevant details such as feedback to electrons, heating, and competing factors are left to the second stage.

Section IV and its multiple subsections are dedicated to developing the formalism of Floquet-Migdal-Eliashberg quantum kinetics. In particular, a pairing instability criterion is derived in Sec. V that generalizes the result of Scalapino, Schrieffer, and Wilkins [38] to quasisteady Floquet states. As a first application of the formalism, we study the stationary solutions of the driven-dissipative state of phonons while neglecting the heating of electrons. This allows us to gain insight about the parameter regimes of maximal electron-phonon coupling enhancement, and to study the role of individual factors in enhancing and suppressing Cooper pairing. We move on the fully nonequilibrium scenario in Sec. VI B where we discuss the dynamics of the coupled electron-phonon system and show that a window of transient superconducting instability can exist even if the heating of electrons is taken into account. Finally, we use our theory to make additional

experimental predictions in Sec. VI C, in particular, the dynamical formation of Floquet conduction bands which can be probed using time- and angle-resolved photoemission spectroscopy (tr-ARPES). The experimental observation of electronic Floquet bands provides strong evidence for the role of coherent driving in enhancing Cooper pairing as opposed to explanations based on incoherent excitations.

Some of the technical details, in particular those pertaining to numerical methods, have been moved to the Appendices. The Appendices also include an extensive discussion of the role of electrons in generating phonon nonlinearities (see Appendix E). In particular, we show that the magnitude of electron-mediated phonon nonlinearities increases near parametric resonances and can make a significant contribution to intrinsic lattice nonlinearities.

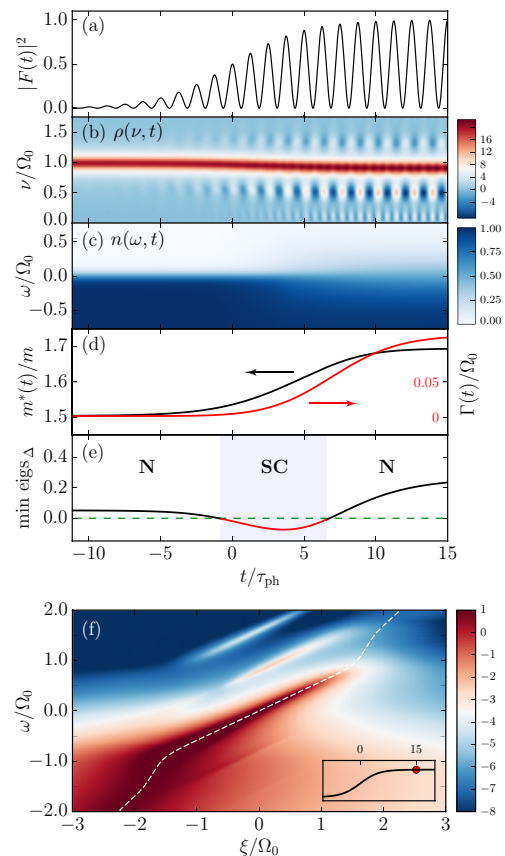


FIG. 2. Nonequilibrium evolution of the driven electron-phonon system obtain using the Floquet-Migdal-Eliashberg formalism. (a) Intensity of the external drive, (b) phonon spectral function $\rho(v, t)$, showing the red-shift of the phonon peak and along with emergent oscillatory features, (c) electron distribution $n(\omega, t)$ showing the smearing of the Fermi surface as the electrons heat up, (d) electron effective mass (black, left axis) and damping (red, right axis), (e) lowest eigenvalue of the Floquet-Migdal-Eliashberg gap functional, where N and SC correspond to normal conducting and superconducting (instability) intervals, (f) predicted time-resolved ARPES signal in the log scale as a function of electron frequency ω and kinetic energy ξ at $t = 15 \tau_{\text{ph}}$, showing the formation of electronic Floquet bands. The initial temperature is $T_i = 0.04 \Omega_0$, the lattice nonlinearity is cubic type with $\kappa_3 = 0.1 \Omega_0$, and the drive frequency and amplitudes are $\Omega_{\text{drv}} = 0.4 \Omega_0$ and $\mathcal{A} = 0.75$ (refer to Sec. VI for additional details).

Finally, Fig. 2 shows a summary of the nonequilibrium dynamics obtained from the Floquet-Migdal-Eliashberg formalism; refer to the figure caption for details.

II. MODEL

We start with a general model for conduction electrons and a single-phonon branch, along with an external drive that couples to the uniform lattice displacement, a local nonlinear lattice potential, and a linear electron-phonon coupling. The Lagrangian for this system is given as

$$\begin{aligned} \mathcal{L}[\varphi, \Psi](t) &= \sum_{\mathbf{k}} \Psi_{\mathbf{k}}^\dagger (i \partial_t \mathbb{I} - \xi_{\mathbf{k}} \hat{\sigma}_3) \Psi_{\mathbf{k}} \\ &\quad - \frac{1}{2} \sum_{\mathbf{q}} \frac{1}{2\omega_{\mathbf{q}}} \varphi_{\mathbf{q}} (\partial_t^2 + \omega_{\mathbf{q}}^2) \varphi_{-\mathbf{q}} - \sum_{j \in \text{lattice}} \mathcal{V}^{\text{ph}}(\varphi_j) \\ &\quad - \frac{1}{\sqrt{N}} \sum_{\mathbf{k}, \mathbf{k}'} g_{\mathbf{k}, \mathbf{k}'} \varphi_{\mathbf{k}-\mathbf{k}'} \Psi_{\mathbf{k}}^\dagger \hat{\sigma}_3 \Psi_{\mathbf{k}} + \frac{\Lambda}{2} |F(t)|^2 \sum_{j \in \text{lattice}} \varphi_j. \end{aligned} \quad (1)$$

Here, $\Psi_{\mathbf{k}} = (c_{\mathbf{k}\uparrow}, c_{-\mathbf{k}\downarrow}^\dagger)^T$ is the Nambu spinor of the conduction electrons, $\xi_{\mathbf{k}}$ is the electron dispersion, $\varphi_{\mathbf{q}} \equiv b_{\mathbf{q}}^\dagger + b_{-\mathbf{q}} = \sum_j e^{-i\mathbf{q}\cdot\mathbf{R}_j} \varphi_j / \sqrt{N}$ is the lattice displacement operator, $\omega_{\mathbf{q}}$ is the phonon dispersion, and $g_{\mathbf{k}, \mathbf{k}'}$ is the linear electron-phonon coupling constant. Furthermore, $\mathcal{V}^{\text{ph}}(\varphi)$ is the local lattice anharmonic potential which, for low-amplitude deformations, can be modeled as

$$\mathcal{V}^{\text{ph}}(\varphi) = -\frac{\kappa_3}{3!} \varphi^3 - \frac{\kappa_4}{4!} \varphi^4. \quad (2)$$

We assume $\kappa_4 > 0$ since the lattice potential generically softens for large deformations. The sign of κ_3 is inconsequential due to symmetries. We neglect Coulomb interaction to simplify the analysis. We will briefly comment on its effect later on and argue that it does not play a consequential role in the phenomenon that is the case here. Finally, $F(t)$ is the external classical drive that couples to the uniform $\mathbf{q} = 0$ lattice displacement with strength $\Lambda/2$.

A. Origin of the drive term

The generic model we introduced in Eq. (1) is compatible with several scenarios suggested for modeling the role of the drive in pump-probe experiments of different materials. If φ describes a polarizable (IR-active) phonon, $F(t)$ can be directly identified with the external electric field, in which case, the coupling strength Λ will be proportional to the polarizability of φ . On the other hand, if φ is a nonpolarizable (Raman-active) phonon, even though the incident light does not directly influence it through dipole coupling, the classical drive term can still be obtained via nonlinear coupling to a driven ‘‘proxy’’ IR-active phonon. The leading-order nonlinear IR/Raman coupling allowed by symmetries is the cubic $\propto \varphi_{\text{IR}}^2 \varphi$ interaction. In this case, we can identify $F(t) \sim \langle \varphi_{\text{IR}}(t) \rangle$ as the coherent oscillations of the driven IR-active mode and Λ as the strength of the cubic coupling to the Raman phonon φ .

Regardless of the origin of the classical drive, we assume

$$F(t) = F_{\text{env}}(t) \cos(\Omega_{\text{drv}} t), \quad (3)$$

where Ω_{drv} is the principal frequency of the classical drive and $F_{\text{env}}(t)$ is its slowly varying envelope. Note that the classical drive couples to φ in intensity $|F(t)|^2$, such that the effective principal drive frequency is $2\Omega_{\text{drv}}$.

If the drive term originates from nonlinear coupling to an IR-active phonon, Ω_{drv} may no longer be identified with the frequency of the incident light after the pump pulse is ramped down; rather, the pump pulse coherently drives the proxy IR-active phonon out of its equilibrium position and, subsequently, the coupled IR-active and Raman phonons oscillate together at a frequency predominantly determined by the IR-active mode. The proposed model still applies to this case with the appropriate choice of Ω_{drv} .

B. Different routes to parametric driving

For the purposes of this work, the necessary ingredient of the model is a mechanism to achieve parametric driving of the φ phonon, i.e., a route for achieving the effective substitution $\omega_{\mathbf{q}}^2 \rightarrow \omega_{\mathbf{q}}^2 [1 + 2\alpha_{\mathbf{q}} \cos(2\Omega_{\text{drv}} t)]$, where $\alpha_{\mathbf{q}}$ is the effective parametric driving amplitude. In the model proposed in Sec. II, this is achieved from the interplay between the nonlinearities of the φ phonon and its own coherent displacement, as further explained in the next section. There exists, however, a multitude of other physically realizable routes that all lead to parametric driving. This situation closely resembles the multitude of architectures proposed for building electronic parametric amplifiers over the years using elements such as variable capacitance diodes, nonlinear inductors, and Josephson junctions. The common theme remains the same: the interplay between pumping and nonlinear elements.

The strong pumping of a material with a complex crystal structure will induce coherent oscillations in a few primary modes. These oscillations trickle down to several other modes as a result of nonlinear couplings. Thus, *every* symmetry-allowed mode will be parametrically driven to a degree with strong enough pumping. With this understanding, the model proposed here is only one out of the numerous possible other routes to achieve parametric driving. For instance, the symmetry-allowed quartic coupling in fulleride superconductors $\sim \varphi_{\text{IR}}^2 \varphi^2$ directly translates the coherent motion of φ_{IR} to a parametric drive for φ . Here, φ_{IR} is one of the IR-active modes of C_{60} such as $T_{1u}(1-4)$, and φ is a Raman-active mode such as Hg(7-8) that couples strongly to conduction electrons [12,39]. Even though achieving parametric driving is material specific, it leads to the same qualitative physics. This paper mainly deals with the universal consequences of parametric driving.

III. PARAMETRIC AMPLIFICATION OF PHONON-MEDIATED ELECTRON-ELECTRON ATTRACTION: A FIRST LOOK

Our goal in this section is to demonstrate the resonant amplification of the electron-phonon coupling in the presence of the drive. For the time being, we neglect the complex epiphenomena such as the nonequilibrium evolution of electrons,

phonon dissipation and retardation, and the feedback between electrons and phonons. Instead, we resort to a perturbative treatment and elementary methods in order to elucidate the main ideas. We will revisit the problem again in a later section and provide a comprehensive account using the nonequilibrium Migdal-Eliashberg theory. The latter treatment is naturally more cumbersome than the physical account given in this section. The present analysis serves as a guideline to identify and interpret the results of the upcoming detailed analysis.

As a first step, we assume that the lattice nonlinearity $\mathcal{V}(\varphi)$ and the electron-phonon coupling $g_{\mathbf{k},\mathbf{k}'}$ are both weak compared to the drive, such that we can study the coherent motion of the lattice in isolation. The classical equation of motion for $\langle \hat{\varphi}_0(t) \rangle$ (the $\mathbf{q} = 0$ mode) is easily found as

$$\partial_t^2 \langle \hat{\varphi}_0(t) \rangle + \omega_0^2 \langle \hat{\varphi}_0(t) \rangle = \frac{\Lambda \omega_0}{2} \sqrt{N} F_{\text{env}}^2(t) \cos^2(\Omega_{\text{drv}} t). \quad (4)$$

The normalization constant \sqrt{N} results from the definition of the Fourier operators given earlier, i.e., $\langle \hat{\varphi}_0 \rangle = \sqrt{N} \langle \hat{\varphi}_j \rangle$ where $\langle \hat{\varphi} \rangle$ is the coordinate of an arbitrary single ion j . We assume that the temporal variation scale of $F_{\text{env}}(t)$ is much longer than the drive period. Thus, for an adiabatically ramped up $F_{\text{env}}(t)$, we find

$$\begin{aligned} \langle \hat{\varphi}_0(t) \rangle &\approx \frac{\Lambda \sqrt{N}}{4\omega_0} F_{\text{env}}^2(t) + \frac{\Lambda \sqrt{N} \omega_0}{4(\omega_0^2 - 4\Omega_{\text{drv}}^2)} \\ &\times F_{\text{env}}^2(t) \cos(2\Omega_{\text{drv}} t). \end{aligned} \quad (5)$$

Near the resonance $\Omega_{\text{drv}} = \omega_0/2$, the oscillatory term dominates the dc term in amplitude. The precise values of the prefactors of the dc and ac terms are not important for the present discussion and in a more realistic setting, both get corrections from phonon damping, nonlinearities, etc. Quite generally, though, we have $\langle \hat{\varphi}_0(t) \rangle \approx \sqrt{N} \varphi_0(t) + \sqrt{N} \varphi_1(t) \cos(2\Omega_{\text{drv}} t)$ where $\varphi_0(t)$ and $\varphi_1(t)$ are slowly varying functions of time. With this understanding, we drop the time labels from φ_0 and φ_1 hereafter and treat them as given quasisteady parameters.

The local lattice nonlinearity terms couple the coherent uniform motion of the lattice to $\pm \mathbf{q}$ modes. For instance, the leading-order correction resulting from the cubic nonlinearity $\sim \varphi^3$ is found by replacing one of the operators with $\langle \hat{\varphi}_0(t) \rangle$. Momentum conservation implies opposite momenta for the remaining two operators:

$$-\frac{\kappa_3}{3!} \sum_{j \in \text{lattice}} \hat{\varphi}_j^3 \rightarrow -\frac{\kappa_3}{2} [\varphi_0 + \varphi_1 \cos(2\Omega_{\text{drv}} t)] \sum_{\mathbf{q} \neq 0} \hat{\varphi}_{\mathbf{q}} \hat{\varphi}_{-\mathbf{q}}. \quad (6)$$

Likewise, the leading-order contribution from the quartic nonlinearity is found by replacing two of the operators with $\mathbf{q} = 0$, which yields

$$-\frac{\kappa_4}{4!} \sum_{j \in \text{lattice}} \hat{\varphi}_j^4 \rightarrow -\frac{\kappa_4}{4} [\varphi_0 + \varphi_1 \cos(2\Omega_{\text{drv}} t)]^2 \sum_{\mathbf{q} \neq 0} \hat{\varphi}_{\mathbf{q}} \hat{\varphi}_{-\mathbf{q}}. \quad (7)$$

The dc terms result in the renormalization of the phonon frequency, e.g., $\omega_{\mathbf{q}}^2 \rightarrow \omega_{\mathbf{q}}^2 - \kappa_3 \varphi_0/2$ for the cubic nonlinearity and $\omega_{\mathbf{q}}^2 \rightarrow \omega_{\mathbf{q}}^2 - \kappa_4(\varphi_0^2/4 + \varphi_1/8)$. Such corrections are precisely the time-averaged renormalized lattice properties that we discussed earlier in the Introduction and can enhance or suppress the effective electron-phonon coupling on their own account.

As we will show soon, the most intriguing effect is purely dynamical and stems from the ac term. We neglect the dc corrections for simplicity hereafter. At the present order in perturbation theory, only $\pm \mathbf{q}$ opposite momentum pairs couple and thus we may focus on a single momentum pair without the loss of generality. We also only consider the cubic nonlinearity. It will soon become apparent that both types of nonlinearity give rise to the same resonant amplification phenomenon. The Hamiltonian is given as $\hat{H}_{\pm \mathbf{q}}(t) = \hat{H}_e + \hat{H}_{p,\pm \mathbf{q}}(t) + \hat{H}_{ep,\pm \mathbf{q}}$, where $\hat{H}_e = \sum_{\mathbf{k},\sigma} \xi_{\mathbf{k}} c_{\mathbf{k},\sigma}^\dagger c_{\mathbf{k},\sigma}$ and

$$\begin{aligned} H_{p,\pm \mathbf{q}}(t) &= \frac{\hbar \omega_{\mathbf{q}}}{2} \hat{\varphi}_{\mathbf{q}} \hat{\varphi}_{-\mathbf{q}} + 2 \hbar \omega_{\mathbf{q}} \hat{\pi}_{\mathbf{q}} \hat{\pi}_{-\mathbf{q}} \\ &\quad - \kappa_3 \varphi_1 \cos(2\Omega_{\text{drv}} t) \hat{\varphi}_{\mathbf{q}} \hat{\varphi}_{-\mathbf{q}}, \\ H_{ep,\pm \mathbf{q}} &= g_{\mathbf{q}} \hat{\varphi}_{\mathbf{q}} \hat{\rho}_{-\mathbf{q}} + g_{-\mathbf{q}} \hat{\varphi}_{-\mathbf{q}} \hat{\rho}_{\mathbf{q}}, \end{aligned} \quad (8)$$

where $\hat{\pi}_{\mathbf{q}} = (b_{-\mathbf{q}} - b_{\mathbf{q}}^\dagger)/(2i)$ is the conjugate momentum to $\hat{\varphi}_{\mathbf{q}}$,¹ and $g_{\mathbf{q}}$ is the linear electron-phonon coupling constant (we have assumed $g_{\mathbf{k},\mathbf{k}'} \approx g_{\mathbf{k}-\mathbf{k}'}$).

Finally, $\rho_{\mathbf{q}} = \sum_{\mathbf{k},\sigma} c_{\mathbf{k}+\mathbf{q},\sigma}^\dagger c_{\mathbf{k},\sigma}$ is the electron charge density operator. The analysis can be further simplified by performing a canonical change of variables to standing wave phonon operators:

$$\begin{aligned} \hat{Q}_+ &= \sqrt{\frac{\hbar}{4M\omega_{\mathbf{q}}}} (\hat{\varphi}_{\mathbf{q}} + \hat{\varphi}_{-\mathbf{q}}), \\ \hat{Q}_- &= \sqrt{\frac{\hbar}{4M\omega_{\mathbf{q}}}} (i\hat{\varphi}_{\mathbf{q}} - i\hat{\varphi}_{-\mathbf{q}}), \end{aligned} \quad (9)$$

and their corresponding conjugate momenta:

$$\begin{aligned} \hat{P}_+ &= \sqrt{\hbar M \omega_{\mathbf{q}}} (\hat{\pi}_{\mathbf{q}} + \hat{\pi}_{-\mathbf{q}}), \\ \hat{P}_- &= \sqrt{\hbar M \omega_{\mathbf{q}}} (i\hat{\pi}_{\mathbf{q}} - i\hat{\pi}_{-\mathbf{q}}). \end{aligned} \quad (10)$$

Here, M is the ion mass. It is readily verified that $[\hat{Q}_+, \hat{P}_+] = [\hat{Q}_-, \hat{P}_-] = i\hbar$ while all other commutators vanish. The Hamiltonian can be easily written in terms of \hat{Q}_{\pm} and \hat{P}_{\pm}

¹Our definition of $\hat{\varphi}_{\mathbf{q}}$ and $\hat{\pi}_{\mathbf{q}}$ deviates from the standard literature, resulting in unbalanced prefactors of the kinetic and potential terms in the harmonic oscillator Hamiltonian.

operators:

$$H_{p,q} = \sum_{\alpha=\pm} \left(\frac{\hat{P}_\alpha^2}{2M} + \frac{1}{2} M \Omega_q^2(t) \hat{Q}_\alpha^2 \right), \quad (11a)$$

$$H_{ep,q} = \tilde{g}_q \sum_{\alpha=\pm} \hat{Q}_\alpha \hat{\rho}_\alpha, \quad (11b)$$

where $\tilde{g}_q = g_q \sqrt{2M\omega_q/\hbar}$, $\hat{\rho}_+ = (\hat{\rho}_q + \hat{\rho}_{-q})/\sqrt{2}$, $\hat{\rho}_- = i(\hat{\rho}_q - \hat{\rho}_{-q})/\sqrt{2}$, and

$$\Omega_q^2(t) = \omega_q^2 [1 + 2\alpha \cos(2\Omega_{\text{drv}} t)], \quad (12)$$

$$\alpha = -\kappa_3 \omega_q \varphi_1 / (\hbar \omega_q).$$

The Hamiltonian is the sum of two decoupled harmonic oscillators ($\alpha = \pm$) each with linear coupling to a standing electronic charge density wave. Since the $\alpha = \pm$ modes undergo a similar evolution, we will drop the \pm index hereafter and focus on one of the modes. In the absence of electron-phonon coupling, the problem reduces to a parametrically driven harmonic oscillator. Corrections arising from electron-phonon coupling can be studied order by order using time-dependent perturbation theory in the weak-coupling limit $g_q v(0) \ll 1$. This can be done, e.g., via a perturbative expansion of the unitary evolution operator $\hat{U}(t) = \mathcal{T} \exp[-i\hbar^{-1} \int_0^t dt' \hat{H}_{\pm q}(t')]$ in the powers of \tilde{g}_q [40]. The leading-order correction to the action is $\mathcal{O}(\tilde{g}_q^2)$ and is easily found as

$$\Delta S^{(2)}(t) = -\frac{|\tilde{g}_q|^2}{\hbar} \int_{-\infty}^t dt' e^{-\epsilon(t-t')} \mathcal{D}_{QQ}^R(t,t') \hat{\rho}(t) \hat{\rho}(t'), \quad (13)$$

where $\mathcal{D}_{QQ}^R(t,t') = -i\theta(t-t') \langle [\hat{Q}(t), \hat{Q}(t')] \rangle$ is the retarded phonon correlator and ϵ is an infinitesimal. It is well known that this correction implies an attractive interaction between the electrons in the long-wavelength regime $|\xi_{\mathbf{k}\pm q} - \xi_{\mathbf{k}}| \ll \omega_q$. In this regime of interest, the phase winding of the electron charge density excitation is much slower than the phonon time scale. Thus, to simplify the discussion further, we simply neglect the relative phase winding of the electron charge density waves and set $\hat{\rho}(t') \rightarrow \hat{\rho}(t)$ from the outset. Note that this coincides with the usual $\varepsilon_{\mathbf{k}} = \varepsilon_{\mathbf{k}'} = \varepsilon_F$ approximation in the BCS treatment. This results in the following simple expression for the phonon-mediated attractive interaction $\Delta S^{(2)}(t) = U(t) \hat{\rho}(t) \hat{\rho}(t)$, where

$$U(t) = \frac{|\tilde{g}_q|^2}{\hbar} \int_{-\infty}^t dt' e^{-\epsilon(t-t')} \mathcal{D}_{QQ}^R(t,t'). \quad (14)$$

Since the Hamiltonian is time dependent, $U(t)$ is expected to be time dependent as well. In particular, for the periodic Hamiltonian given in Eq. (11a), $U(t)$ further admits a Fourier expansion $U(t) = \sum_{n=-\infty}^{+\infty} U_n e^{-2in\Omega_{\text{drv}} t}$ in the harmonics of $2\Omega_{\text{drv}}$. In plain words, $U(t)$ is proportional to the *mean displacement* of the oscillator up to time t in response to a momentum boost at all prior times.

The retarded phonon propagator $\mathcal{D}_{QQ}^R(t,t')$ is most easily calculated using Heisenberg equations for $\hat{Q}(t)$ and $\hat{P}(t)$:

$$\frac{d\hat{Q}(t)}{dt} = \frac{\hat{P}(t)}{M}, \quad (15a)$$

$$\frac{d\hat{P}(t)}{dt} = -M\omega_q^2 [1 + 2\alpha \cos(2\Omega_{\text{drv}} t)] \hat{Q}(t). \quad (15b)$$

The Heisenberg equations exactly coincide with the classical equations of motion due to the Ehrenfest's theorem. The formal solution of these equations can be expressed in terms of Mathieu functions. For given Heisenberg operators at time t' , we find

$$\hat{Q}(t) = \mathfrak{M}_{QQ}(t,t') \hat{Q}(t') - \mathfrak{M}_{QP}(t,t') \frac{\hat{P}(t')}{M\Omega_{\text{drv}}},$$

$$\hat{P}(t) = \mathfrak{M}_{PQ}(t,t') M\Omega_{\text{drv}} \hat{Q}(t') + \mathfrak{M}_{PP}(t,t') \hat{P}(t'). \quad (16)$$

The explicit expressions for the \mathfrak{M} functions are given in Eq. (A1) in terms of even and odd Mathieu functions. In the limit $\alpha \rightarrow 0$ (no drive), we have $\lim_{\alpha \rightarrow 0} \mathfrak{M}_{QQ}(t,t') = \lim_{\alpha \rightarrow 0} \mathfrak{M}_{PP}(t,t') = \cos[\omega_q(t-t')]$, and $(\omega_q/\Omega_{\text{drv}}) \lim_{\alpha \rightarrow 0} \mathfrak{M}_{QP}(t,t') = -(\Omega_{\text{drv}}/\omega_q) \lim_{\alpha \rightarrow 0} \mathfrak{M}_{PQ}(t,t') = -\sin[\omega_q(t-t')]$, thus reducing Eq. (16) the usual nondriven harmonic oscillator evolution. Furthermore, $\mathfrak{M}_{QQ}(t',t') = \mathfrak{M}_{PP}(t',t') = 1$ and $\mathfrak{M}_{PQ}(t',t') = \mathfrak{M}_{QP}(t',t') = 0$, as it is also required from the initial condition. The retarded correlator is immediately calculated using Eq. (16), giving an exceedingly simple result:

$$\mathcal{D}_{QQ}^R(t,t') = -i\theta(t-t') \langle [\hat{Q}(t'), \hat{P}(t')] \rangle \times \frac{-\mathfrak{M}_{QP}(t,t')}{M\Omega_{\text{drv}}}$$

$$= -\frac{\hbar}{M\Omega_{\text{drv}}} \theta(t-t') \mathfrak{M}_{QP}(t,t'). \quad (17)$$

This result presents several important features:

(i) The retarded phonon propagator $\mathcal{D}_{QQ}^R(t,t')$ and consequently $U(t)$ [see Eq. (14)] are *fully determined* by $\mathfrak{M}_{QP}(t,t')$. The latter is in turn fully determined by the Heisenberg equations, and is independent of the initial wave function of phonons. In other words, for the Hamiltonian given in Eq. (11a), one obtains the same effective interaction $U(t)$ in all equilibrium and nonequilibrium phonon states. This is a direct consequence of the linearity of the harmonic oscillator evolution. As a corollary, this result immediately shows the peculiar cancellation of Bose enhancement factors between phonon absorption and emission processes in the conventional textbook diagrammatic calculation of U in equilibrium [41].

(ii) $\mathcal{D}_{QQ}^R(t,t') \propto \mathfrak{M}_{QP}(t,t')$ admits a simple classical interpretation: it coincides with the *displacement* of a classical driven oscillator at time t in response to a *momentum* jump at time t' , i.e., $\mathcal{D}_{QQ}^R(t,t') = \hbar \delta Q_{\text{cl}}(t) / \delta P_{\text{cl}}(t')$. This result can be obtained independently and more directly using quantum phase-space methods [42].

(iii) The origin of phonon-mediated attraction is purely quantum mechanical. Had \hat{Q} been a classical operator, it would commute with itself at different times and we would obtain $\lim_{\hbar \rightarrow 0} \mathcal{D}_{QQ}^R(t,t') = 0$. Nonetheless, this analysis provides a classical analogy as a response to a momentum jump (see the previous remark).

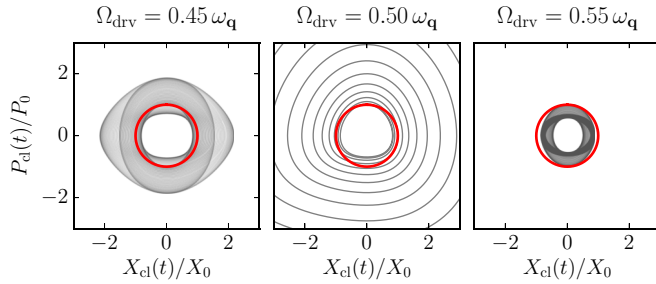


FIG. 3. Illustration of parametric amplification from classical phase-space trajectories. The classical phase-space trajectories correspond to a parametrically driven oscillator in response to a momentum jump with magnitude P_0 at $t = 0$ for Ω_{drv} below resonance (left), on resonance (middle), and above resonance (right). Here, $X_0 \equiv P_0/(2M\omega_q)$ is a normalization constant and the Mathieu parameter is set to $\alpha = 0.2$. The red circle is the periodic trajectory in the absence of the drive ($\alpha = 0$). Note the significantly amplified response below resonance $\Omega_{\text{drv}} < \omega_q/2$, the diverging response on resonance $\Omega_{\text{drv}} = \omega_q/2$, and suppressed response above resonance $\Omega_{\text{drv}} > \omega_q/2$.

The second remark implies that classical trajectories of a parametrically driven oscillator following a momentum jump encode the necessary and sufficient information to calculate $U(t)$. As a first example, let us consider the nondriven limit. In this case, we find $\lim_{\alpha \rightarrow 0} \mathfrak{M}_{QP}(t, t') = -(\Omega_{\text{drv}}/\omega_q) \sin \omega_q(t - t')$:

$$\lim_{\alpha \rightarrow 0} \mathcal{D}_{QP}^R(t, t') = \hbar \theta(t - t') \frac{\sin \omega_q(t - t')}{M\omega_q}. \quad (18)$$

The above result indeed corresponds the QP response of the classical harmonic oscillator up to a factor of \hbar . Plugging this result in Eq. (14), we find $U = -|g_q|^2/(\hbar\omega_q) = -2|g_q|^2/(\hbar\omega_q)$ which is the usual time-independent equilibrium result [43]. Note that regularizing prefactor $e^{-\epsilon(t-t')}$ is crucial for obtaining this result, without which the t' integration is ill defined. In a more realistic model with finite phonon damping, regularization is unnecessary.

Figure 3 shows the classical trajectories in response to a sudden momentum jump at $t = 0$ in the presence of a finite parametric drive. The red circular orbit shows the response in the absence of the drive. It is noticed that the classical trajectory diverges on resonance $\Omega_{\text{drv}} = \omega_q/2$ (middle panel), implying an *infinitely enhanced* response. Intuitively, the lattice becomes critically unstable in the presence of a resonant drive of finite amplitude such that smallest perturbation causes an infinitely large deformation. Just below the resonance (left panel), the trajectories are noticeably expanded in the phase space though they remain bounded. This corresponds to a moderately enhanced $U(t)$. Finally, the response is attenuated just above the resonance (right panel), which is the expected asymmetric behavior near a parametric resonance.

The time-dependent effective attraction $U(t)$ can be obtained numerically using Eqs. (17) and (14). The results are shown in Fig. 4. According to the previously mentioned periodicity $U(t + \pi/\Omega_{\text{drv}}) = U(t)$, we have only shown one full period in t . The immediately noticeable feature is the large temporal variations of $U(t)$ near parametric resonances, which is a manifestation of the wild variations of classical

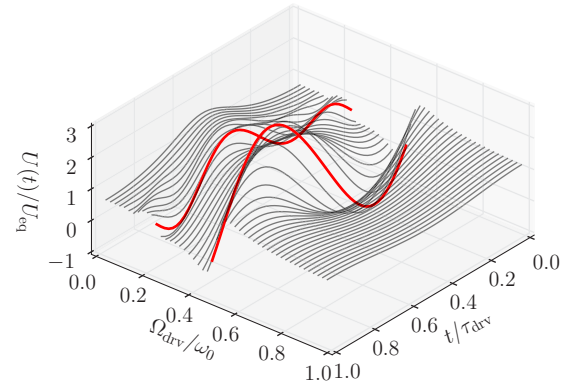


FIG. 4. The effective electron-electron interaction $U(t)$ as a function of drive frequency Ω_{drv} and time. Here, $\tau_{\text{drv}} = \pi/\Omega_{\text{drv}}$ and $U_{\text{eq}} = -2|g_q|^2/(\hbar\omega_q)$ is attraction strength in the absence of the drive. The Mathieu parameter is $\alpha = 0.2$ and we have set the damping rate to $\epsilon = 0.1\omega_q$. The red thick lines show $U(t)$ on the first two resonances $\Omega_{\text{drv}}/\omega_q = \frac{1}{2}, \frac{1}{4}$.

trajectories in the phase space in this regime. The perturbation series for $U(t)$ can be worked out using Eqs. (14), (17), and the expressions given in Appendix A. We quote the final result here:

$$\begin{aligned} \frac{U(t)}{U_{\text{eq}}} = & 1 - \frac{2\alpha \omega_q^2 \cos(2\Omega_{\text{drv}}t)}{\omega_q^2 - 4\Omega_{\text{drv}}^2} \\ & + \frac{2\alpha^2 \omega_q^2 [\omega_q^2 - 16\Omega_{\text{drv}}^2 + \omega_q^2 \cos(4\Omega_{\text{drv}}t)]}{(\omega_q^2 - 16\Omega_{\text{drv}}^2)(\omega_q^2 - 4\Omega_{\text{drv}}^2)} + \mathcal{O}(\alpha^4). \end{aligned} \quad (19)$$

Note the parametric resonances at $\Omega_{\text{drv}} = \omega_q/2$ in the first-order term and $\Omega_{\text{drv}} = \omega_q/4$ in the second-order term, as well as the appearance of higher-order harmonics of $2\Omega_{\text{drv}}$.

We remark that the parametric resonances of the Mathieu oscillator, $\Omega_{\text{drv}} = \omega_q/n$, $n \in \mathbb{N}$, do not necessarily imply a corresponding resonance in the effective attraction $U(t)$. As remarked after Eq. (14), $U(t)$ can be interpreted as the mean displacement of the oscillator in response to a momentum boost. The mean displacement can behave properly even for divergent trajectories. For example, the leading $n = 1$ parametric resonance at $\Omega_{\text{drv}} = \omega_q$ leaves $U(t)$ regular while leading to a divergent response at the same time. This can be easily noticed in the perturbation analysis: Eq. (A2) shows a resonance at $\Omega_{\text{drv}} = \omega_q$ while $U(t)$ remains regular [see Eq. (19) and Fig. 5].

The time average and variance of $U(t)/U_{\text{eq}}$ can be found readily using the above result:

$$\left\langle \frac{U(t)}{U_{\text{eq}}} \right\rangle = 1 + \frac{2\alpha^2 \omega_q^2}{\omega_q^2 - 4\Omega_{\text{drv}}^2} + \mathcal{O}(\alpha^4), \quad (20a)$$

$$\text{Var} \left[\frac{U(t)}{U_{\text{eq}}} \right] = \frac{2\alpha^2 \omega_q^4}{(\omega_q^2 - 4\Omega_{\text{drv}}^2)^2} + \mathcal{O}(\alpha^4). \quad (20b)$$

The leading-order correction to $\langle U(t) \rangle$ is $\mathcal{O}(\alpha^2)$. Figure 5 shows the average and variance of $U(t)$ within a period. The dashed lines show the above perturbative results. As

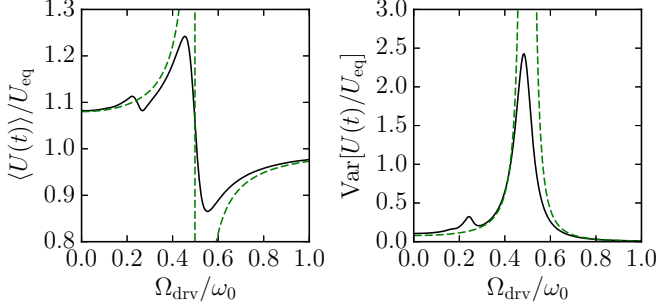


FIG. 5. Time average and variance of the effective electron-electron interaction. Solid lines are numerical results obtained from the solutions of the Mathieu equation. Dashed lines correspond to the perturbative results given in Eq. (20). The Mathieu parameter is set to $\alpha = 0.2$.

expected from the study of classical trajectories (see Fig. 3), $\langle U(t) \rangle$ is enhanced for frequencies below the resonance and is suppressed above the resonance. Perhaps more importantly, the temporal variance of $U(t)$ is significantly increased on either side of the resonance. This can be seen, e.g., from Eq. (20b). In the next section, we discuss the important role of enhanced temporal variations of $U(t)$ in enhancing the superconducting transition temperature.

A. Superconducting transition temperature for a time-dependent effective interaction

We showed that the parametric drive of the lattice results in the enhancement of the effective attraction mediated between the electrons $U(t)$. We further showed that $U(t)$ exhibits large oscillations in t near parametric resonances (see Fig. 4), such that $U(t)$ takes on values that are significantly higher and lower than its equilibrium value. According to the BCS theory, $T_c[U] \sim \exp\{-1/[\nu(0)U]\}$ where $\nu(0)$ is the electronic density of states (EDOS) at the Fermi surface. It is tempting to naively propose a replacement $U \rightarrow U(t)$ in the BCS formula and propose $T_c^{\text{drv}} \sim \langle T_c[U(t)] \rangle$. Since $T_c[U]$ is a convex function of U in the weak-coupling limit, one would then conclude $\langle T_c[U(t)] \rangle > T_c[\langle U(t) \rangle]$, i.e., temporal variations of $U(t)$ can increase T_c even if $\langle U(t) \rangle$ remains constant or even decreases. Of course, this argument lacks rigor and T_c^{drv} must be found within a proper Floquet extension of the BCS theory [28]. To this end, we assume

$$U(t) \approx U_0 + U_1 \cos(2\Omega_{\text{drv}}t), \quad (21)$$

where U_0 and U_1 can be read from Eq. (19):

$$U_0 = -\frac{g^2}{2\omega_0} \left[1 + \frac{2\alpha^2 \omega_{\mathbf{q}}^2}{\omega_{\mathbf{q}}^2 - 4\Omega_{\text{drv}}^2} + \mathcal{O}(\alpha^4) \right],$$

$$U_1 = \frac{g^2}{2\omega_0} \left[\frac{2\alpha \omega_{\mathbf{q}}^2}{\omega_{\mathbf{q}}^2 - 4\Omega_{\text{drv}}^2} + \mathcal{O}(\alpha^4) \right]. \quad (22)$$

The superconducting gap inherits the periodicity of $U(t)$ such that $\Delta(t) = \frac{1}{N} \sum_{\mathbf{k}} \langle \psi_{\mathbf{k},\uparrow}(t) \psi_{-\mathbf{k},\downarrow}(t) \rangle \rightarrow \sum_{n=-\infty}^{+\infty} \Delta_n e^{2ni\Omega_{\text{drv}}t}$. At the onset of pairing, the Floquet BCS

gap equation takes the following form [28]:

$$(1 - U_0 F_n) \Delta_n + \frac{U_1}{2} F_n (\Delta_{n-1} + \Delta_{n+1}) = 0, \quad (23)$$

where

$$F_n = -\nu(0) \int_{-\omega_c/2}^{\omega_c/2} d\xi \frac{\tanh[\xi/(2T)]}{2\xi - 2n\Omega_{\text{drv}} + i0^+}. \quad (24)$$

Here, T is the temperature and ω_c is the UV cutoff for U . For an Einstein phonon with frequency ω_0 , we expect $\omega_c \sim \omega_0$. In principle, T_c must be found such that Eq. (23) admits a nontrivial solution for $\{\Delta_n\}$ and since it is a homogeneous equation in $\{\Delta_n\}$, it reduces to the vanishing determinant condition for an (infinitely large) matrix.

A closed-form solution for T_c seems to be out of reach in general and one must resort to numerical methods. We attempt to find an approximate analytic solution with additional assumptions $U_0 \nu(0) \ll 1$ and $U_1 \ll U_0$. Strictly speaking, the last assumption does not generally apply to our problem since $|U_1| \geq |U_0|$ near the resonances. Our main goal here is to demonstrate how temporal variations in $U(t)$ increase T_c rather than presenting a rigorous analysis; the latter is the objective of the upcoming sections. Thus, the additional simplifying assumptions must be taken with this understanding in mind.

As a first step, we observe that $\Delta_{n+1}/\Delta_n \sim \mathcal{O}(U_1/U_0) \ll 1$. Therefore, we may neglect Δ_n for $|n| \geq 2$ for small U_1 . This reduces the infinite set of equations for $\{\Delta_n\}$ to only three equations for Δ_0 , Δ_1 , and Δ_{-1} . Omitting $\Delta_{\pm 1}$ between the equations and assuming $\Delta_0 \neq 0$, we find the following approximate pairing condition:

$$U_0 F_0 + \frac{U_1^2}{4} F_0 \left(\frac{F_1}{1 - U_0 F_1} + \frac{F_{-1}}{1 - U_0 F_{-1}} \right) = 1. \quad (25)$$

Approximate expressions for F_n can be found in the limit $T/\omega_c, T/\Omega_{\text{drv}} \ll 1$ using the Sommerfeld expansion technique. We quote the final result here:

$$F_0 = -\nu(0) [\ln(2\omega_c/T) + \gamma - \ln \pi + \mathcal{O}(T/\omega_c)],$$

$$F_n = -\frac{\nu(0)}{2} \left[-i\pi \text{sgn}(n) + \ln \left| \frac{\omega_c^2}{n^2 \Omega_{\text{drv}}^2} - 1 \right| + \mathcal{O}(e^{-\omega_c/T_c}) \right] \quad (|n| > 0), \quad (26)$$

where $\gamma \simeq 0.577$ is the Euler-Mascheroni constant. The final result resembles the BCS formula for T_c , though, with U_0 replaced with an effective interaction U_{eff} :

$$T_c^{\text{drv}} \simeq \frac{2e^\gamma}{\pi} \omega_c \exp\{-1/[\nu(0)U_{\text{eff}}]\}, \quad (27a)$$

where

$$U_{\text{eff}} \approx \begin{cases} |U_0| + \frac{\nu(0)U_1^2}{4} \ln \left| \frac{\omega_c^2}{\Omega_{\text{drv}}^2} - 1 \right|, & \frac{\omega_c}{\Omega_{\text{drv}}} \approx 1, \\ |U_0| + \frac{U_1^2}{2|U_0|}, & \frac{\omega_c}{\Omega_{\text{drv}}} \sim 1. \end{cases} \quad (27b)$$

We notice that $U_{\text{eff}} > |U_0|$ in both cases. The last result provides a well-founded justification for our preliminary heuristic argument based on the convexity of $T_c[U]$.

Finally, we have plotted T_c^{drv} based on the approximate analytic results obtained in this section [Eqs. (22), (27a),

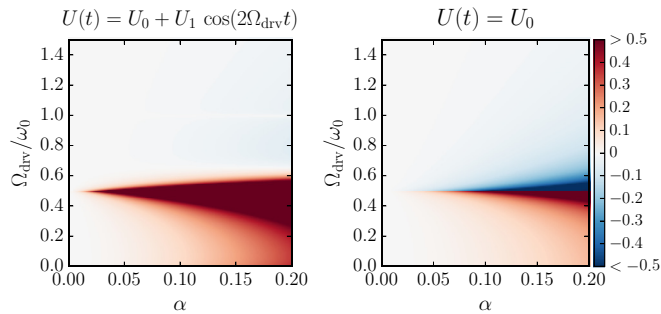


FIG. 6. Heat map plot of $T_c^{\text{drv}}/T_c^{\text{eq}} - 1$ based on the analytic Floquet-BCS analysis of Sec. III A. The plot on the left is the result obtained from $U(t) = U_0 + U_1 \cos(2\Omega_{\text{drv}}t)$. The plot on the right is obtained by neglecting the ac component and setting $U(t) = U_0 = \text{const}$. The significant role of oscillations of $U(t)$ in enhancing T_c is clearly noticeable. Note that U_0 and U_1 are both functions of α and Ω_{drv} as given in Eq. (22), and T_c is calculated using Eqs. (27a) and (27b). In both cases, we have set $v(0)U_{\text{eq}} = 0.5$ and $\omega_c = \omega_0$.

and (27b)] in Fig. 6. The left heat map plot shows the full result, when both dc and ac components of $U(t)$ are taken into account. It is noticed that T_c is dramatically enhanced both below and above the resonance. The right plot shows the result when only the dc component U_0 is kept. While T_c^{drv} is enhanced below the resonance, it is suppressed for $\Omega_{\text{drv}} > \omega_0/2$. This result can be understood by appealing to Fig. 5. The time-averaged interaction $\langle U(t) \rangle = U_0$ is lower than U_{eq} for $\Omega_{\text{drv}} > \omega_0/2$, and T_c is decreased accordingly. In contrast, including the ac component brings in large oscillations $\propto U_1$ which offset the loss in U_0 by allowing $U(t)$ to exceed U_{eq} during a fraction of each cycle.

We will obtain a plot similar to Fig. 6 later using a Floquet extension of the Migdal-Eliashberg theory (see Fig. 10), and we will find that the approximate analytic picture provided here remains remarkably accurate. We conclude this section by noting that had we included higher-order harmonic corrections in $U(t)$, we would get additional parametric resonances aside from the main one. Those would subsequently lead to additional “tongues” in Fig. 6 around $\Omega_{\text{drv}} = \omega_0/4, \omega_0/8, \dots$ (see Fig. 10).

B. Higher-order nonlinearities, phonon damping, and parametric resonance

Our discussion in the last two sections was based on a cubic lattice nonlinearity. We showed that the nonlinearity leads to a constant renormalization of $\omega_{\mathbf{q}}$ and produces a $\sim \cos(2\Omega_{\text{drv}}t)$ periodic correction to $\omega_{\mathbf{q}}$ at the leading order [see Eq. (6)]. The scenario remains similar for quartic nonlinearities, save for an additional $\sim \cos(4\Omega_{\text{drv}}t)$ correction to $\omega_{\mathbf{q}}$. This can be seen by expanding the square brackets in Eq. (7). In fact, for a nonlinearity $\sim \hat{\varphi}^n$ ($n \geq 3$), we find $\hat{\varphi}^n \approx \langle \hat{\varphi}_0(t) \rangle^{n-2} \sum_{\mathbf{q}} \hat{\varphi}_{\mathbf{q}} \hat{\varphi}_{-\mathbf{q}}$. Subsequently, $\langle \hat{\varphi}_0(t) \rangle^{n-2}$ can be expanded in harmonics of $2\Omega_{\text{drv}}$ such that $\omega_{\mathbf{q}}^2 \rightarrow \omega_{\mathbf{q}}^2 [1 + \sum_{n=0}^{n-2} \alpha_n \cos(2n\Omega_{\text{drv}}t)]$ for some $\{\alpha_n\}$. This analysis can be naturally extended for any smooth nonlinear potential. Since all parametric drive terms are harmonics of $2\Omega_{\text{drv}}$, the physics is expected to remain qualitatively similarly to the single

harmonic case. For example, the case of double parametric drive terms is studied in Ref. [44], where it is shown if the drive frequencies are integer multiples of one another, the same instability “tongue” patterns are obtained. Finally, let us mention in passing that with a finite phonon damping and for a fixed driving strength, the infinite cascade of ideal parametric resonances at $\Omega_{\text{drv}} = \omega_0/(2n)$ will be truncated above a certain order [45]. For instance, only two resonances are noticeable in Fig. 4 (black lines). The reason can be traced back to using a small phonon damping in the numerics.

C. Intermission

We derived a simple formula for the phonon-mediated electron-electron attraction $U(t)$ in the presence of parametric drive [Eq. (14)]. We showed that $U(t)$ is independent of the initial phonon wave function and is fully determined by the Hamiltonian and the drive. We related $U(t)$ to the momentum-jump response of a classical parametric oscillator and used this classical analogy to demonstrate the parametric amplification of $U(t)$ by appealing to the classical phase-space trajectories of the parametric oscillator. Finally, we calculated an analytical formula for T_c using a Floquet generalization of the BCS theory [28] and demonstrated that the oscillations $U(t)$, as well as its increased time average, lead to enhanced T_c .

Parametric amplification, while enhancing T_c at the first glance, leads to several undesirable consequences as well. It leads to parametric phonon generation, a well-known phenomenon in the context of early universe field theory [46]. The generated phonons heat up the electrons and decrease their coherence. The oscillatory effective electron-electron interaction $U(t)$ also generates electron-hole excitations on its own account [28]. An unbiased and consistent analysis of these competing effects is a challenging task and requires a rigorous and unified treatment. In the remainder of the paper, we will develop such a formalism and revisit the problem one more time in full detail.

IV. FLOQUET-MIGDAL-ELIASHBERG QUANTUM KINETIC THEORY

The major steps of the forthcoming calculation are summarized graphically in Fig. 7. Initially, the electron-phonon system is prepared in a normal-conducting equilibrium state with temperature $T_i > T_c$, where T_c is the equilibrium critical temperature for Cooper pairing. The external drive is then ramped up and initiates the nonequilibrium quantum dynamics.

We study the coupled quantum dynamics of the lattice displacement, phonons, and electrons by deriving and numerically solving a set of quantum kinetic equations specifically tailored for investigating driven electron-phonon systems. We start this theoretical development from a two-particle-irreducible effective active (2PI-EA) formulation of the Migdal-Eliashberg theory extended to nonlinear lattices in Sec. IV A, followed by a Floquet generalization of the ensuing quantum kinetic equations in Secs. IV C–IV E.

Once the evolution of the system in the normal-conducting state is calculated, it is checked for the emergence of a Floquet superconducting instability during the evolution. This step is enabled by deriving a Floquet-Migdal-Eliashberg gap equation

defined as

$$\Pi_{\mathbf{q}}(t_1, t_2) = \frac{1}{N} \sum_{\mathbf{k}} |g_{\mathbf{k}, \mathbf{k}+\mathbf{q}}|^2 \text{tr} [\hat{\mathcal{G}}_{\mathbf{k}+\mathbf{q}}(t_1, t_2) \hat{\sigma}_3 \hat{\mathcal{G}}_{\mathbf{k}}(t_2, t_1) \hat{\sigma}_3], \quad (28e)$$

and the local phonon propagator \mathcal{D}_ℓ appearing in the last three terms of (28a) is defined as

$$\mathcal{D}_\ell(t_1, t_2) = \frac{1}{N} \sum_{\mathbf{q}} \mathcal{D}_{\mathbf{q}}(t_1, t_2). \quad (28f)$$

We note that the external drive only appears in the classical action $S_{\text{cl}}[\varphi]$ and couples to $\varphi_{\mathbf{q}=0}$. The latter directly couples to finite- \mathbf{q} phonons via nonlinearities [see the fifth and sixth diagrams in Eq. (28b)], and to electrons if $g_{\mathbf{k}, \mathbf{k}} \neq 0$ [SSH-type phonons, see the fourth diagram in Eq. (28b)].

The equations of motion are found by imposing the stationarity condition on Γ with respect to φ , \mathcal{G} , and \mathcal{D} . For the classical displacement, we find

$$\begin{aligned} & \frac{1}{2\omega_0} (\partial_t^2 + \omega_0^2 + \gamma_0 \omega_0 \partial_t) \varphi(t) - \frac{\kappa_4}{6} \varphi^3(t) - \frac{\kappa_3}{2} \varphi^2(t) \\ & - \frac{\kappa_4}{2} \chi(t) \varphi(t) \\ & = \frac{\Lambda}{2} |F(t)|^2 + \frac{\kappa_3}{2} \chi(t) + \eta(t), \end{aligned} \quad (29)$$

where

$$\chi(t) \equiv \frac{1}{N} \sum_{\mathbf{q}} i \mathcal{D}_{\mathbf{q}}(t, t), \quad (30a)$$

$$\eta(t) \equiv \frac{i}{N} \sum_{\mathbf{k}} g_{\mathbf{k}, \mathbf{k}} \text{tr} [\hat{\mathcal{G}}_{\mathbf{k}}(t, t^+) \hat{\sigma}_3]. \quad (30b)$$

Here, $\chi(t)$ is the phonon tadpole and $\eta(t)$ is the electron-mediated classical force on the uniform lattice displacement. The evolution of \mathcal{D} is given by the following set of Kadanoff-Baym (KB) equations:

$$\begin{aligned} & -\frac{1}{2\omega_{\mathbf{q}}} [\partial_{t_1}^2 + \omega_{\mathbf{q}}^2] \mathcal{D}_{\mathbf{q}}(t_1, t_2) \\ & = \delta_{\mathcal{C}}(t_1, t_2) + V(t_1) \mathcal{D}_{\mathbf{q}}(t_1, t_2) + \int_{\mathcal{C}} d\tau \Pi_{\mathbf{q}}(t_1, \tau) \mathcal{D}_{\mathbf{q}}(\tau, t_2), \end{aligned} \quad (31a)$$

$$\begin{aligned} & -\frac{1}{2\omega_{\mathbf{q}}} [\partial_{t_2}^2 + \omega_{\mathbf{q}}^2] \mathcal{D}_{\mathbf{q}}(t_1, t_2) \\ & = \delta_{\mathcal{C}}(t_1, t_2) + V(t_2) \mathcal{D}_{\mathbf{q}}(t_1, t_2) + \int_{\mathcal{C}} d\tau \mathcal{D}_{\mathbf{q}}(t_1, \tau) \Pi_{\mathbf{q}}(\tau, t_2), \end{aligned} \quad (31b)$$

where

$$V(t) \equiv -\frac{\kappa_4}{2} \chi(t) - \frac{\kappa_4}{2} \varphi^2(t) - \kappa_3 \varphi(t) \quad (32)$$

is a local time-dependent potential acting on phonons. Aside from $\chi(t)$ which is a phonon self-interaction, the second and third terms are responsible for the parametric drive of phonons in connection to the analysis given in Sec. III.

Finally, the evolution of the CTP Nambu electron propagator \mathcal{G} is given by the following set of KB equations:

$$\begin{aligned} & [i \partial_{t_1} \mathbb{I} - \xi_{\mathbf{k}} \hat{\sigma}_3 - \varphi(t_1) g_{\mathbf{k}, \mathbf{k}} \hat{\sigma}_3] \hat{\mathcal{G}}_{\mathbf{k}}(t_1, t_2) \\ & = \delta_{\mathcal{C}}(t_1, t_2) + \int_{\mathcal{C}} \hat{\Sigma}_{\mathbf{k}}(t_1, \tau) \hat{\mathcal{G}}_{\mathbf{k}}(\tau, t_2), \end{aligned} \quad (33a)$$

$$\begin{aligned} & [i \partial_{t_2} \mathbb{I} - \xi_{\mathbf{k}} \hat{\sigma}_3 - \varphi(t_2) g_{\mathbf{k}, \mathbf{k}} \hat{\sigma}_3] \hat{\mathcal{G}}_{\mathbf{k}}(t_1, t_2) \\ & = \delta_{\mathcal{C}}(t_1, t_2) + \int_{\mathcal{C}} \hat{\mathcal{G}}_{\mathbf{k}}(t_1, \tau) \hat{\Sigma}_{\mathbf{k}}(\tau, t_2), \end{aligned} \quad (33b)$$

where the Nambu self-energy is given as

$$\hat{\Sigma}_{\mathbf{k}}(t_1, t_2) = \frac{1}{N} \sum_{\mathbf{k}'} |g_{\mathbf{k}, \mathbf{k}'}|^2 \hat{\sigma}_3 \hat{\mathcal{G}}_{\mathbf{k}'}(t_1, t_2) \hat{\sigma}_3 i \mathcal{D}_{\mathbf{k}-\mathbf{k}'}(t_1, t_2), \quad (34)$$

which is the usual Migdal-Eliashberg self-energy in real time. Explicit equations for the retarded (R), advanced (A), and Keldysh (K) components of $\hat{\mathcal{G}}$ and \mathcal{D} can be worked out from Eqs. (33a) and (33b) and Eqs. (31a) and (31b) using Langreth rules [48], respectively.

In principle, the solution of the coupled integrodifferential equations derived in this section, while being a daunting task, yields a complete and unbiased analysis. Given that our goal in this paper is to give a transparent account of the key mechanisms that play a role in enhancing or suppressing superconductivity, we find it rather beneficial to simplify the model to the greatest possible extent without sacrificing any qualitative physics.

B. Trimmed-down model

In this section, we present and discuss several simplifying approximations which we adopt in the rest of the paper. These assumptions are presented in a single section, rather than incrementally, for better clarity.

Holstein-type electron-phonon coupling. Depending on the nature of the electron-phonon coupling, $g_{\mathbf{k}, \mathbf{k}'}$ may assume different dependencies on \mathbf{k} and \mathbf{k}' . For Holstein-type phonons, appropriate for describing longitudinal optical (LO) phonons, $g_{\mathbf{k}, \mathbf{k}'}$ only depends on the net momentum of the electron-hole excitation, i.e., $g_{\mathbf{k}, \mathbf{k}'} \sim g_{\mathbf{k}-\mathbf{k}'}$. On the other hand, for Su-Shrieffer-Hieger-type (SSH-type) phonons, $g_{\mathbf{k}, \mathbf{k}'}$ will depend on the individual momenta. We restrict our analysis to Holstein-type coupling here.

For a realistic description of an electron-phonon system, some aspects of the Coulomb interaction must be incorporated into the model, in particular, the renormalized electron dispersion $\xi_{\mathbf{k}}$ and screening of the electron-phonon coupling $g_{\mathbf{k}-\mathbf{k}'}^{(\text{scr})} \approx g_{\mathbf{k}-\mathbf{k}'}/\varepsilon(\Omega, \mathbf{k}-\mathbf{k}')$ [43]. Here, ε is the dielectric function and Ω is the relevant energy scale of the dynamical screening process which is commonly set to zero. In our problem, the largest relevant frequency for dynamical screening is set by external drive and the optical phonon peak frequency, whichever is the largest. In the regime relevant to the experiments, both are an order of magnitude smaller than the typical plasma frequency ω_p . For example, $\omega_p \approx 0.5 - 2$ eV for fulleride superconductors whereas the typical frequency of optical phonons is $\omega_{\text{ph}} \approx 10 - 100$ meV [13]. Therefore, we may

safely use the static Thomas-Fermi (TF) dielectric function:

$$g_{\mathbf{k}-\mathbf{k}'}^{(\text{scr})} \simeq \frac{g_{\mathbf{k}-\mathbf{k}'}}{\varepsilon^{\text{TF}}(\mathbf{k}-\mathbf{k}')} = \frac{g_{\mathbf{k}-\mathbf{k}'}}{1 + q_{\text{TF}}^2/|\mathbf{k}-\mathbf{k}'|^2}. \quad (35)$$

The screened coupling in the long wavelength $|\mathbf{k}-\mathbf{k}'| \ll q_{\text{TF}}$ is almost perfectly screened. As a consequence, (1) the direct coupling of the uniform $\mathbf{q}=0$ lattice displacement to conduction electrons [described by the fourth diagram in Eqs. (28b) and (30b)] is vanishingly small and can be neglected; (2) the time-dependent correction $g_{\mathbf{k},\mathbf{k}'}\varphi(t)$ to the electron dispersion in Eqs. (33a) and (33b) vanishes as well.

Nondispersive (Einstein) optical phonons. So far, we have assumed a general dispersion $\omega_{\mathbf{q}}$ for the optical phonon. We neglect the phonon dispersion hereafter, i.e., $\omega_{\mathbf{q}} \rightarrow \omega_0$, which is an excellent approximation for a large class of materials, including fulleride superconductors [14].

Local approximation for $\Pi_{\mathbf{q}}$. In the absence of $\Pi_{\mathbf{q}}$ phonon self-energy correction appearing on the right-hand side of Eqs. (31a) and (31b) and using Einstein phonons, the phonon propagator $\mathcal{D}_{\mathbf{q}}$ will have no \mathbf{q} dependence. Therefore, the \mathbf{q} dependence of $\mathcal{D}_{\mathbf{q}}$ is entirely induced by $\Pi_{\mathbf{q}}$. The \mathbf{q} dependence of the latter is inherited from $g_{\mathbf{k},\mathbf{k}'}$ and the electron dispersion $\xi_{\mathbf{k}}$ [see Eq. (28e)] and is nonuniversal. In an attempt to simplify the model, we propose a local approximation for $\Pi_{\mathbf{q}}$ in the spirit of dynamical mean field theory (DMFT) [23,49,50]:

$$\Pi_{\mathbf{q}}(t_1, t_2) \rightarrow \Pi_{\ell}(t_1, t_2) \equiv \frac{1}{N} \sum_{\mathbf{q}} \Pi_{\mathbf{q}}(t_1, t_2). \quad (36)$$

The local approximation for $\Pi_{\mathbf{q}}$ has an important practical advantage. It removes the \mathbf{q} dependence from $\mathcal{D}_{\mathbf{q}}$ and allows us to study a single momentum mode.

Fermi-surface averaged (FSA) electron self-energy. The Cooper pairing process in the majority of conventional superconductors only involves electrons within a thin shell about the Fermi surface. This observation is the basis of a widely used approximation where the Migdal-Eliashberg electron self-energy $\hat{\Sigma}_{\mathbf{k}}$ is replaced with its Fermi-surface averaged (FSA) approximation:

$$\hat{\Sigma}_{\mathbf{k}}(t_1, t_2) \rightarrow \hat{\Sigma}(t_1, t_2) \equiv \langle\langle \hat{\Sigma}_{\mathbf{k}}(t_1, t_2) \rangle\rangle_{\text{FS}}. \quad (37)$$

This approximation, being akin to DMFT-type approximation, fully retains the dynamical structure of the self-energy while simplifying the momentum summations by removing the spatial structure of the self-energy. We remark that the FSA approximation is indeed an excellent approximation while adopting the previous two approximations: for a local Holstein-type electron-phonon coupling and Einstein phonons, $\hat{\Sigma}_{\mathbf{k}}$ naturally loses its \mathbf{k} dependence [see Eq. (34)].

Flat electronic density of states (EDOS). We neglect the variations of the EDOS $\nu(\xi)$ and pin it to its value at the Fermi surface $\nu(0)$. This is an excellent approximation in three-dimensional systems.

Ideal Migdal's limit. We work in the ideal Migdal's limit $\omega_{\text{ph}}/W_{\text{el}} \rightarrow 0$.

C. Floquet-Boltzmann quantum kinetic formalism

Despite the simplifications proposed to the model in Sec. IV B, the solution of the KB equations and obtaining

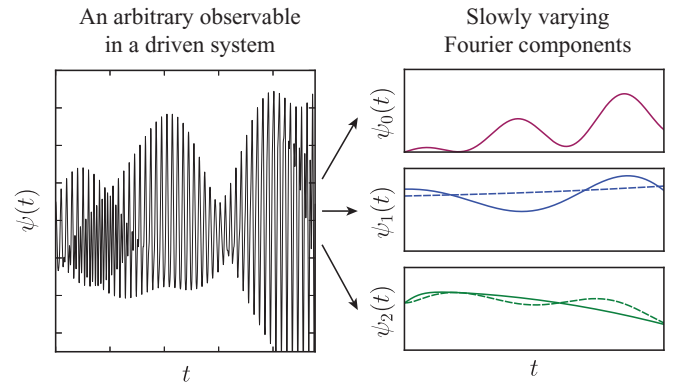


FIG. 8. An illustration of Floquet-Boltzmann kinetic formalism. An arbitrary observable in a driven system is expected to have fast temporal variations on the scale of the driving frequency and a slowly varying envelope. By decomposing the observable into the harmonics of the driving frequency using short-time Fourier transforms.

the two-time propagators remains a challenging numerical task. Provided that the external perturbing field varies on time and length scales longer than the intrinsic microscopic time and scale of the many-body system, the KB equations can be controllably reduced to one-time kinetic-type equation using the machinery of Wigner transforms and gradient expansion [25,48]. The case of driven systems is subtler though since the external drive $F(t)$ has both *fast* and *slow* components: even though the temporal variations of the amplitude $F_{\text{env}}(t)$ occurs on long-time scales (compared to the phonon period), the multiplicative oscillatory factor $\cos(\Omega_{\text{drv}}t)$ varies on the same scale as the phonon frequency in the interesting nearly resonant regime. In this section, we show that by introducing Floquet bands via short-time Fourier transforms, we can perform gradient expansion on the amplitude of Fourier components and derive Boltzmann-type quantum kinetic equations. This procedure is schematically shown in Fig. 8.

Floquet-Wigner (FW) transform. Let $\mathcal{A}(t_1, t_2)$ be an arbitrary two-time function, such as the $\hat{G}(t_1, t_2)$ and $\mathcal{D}(t_1, t_2)$. The Wigner transform $\mathcal{A}(\omega, t)$ is formally defined as

$$\mathcal{A}(\omega, t) = \int_{-\infty}^{+\infty} d\tau e^{i\omega\tau} \mathcal{A}(t + \tau/2, t - \tau/2). \quad (38)$$

Here, $t = (t_1 + t_2)/2$ is the *center-of-mass (COM) time* and $\tau = t_1 - t_2$ is the relative time on which we perform a Fourier transform. The COM time dependence vanishes at equilibrium. By continuity, we expect the presence of a slowly varying external field to induce a similarly slowly varying COM dependence on $\mathcal{A}(\omega, t)$. This permits a controllable series expansion in successive COM time derivatives of $\mathcal{A}(\omega, t)$ in the collision integrals [48]. In case of periodically driven systems, however, the fast oscillatory component of the external field can induce fast harmonics on the COM dependence of all two-time quantities. To make a connection with Fig. 8, one must identify $\psi(t)$ as $\mathcal{A}(\omega, t)$ for a fixed value of ω . In principle, we can resolve the t dependence of $\mathcal{A}(\omega, t)$ into Fourier harmonics of the drive using short-time Fourier transforms:

$$\mathcal{A}(\omega, t) = \sum_n \mathcal{A}_n(\omega; t) e^{-in\Omega t}, \quad (39)$$

where formally $\mathcal{A}_n(\omega; t) = \int_{-\infty}^{+\infty} dt' W(t' - t) e^{in\Omega t'} \mathcal{A}(\omega, t')$. We express the COM time of the harmonics as a label, i.e., $\mathcal{A}_n(\omega; t)$, to emphasize on the quasistatic nature of the Fourier amplitudes. Here, Ω is the principal frequency of the driving term. In the present context, $\Omega = 2\Omega_{\text{drv}}$ since the external drive appears as $|F(t)|^2$ in the model. $W(t)$ is a *window function* normalized to unity and concentrated near $t = 0$ with support in the time interval $\sim(-\tau_W, +\tau_W)$ where $\Omega^{-1} \ll \tau_W \ll |F_{\text{env}}(t)|/|F'_{\text{env}}(t)|$. The shape of the window function is immaterial so long as this condition is satisfied [51]. We refer to the collection of $\{\mathcal{A}_n(\omega, t)\}$ as the *Floquet-Wigner transform* of $\mathcal{A}(t_1, t_2)$ and, hereafter, we assume that the Floquet components admit a controlled series expansion in COM time derivatives.

Floquet-Groenewold-Moyal (FGM) product formula. The convolution integrals appearing on the right-hand side of KB equations can be formally expressed as a series expansion using Groenewold-Moyal (GM) product formula [52,53]:

$$(\mathcal{A} \star \mathcal{B})(\omega, t) = \exp \left[\frac{i}{2} (\partial_t^B \partial_\omega^A - \partial_t^A \partial_\omega^B) \right] \mathcal{A}(\omega, t) \mathcal{B}(\omega, t). \quad (40)$$

The left-hand side represents the convolution integral of \mathcal{A} and \mathcal{B} followed by a Wigner transform. Expanding the exponentiated differential operator and truncating the series at finite orders yields an approximate expression for the convolution of \mathcal{A} and \mathcal{B} in terms of the time and frequency derivatives of their Wigner transforms. In particular, truncating the series at the first order yields the well-known *gradient expansion* formula which forms the basis of quantum kinetic equations [25]. This procedure can be readily generalized to the case of Floquet-Wigner transforms. To this end, we plug the Floquet-Wigner expansion of \mathcal{A} and \mathcal{B} [as given in Eq. (39)] in Eq. (40) and take a short-time Fourier transform of both sides. The final result is

$$\begin{aligned} (\mathcal{A} \star \mathcal{B})_n(\omega; t) &= \int_{-\infty}^{+\infty} dt' W(t' - t) e^{in\Omega t'} \\ &\times \exp \left[\frac{\Omega}{2} (n_B \partial_\omega^A - n_A \partial_\omega^B) + \frac{i}{2} (\partial_t^B \partial_\omega^A - \partial_t^A \partial_\omega^B) \right] \\ &\times \sum_{n_A, n_B} \mathcal{A}_{n_A}(\omega; t') \mathcal{B}_{n_B}(\omega; t') e^{-i(n_A + n_B)\Omega t'}. \end{aligned} \quad (41)$$

The COM time derivatives have been resolved into a part acting on the phasor and a part acting on the Fourier amplitudes, i.e., $\partial_t \rightarrow -in_{A/B}\Omega + \partial_t^{A/B}$. Performing the t' integral is trivial since by construction, we can neglect the

COM time variations $\{\mathcal{A}_n(\omega; t)\}$ and $\{\mathcal{B}_n(\omega; t)\}$ within the support of the window function. Using the formal Taylor's expansion formula $e^{\alpha \partial/\partial x} f(x) = f(x + \alpha)$, we finally obtain

$$\begin{aligned} (\mathcal{A} \star \mathcal{B})_n(\omega, t) &= \sum_{n_A, n_B} \delta(n - n_A - n_B) \exp \left[\frac{i}{2} (\partial_t^B \partial_\omega^A - \partial_t^A \partial_\omega^B) \right] \\ &\times \mathcal{A}_{n_A, -n_B}(\omega; t) \mathcal{B}_{n_B, n_A}(\omega; t), \end{aligned} \quad (42)$$

where we have defined

$$\mathcal{A}_{n,m}(\omega; t) \equiv \mathcal{A}_n(\omega - m\Omega/2; t). \quad (43)$$

We refer to labels n and m in $\mathcal{A}_{n,m}(\omega; t)$ as *Floquet band index* and *Floquet quasimomentum*, respectively, in analogy to the Bloch band theory. Equation (42) will be referred to as *Floquet-Groenewold-Moyal (FGM) product formula*. Expanding the exponentiated differential operator to linear order, we obtain the *FGM gradient expansion formula*.

D. Floquet-Boltzmann quantum kinetic equations for phonons

The formalism outlined in the previous section can be used to obtain quantum kineticlike (“one-time”) equations for the nonequilibrium evolution of the lattice displacement and phonon propagators in the presence of a periodic drive with a slowly varying envelope.

Starting with Eq. (29), taking a short-time Fourier transform of the sides and neglecting the second-order derivatives, we find

$$\begin{aligned} &[(\gamma_0 \omega_0 - 2in\Omega) \partial_t + \omega_0^2 - n^2 \Omega^2] \varphi_n - \frac{\omega_0 \kappa}{3} \sum_{n_1, n_2} \varphi_{n_1} \varphi_{n_2} \varphi_{n-n_1-n_2} \\ &- \omega_0 \kappa_3 \sum_{n_1} \varphi_{n_1} \varphi_{n-n_1} - \omega_0 \kappa_4 \sum_{n_1} \varphi_{n_1} \chi_{n-n_1} - \omega_0 \kappa_3 \chi_n \\ &= \omega_0^2 \Phi_n + \mathcal{O}(\partial_t^2). \end{aligned} \quad (44a)$$

We have dropped the t arguments for brevity, $\mathcal{O}(\partial_t^2)$ is a mnemonic for neglecting the second-order time derivative, and Φ_n is the Fourier amplitude for the external drive. For the drive given in Eq. (3), we have

$$\Phi_n(t) = \frac{\Lambda}{2\omega_0} F_{\text{env}}^2(t) \left[\delta_{n,0} + \frac{1}{2} \delta_{n,-1} + \frac{1}{2} \delta_{n,1} \right], \quad (44b)$$

and $\Omega \equiv 2\Omega_{\text{drv}}$. χ_n is found using Eq. (30a):

$$\chi_n(t) = \frac{1}{2} \int_{-\infty}^{+\infty} \frac{d\omega}{2\pi} i \mathcal{D}_n^K(\omega; t). \quad (44c)$$

Next, we consider the retarded component of the KB equation for \mathcal{D} . Taking a FW transform of the sides of Eqs. (31a) and (31b) and using the FGM gradient expansion formula in the collision convolution integrals, we find

$$\begin{aligned} &\left[\mathfrak{D}^{-1}(\omega + n\Omega/2) + \frac{i}{2} \partial_\omega \mathfrak{D}^{-1}(\omega + n\Omega/2) \partial_t \right] \mathcal{D}_n^R(\omega; t) \\ &= \delta_{n,0} + \sum_{n_1} \left[1 - \frac{i}{2} \partial_\omega^D \partial_t^V \right] V_{n_1}(t) \mathcal{D}_{n-n_1, n_1}^R(\omega; t) + \sum_{n_1} \left[1 + \frac{i}{2} \partial_\omega^\Pi \partial_t^D - \frac{i}{2} \partial_\omega^D \partial_t^\Pi \right] \Pi_{\ell, n_1, n_1-n}^R(\omega; t) \mathcal{D}_{n-n_1, n_1}^R(\omega; t) + \mathcal{O}(\partial_t^2), \end{aligned} \quad (45a)$$

$$\begin{aligned}
& \left[\mathfrak{D}^{-1}(\omega - n\Omega/2) - \frac{i}{2} \partial_\omega \mathfrak{D}^{-1}(\omega - n\Omega/2) \partial_t \right] \mathcal{D}_n^R(\omega; t) \\
&= \delta_{n,0} + \sum_{n_1} \left[1 + \frac{i}{2} \partial_\omega^D \partial_t^V \right] \mathcal{D}_{n-n_1, -n_1}^R(\omega; t) V_{n_1}(t) + \sum_{n_1} \left[1 + \frac{i}{2} \partial_\omega^D \partial_t^\Pi - \frac{i}{2} \partial_\omega^\Pi \partial_t^D \right] \mathcal{D}_{n_1, n_1-n}^R(\omega; t) \Pi_{\ell; n-n_1, n_1}^R(\omega; t) + \mathcal{O}(\partial_t^2),
\end{aligned} \tag{45b}$$

where $\mathfrak{D}^{-1}(\omega) \equiv (\omega^2 - \omega_0^2)/(2\omega_0)$ is the bare inverse phonon propagator in the frequency time. $V(t)$ was defined earlier in Eq. (E8) and is the self-consistently determined potential that parametrically drives the phonons. The Fourier amplitudes of $V(t)$ are trivially found as $V_{n_1}(t) = -(\kappa_4/2) \sum_{n_1} \varphi_{n_1}(t) \varphi_{n-n_1}(t) - (\kappa_4/2) \chi_n(t) - \kappa_3 \varphi_n(t)$. We have employed local approximation for Π . The phonon propagator thus can be thought of either as that of a single momentum mode or as the momentum-summed (local) one. We do not need a separate evolution equation for the advanced propagator since it can be determined from the retarded propagator via the identity $\mathcal{D}_n^A(\omega; t) = [\mathcal{D}_{-n}^R(\omega; t)]^*$.

The kinetic equations for the Keldysh phonon propagator are found in a similar fashion. First, we use the Langreth rules to find an explicit KB equation for \mathcal{D}^K , followed by a FW transform and FGM gradient expansion of the collision integral convolutions. The final result is

$$\begin{aligned}
& \left[\mathfrak{D}^{-1}(\omega + n\Omega/2) + \frac{i}{2} \partial_\omega \mathfrak{D}^{-1}(\omega + n\Omega/2) \partial_t \right] i\mathcal{D}_n^K(\omega; t) = \sum_{n_1} \left[1 - \frac{i}{2} \partial_\omega^D \partial_t^V \right] V_{n_1}(t) i\mathcal{D}_{n-n_1, n_1}^K(\omega; t) \\
&+ \sum_{n_1} \left[1 + \frac{i}{2} \partial_\omega^\Pi \partial_t^D - \frac{i}{2} \partial_\omega^D \partial_t^\Pi \right] \left[\Pi_{n_1, n_1-n}^{(\ell), R}(\omega; t) i\mathcal{D}_{n-n_1, n_1}^K(\omega; t) + i\Pi_{\ell; n_1, n_1-n}^K(\omega; t) \mathcal{D}_{n-n_1, n_1}^A(\omega; t) \right] + \mathcal{O}(\partial_t^2),
\end{aligned} \tag{46a}$$

$$\begin{aligned}
& \left[\mathfrak{D}^{-1}(\omega - n\Omega/2) - \frac{i}{2} \partial_\omega \mathfrak{D}^{-1}(\omega - n\Omega/2) \partial_t \right] i\mathcal{D}_n^K(\omega; t) = \sum_{n_1} \left[1 + \frac{i}{2} \partial_\omega^D \partial_t^V \right] i\mathcal{D}_{n-n_1, -n_1}^K(\omega; t) V_{n_1}(t) \\
&+ \sum_{n_1} \left[1 + \frac{i}{2} \partial_\omega^D \partial_t^\Pi - \frac{i}{2} \partial_\omega^\Pi \partial_t^D \right] \left[\mathcal{D}_{n_1, n_1-n}^R(\omega; t) i\Pi_{\ell; n-n_1, n_1}^K(\omega; t) + i\mathcal{D}_{n_1, n_1-n}^K(\omega; t) \Pi_{\ell; n-n_1, n_1}^A(\omega; t) \right] + \mathcal{O}(\partial_t^2).
\end{aligned} \tag{46b}$$

Even though Eqs. (45a)–(46b) have a more complex presentation compared to the original KB equations, they are significantly simpler to work with in practice: convolution integrals have been reduced to discrete Floquet index summations, and the two-time structure has been reduced to the COM time and the relative frequency ω which does not appear in a convolution. Finally, we remark that the electron-hole bubble Π_ℓ acts as a dissipation source (“bath”) for phonons, and must be determined by solving the evolution equations for $\hat{\mathcal{G}}$ in a fully self-consistent treatment. We will argue later that it can be approximately calculated using bare electron propagators at the initial temperature as long as heating does not bring up the energy density of electrons to phonon energy scales. Approximate expressions for Π_ℓ have been provided in Appendix E 1 [see Eq. (E17)]. We show Π_ℓ acts as a quantum Ohmic bath for phonons, and gives rise to a Lamb shift of the Einstein oscillator.

E. Floquet-Boltzmann quantum kinetic equations for electrons

We can obtain quantum kinetic equations for the nonequilibrium evolution of electrons similar to phonons. Before embarking on deriving these equations, we take a short detour to derive explicit expressions for the Migdal-Eliashberg and employ the approximations discussed in Sec. IV B.

1. Migdal-Eliashberg self-energy: General case

Our goal in this section is derive explicit expressions for various real-time components of the Migdal-Eliashberg self-energy, starting from Eq. (34). To keep the notation uncluttered, we will work out the results for a general Wigner-transformed propagators as a first step. We employ the approximations discussed in Sec. IV B step by step. The simplified self-energy expressions for Floquet-Wigner-transformed propagators are readily found in the end as a special case.

As a starting point, we transform Eq. (34) to the Wigner representation and employ the decomposition of propagators defined in Eqs. (B4a) and (B4b) in terms of their Keldysh and spectral components. The calculation is elementary and the final result is

$$\begin{aligned}
\hat{\Sigma}_{\mathbf{k}}^R(\omega, t) &= \frac{1}{2N} \sum_{\mathbf{k}'} |g_{\mathbf{k}, \mathbf{k}'}|^2 \int \frac{d\omega'}{2\pi} \frac{dv}{2\pi} \frac{1}{\omega - \omega' - v + i0^+} \{ i\mathcal{D}_{\mathbf{k}-\mathbf{k}'}^K(v, t) \check{\mathcal{A}}_{\mathbf{k}'}(\omega', t) + \rho_{\mathbf{k}-\mathbf{k}'}(v, t) i\check{\mathcal{G}}_{\mathbf{k}'}^K(\omega', t) \}, \\
i\hat{\Sigma}_{\mathbf{k}}^K(\omega, t) &= \frac{1}{2N} \sum_{\mathbf{k}'} |g_{\mathbf{k}, \mathbf{k}'}|^2 \int \frac{d\omega'}{2\pi} \frac{dv}{2\pi} (2\pi)\delta(\omega - \omega' - v) \{ i\mathcal{D}_{\mathbf{k}-\mathbf{k}'}^K(v, t) i\check{\mathcal{G}}_{\mathbf{k}'}^K(\omega', t) + \rho_{\mathbf{k}-\mathbf{k}'}(v, t) \check{\mathcal{A}}_{\mathbf{k}'}(\omega', t) \},
\end{aligned} \tag{47}$$

where the capped Nambu propagators are defined according to Eq. (B6). We define the Eliashberg function² $F_{\xi,\xi'}^\rho(v)$, as well as a Keldysh-Eliashberg function $iF_{\xi,\xi'}^K(v)$ as

$$F_{\xi,\xi'}^\rho(v,t) \equiv \frac{\nu(0)}{\nu(\xi)\nu(\xi')} \frac{1}{N^2} \sum_{\mathbf{k},\mathbf{k}'} \frac{|g_{\mathbf{k},\mathbf{k}'}|^2}{2\pi} \rho_{\mathbf{k}-\mathbf{k}'}(v,t) \delta(\xi_{\mathbf{k}} - \xi) \delta(\xi_{\mathbf{k}'} - \xi'), \quad (48a)$$

$$iF_{\xi,\xi'}^K(v,t) \equiv \frac{\nu(0)}{\nu(\xi)\nu(\xi')} \frac{1}{N^2} \sum_{\mathbf{k},\mathbf{k}'} \frac{|g_{\mathbf{k},\mathbf{k}'}|^2}{2\pi} i\mathcal{D}_{\mathbf{k}-\mathbf{k}'}^K(v,t) \delta(\xi_{\mathbf{k}} - \xi) \delta(\xi_{\mathbf{k}'} - \xi'). \quad (48b)$$

In the special case of Einstein phonons where $i\mathcal{D}_{\mathbf{q}}^K$ and $\rho_{\mathbf{q}}$ have no \mathbf{q} dependence, we find

$$F_{\xi,\xi'}^\rho(v,t) \equiv \frac{\alpha^2(\xi,\xi')}{2\pi} \rho(v,t), \quad (49a)$$

$$iF_{\xi,\xi'}^K(v,t) \equiv \frac{\alpha^2(\xi,\xi')}{2\pi} i\mathcal{D}^K(v,t), \quad (49b)$$

where the energy-resolved dimensionless coupling constant $\alpha^2(\xi,\xi')$ is defined as

$$\alpha^2(\xi,\xi') \equiv \frac{\nu(0)}{\nu(\xi)\nu(\xi')} \frac{1}{N^2} \sum_{\mathbf{k},\mathbf{k}'} |g_{\mathbf{k},\mathbf{k}'}|^2 \delta(\xi_{\mathbf{k}} - \xi) \delta(\xi_{\mathbf{k}'} - \xi'), \quad (50)$$

which in turn in the limit of flat EDOS and constant $g_{\mathbf{k},\mathbf{k}'}$ evaluates to $\alpha^2(\xi,\xi') \rightarrow \nu(0)g^2 \sim \text{const}$. The Fermi-surface averaged (FSA) self-energy is readily found as

$$\begin{aligned} \hat{\Sigma}^R(\omega,t) &\equiv \langle\langle \hat{\Sigma}_{\mathbf{k}}^R(\omega,t) \rangle\rangle_{\text{FS}} \\ &= \int_{-W/2}^{+W/2} d\xi' \frac{\nu(\xi')}{\nu(0)} \int_{-\infty}^{+\infty} \frac{d\omega'}{2\pi} \int_{-\infty}^{+\infty} \frac{d\nu}{\omega - \omega' - \nu + i0^+} \frac{1}{2} \{iF_{0,\xi'}^K(v,t) \check{\mathcal{A}}_{\xi'}(\omega',t) + F_{0,\xi'}^\rho(v,t) i\check{\mathcal{G}}_{\xi'}^K(\omega',t)\}, \end{aligned} \quad (51a)$$

$$\begin{aligned} i\hat{\Sigma}^K(\omega,t) &\equiv \langle\langle i\hat{\Sigma}_{\mathbf{k}}^K(\omega,t) \rangle\rangle_{\text{FS}} \\ &= \int_{-W/2}^{+W/2} d\xi' \frac{\nu(\xi')}{\nu(0)} \int_{-\infty}^{+\infty} \frac{d\omega'}{2\pi} \int_{-\infty}^{+\infty} d\nu (2\pi) \delta(\omega - \omega' - \nu) \frac{1}{2} \{iF_{0,\xi'}^K(v,t) i\check{\mathcal{G}}_{\xi'}^K(\omega',t) + F_{0,\xi'}^\rho(v,t) \check{\mathcal{A}}_{\xi'}(\omega',t)\}. \end{aligned} \quad (51b)$$

Since the FSA self-energy has no momentum dependence, the \mathbf{k} dependence of the resulting electron propagators is induced from the bare electron dispersion $\xi_{\mathbf{k}}$. Hence, we have legitimately replaced the \mathbf{k}' momentum labels with ξ' , and \mathbf{k}' momentum summations with EDOS-weighted ξ' integrals over the bandwidth $[-W_{\text{el}}/2, +W_{\text{el}}/2]$. At this point, we employ the remaining approximations discussed in Sec. IV B, i.e., flat EDOS, infinitely large electronic bandwidth W_{el} compared to the phonon scale, constant $g_{\mathbf{k},\mathbf{k}'}$, and dispersionless phonons. In particular, the last two imply that the Eliashberg functions do not depend on ξ' . The final result reads as

$$\hat{\Sigma}^R(\omega,t) = \frac{1}{2} \int_{-\infty}^{+\infty} \frac{d\omega'}{2\pi} \int_{-\infty}^{+\infty} \frac{d\nu}{\omega - \omega' - \nu + i0^+} [iF^K(v,t) \check{\mathcal{A}}(\omega',t) + F^\rho(v,t) i\check{\mathcal{G}}^K(\omega',t)], \quad (52a)$$

$$i\hat{\Sigma}^K(\omega,t) = \frac{1}{2} \int_{-\infty}^{+\infty} \frac{d\omega'}{2\pi} \int_{-\infty}^{+\infty} d\nu (2\pi) \delta(\omega - \omega' - \nu) [iF^K(v,t) i\check{\mathcal{G}}^K(\omega',t) + F^\rho(v,t) \check{\mathcal{A}}(\omega',t)], \quad (52b)$$

where

$$\check{\mathcal{A}}(\omega,t) \equiv \int_{-\infty}^{+\infty} d\xi \check{\mathcal{A}}_{\xi}(\omega,t), \quad (53a)$$

$$i\check{\mathcal{G}}^K(\omega,t) \equiv \int_{-\infty}^{+\infty} d\xi i\check{\mathcal{G}}_{\xi}^K(\omega,t) \quad (53b)$$

are *local* electronic spectral and Keldysh functions as obtained by summing over all momentum states:

$$F^\rho(v,t) \equiv F_{0,0}^\rho(v,t) = \nu(0)g^2 \rho(v,t), \quad (54a)$$

$$F^K(v,t) \equiv F_{0,0}^K(v,t) = \nu(0)g^2 \mathcal{D}^K(v,t). \quad (54b)$$

Finally, we find it useful to parametrize the strength of the electron-phonon coupling in terms of the dimensionless *mass enhancement factor* of an ideal Einstein oscillator at equilibrium [18]:

$$\lambda \equiv 2 \int_0^\infty d\nu \frac{F_{\text{ideal}}^\rho(\nu)}{\nu} = \frac{2g^2\nu(0)}{\omega_0}. \quad (55)$$

²In the Migdal-Eliashberg theory literature, it is customary to refer to F^ρ as $\alpha^2 F$. We do not employ this cluttered notation in our treatment.

2. Migdal-Eliashberg self-energy: Normal state

The results of the previous section were worked out for a general Nambu electron propagator. We specialize the result to the normal nonpaired state in this section. Nambu functions are diagonal in the normal state and the Nambu structure of the self-energy and the ensuing KB equations can be simplified. Starting with the general ansatz

$$\hat{\mathcal{G}}_{\xi}^R = \begin{pmatrix} \mathcal{G}_{\xi}^R & 0 \\ 0 & \bar{\mathcal{G}}_{\xi}^R \end{pmatrix}, \quad \hat{\Sigma}^{R/K} = \begin{pmatrix} \Sigma^{R/K} & 0 \\ 0 & \bar{\Sigma}^{R/K} \end{pmatrix}, \quad (56)$$

and using Lemma 1(b) from Appendix B, we find

$$\check{\mathbf{A}}_{\xi}(\omega, t) = \hat{\mathbf{A}}_{\xi}(\omega, t) = \begin{pmatrix} \mathbf{A}_{\xi}(\omega, t) & 0 \\ 0 & \mathbf{A}_{\xi}(-\omega, t) \end{pmatrix}, \quad (57)$$

where we have defined $\mathbf{A}_{\xi}(\omega, t) = -2 \text{Im} \mathcal{G}_{\xi}^R(\omega, t)$ as the normal spectral function. The kinetic energy variable ξ appears as a convenient scalar surrogate for \mathbf{k} after using FSA self-energies [see the discussion after Eq. (51b)]. We have also used Lemma 1(d) to relate the time-reversed spectral function $\bar{\mathbf{A}}_{\xi}(\omega, t) \equiv \text{Im} \bar{\mathcal{G}}_{\xi}^R(\omega, t)$ to $\mathbf{A}_{\xi}(\omega, t)$, i.e., $\bar{\mathbf{A}}_{\xi}(\omega, t) = \mathbf{A}_{\xi}(-\omega, t)$. We further define an unrestricted ansatz for $i\mathcal{G}_{\xi}^K$ in compliance with Lemmas 1(c) and 1(e):

$$i\hat{\mathcal{G}}_{\xi}^K(\omega, t) = \begin{pmatrix} \psi_{\xi}(\omega, t) \mathbf{A}_{\xi}(\omega, t) & 0 \\ 0 & -\psi_{\xi}(\omega, t) \mathbf{A}_{\xi}(-\omega, t) \end{pmatrix}, \quad (58)$$

where $\psi(\omega, t)$ is an *odd real function of ω* that encodes the statistics of electrons in the normal state. For example, in thermal equilibrium, the Kubo-Martin-Schwinger (KMS) boundary condition implies

$$\psi_{\xi}^{\text{eq}}(\omega, t) \rightarrow 1 - 2n_{\text{FD}}(\omega) = \tanh(\beta\omega/2). \quad (59)$$

We further define the *local* electron statistics as

$$\psi(\omega, t) = \frac{1}{2\pi} \int_{-\infty}^{+\infty} d\xi i\mathcal{G}_{\xi}^K(\omega, t). \quad (60)$$

In theory, the $\Sigma^{R/K}$ can be expressed as functionals of ψ , $i\mathcal{D}^K$, and ρ . An explicit formula for $\Sigma^{R/K}[\psi, i\mathcal{D}^K, \rho]$ can be found using Eqs. (52a) and (52b), (54a) and (54b), (58), and the following crucial lemma:

Lemma (\mathcal{G}^R momentum summation formula). Assuming (1) infinite electronic bandwidth limit, and (2) a momentum-independent retarded self-energy as in Fermi surface averaging approximation and local approximation (DMFT), the following identity holds:

$$\int_{-\infty}^{+\infty} d\xi \mathcal{G}_{\xi}^R(\omega, t) = -i\pi. \quad (61)$$

The proof is given in Appendix C. An immediate corollary is

$$\int_{-\infty}^{+\infty} d\xi \mathbf{A}_{\xi}(\omega, t) = 2\pi. \quad (62)$$

Combining Eqs. (52a) and (52b), (54a) and (54b), (58), and (61), we find the sought after explicit self-energy functionals

$$\Sigma^R(\omega, t) = \int_0^{+\infty} d\omega' \int_{-\infty}^{+\infty} dv \left[\frac{N^+(\omega', v; t)}{\omega - \omega' - v + i0^+} + \frac{N^-(\omega', v; t)}{\omega + \omega' - v + i0^+} \right], \quad (63a)$$

$$i\Sigma^K(\omega, t) = \pi \int_{-\infty}^{+\infty} dv \psi(\omega - v, t) iF^K(v, t), \quad (63b)$$

where

$$N^{\pm}(\omega, v; t) \equiv \frac{1}{2} [iF^K(v, t) \pm \psi(\omega, t) F^{\rho}(v)]. \quad (64)$$

It is noteworthy that $\Sigma^{R/K}$ only depends on the *local* electron statistics $\psi(\omega, t)$ and not the ξ response $\psi_{\xi}(\omega, t)$. Finally, Lemmas 3(a) and 3(b) from Appendix B and the above result imply $\bar{\Sigma}^{R/K}(\omega, t) = \Sigma^{R/K}(\omega, t)$, i.e., $\hat{\Sigma}$ is proportional to the identity matrix in the normal state. This result is strictly a consequence of the ideal Migdal limit. One can show $\Sigma^R - \bar{\Sigma}^R \propto 1/W_{\text{el}}$ in a finite-bandwidth model. This completes our discussion of the Migdal-Eliashberg self-energy in the normal state.

3. Floquet-Boltzmann kinetic equation for electrons

An explicit Floquet-Boltzmann kinetic equation can be derived for electrons in the normal state using the result of the previous section and the KB equations. To this end, we write the Keldysh component of Eqs. (33a) and (33b) using FSA self-energy:

$$[+i\partial_{t_1} - \xi] \mathcal{G}_{\xi}^K = \Sigma^R \star \mathcal{G}_{\xi}^K + \Sigma^K \star \mathcal{G}_{\xi}^A, \quad (65)$$

$$[-i\partial_{t_2} - \xi] \mathcal{G}_{\xi}^K = \mathcal{G}_{\xi}^R \star \Sigma^K + \mathcal{G}_{\xi}^K \star \Sigma^A. \quad (66)$$

Subtracting the sides of these equations from one another and performing a Wigner transformation, we find

$$\partial_t i\mathcal{G}_{\xi}^K = \Sigma^R \star \mathcal{G}_{\xi}^K + \Sigma^K \star \mathcal{G}_{\xi}^A - \mathcal{G}_{\xi}^R \star \Sigma^K - \mathcal{G}_{\xi}^K \star \Sigma^A. \quad (67)$$

Integrating both sides over ξ , using Eq. (61), and the definition of the local electron statistics [see Eq. (60)], we find a simple evolution equation for $\psi(\omega, t)$:

$$\partial_t \psi = i\Sigma^K - i(\Sigma^R \star \psi - \psi \star \Sigma^A). \quad (68)$$

As an intermediate consistency check, at equilibrium where $\psi = \tanh(\beta\omega/2)$ and the GM product reduces to an algebraic product, the right-hand side evaluates to $i\Sigma^K(\omega) + 2i \text{Im}[\Sigma^R] \tanh(\beta\omega/2)$ which vanishes in light of the KMS boundary condition. Thus, the thermal state remains stationary as expected.

For a periodically driven system with a slowly varying drive envelope, expanding the convolution integrals using first-order

FGM product formula yields

$$\begin{aligned} \partial_t \psi_{n,m} &= in\Omega \psi_{n,m} + i \Sigma_{n,m}^K[\psi] - i \sum_{n'} \left(\Sigma_{n',-n+n'+m}^R[\psi] \psi_{n-n',n'+m} - \psi_{n',-n+n'+m} \Sigma_{n-n',n'+m}^A[\psi] \right. \\ &+ \frac{i}{2} \partial_\omega \Sigma_{n',-n+n'+m}^R[\psi] \partial_t \psi_{n-n',n'+m} - \frac{i}{2} \partial_t \Sigma_{n',-n+n'+m}^R[\psi] \partial_\omega \psi_{n-n',n'+m} - \frac{i}{2} \partial_\omega \psi_{n',-n+n'+m} \partial_t \Sigma_{n-n',n'+m}^A[\psi] \\ &\left. + \frac{i}{2} \partial_t \psi_{n',-n+n'+m} \partial_\omega \Sigma_{n-n',n'+m}^A[\psi] \right) + \mathcal{O}(\partial_t^2). \end{aligned} \quad (69)$$

The Floquet components of self-energy functionals are worked out easily from Eqs. (63a) and (63b):

$$\Sigma_n^R(\omega; t) = \int_0^{+\infty} d\omega' \int_{-\infty}^{+\infty} dv \left[\frac{N_n^+(\omega', v; t)}{\omega - \omega' - v + i0^+} + \frac{N_n^-(\omega', v; t)}{\omega + \omega' - v + i0^+} \right], \quad (70a)$$

$$i \Sigma_n^K(\omega; t) = \pi \sum_{n'} \int_{-\infty}^{+\infty} dv \psi_{n-n'}(\omega - v; t) i F_{n'}^K(v; t), \quad (70b)$$

where

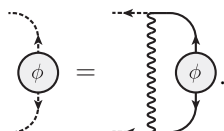
$$N_n^\pm(\omega', v; t) = \frac{1}{2} \left[i F_n^K(v; t) \pm \sum_{n'} \psi_{n-n'}(\omega; t) F_{n'}^\rho(v; t) \right]. \quad (71)$$

The advanced self-energy is readily obtained using the symmetry relation $\Sigma_{n,m}^A(\omega; t) = \Sigma_n^A(\omega - m\Omega/2; t) = [\Sigma_{-n}^R(\omega - m\Omega/2; t)]^* = [\Sigma_{-n,m}^R(\omega; t)]^*$. Self-energies with finite Floquet quasimomentum, e.g., $\Sigma_{n,m}^R(\omega; t)$ are found by shifting $\Sigma_{n,m}^R(\omega; t) \equiv \Sigma_n^R(\omega - m\Omega/2; t)$ [see Eq. (43)].

In the fully self-consistent scheme, one must integrate Eq. (69) together with the previously derived kinetic equations for the lattice displacement and phonon propagator self-consistently. We note that Eq. (69) is an *implicit* integrodifferential equation for $\partial_t \psi_{n,m}$ in disguise due to the presence of derivative terms $\partial_t \Sigma^{R/A}[\psi]$. We will discuss the numerical approach for solving this equation in Appendix F.

V. MIGDAL-ELIASHBERG THEORY OF FLOQUET SUPERCONDUCTING INSTABILITY

We derived a set of tractable evolution equations for the driven system in the normal state. In this section, we derive a criterion to identify the instability of the normal state toward forming a Floquet superconducting state. This criterion follows from a careful linear response analysis as follows: we introduce a small fictitious *pairing potential* (i.e., an off-diagonal self-energy term) to the time-dependent self-energy obtained in the normal state: $\hat{\Sigma}^R(\omega, t) \rightarrow \Sigma^R(\omega, t) \mathbb{I} + \hat{\phi}(\omega, t)$. Here, $\hat{\phi}(\omega, t)$ is off diagonal in the Nambu space. The off-diagonal self-energy, in turn, induces an anomalous (off-diagonal) propagator $\delta \hat{\mathcal{F}}[\hat{\phi}]$ which in turn generates the pairing potential. The introduced pair potential may only persist if and only if $\hat{\Sigma}^R[\hat{\mathcal{G}} + \delta \hat{\mathcal{F}}[\hat{\phi}]] - \hat{\Sigma}^R[\hat{\mathcal{G}}] \equiv \hat{\phi}$. This procedure is shown diagrammatically as



$$(72)$$

Since the self-energy is a linear functional of $\hat{\phi}$, satisfiability of the above equation for a nontrivial $\hat{\phi}$ requires the linear operator $\mathbb{I} - \mathcal{D}\mathcal{G}\mathcal{G}$ to have a nontrivial null space. This operator is precisely the inverse vertex operator that appears in the two-particle propagator $\sim \mathcal{G}\mathcal{G}(\mathbb{I} - \mathcal{D}\mathcal{G}\mathcal{G})^{-1}$. This pairing condition is formally equivalent to requiring a zero-energy pole in the two-particle propagator, the well-known Thouless criterion for spontaneous symmetry breaking [54]. The precise condition for a driven nonequilibrium system is complicated due to nonequilibrium propagators and Floquet bands, and requires a careful implementation of the outlined steps, which is the goal of the next sections. As a first step, we will work out the pairing instability criterion for an arbitrary normal state. The results will be used to find the pairing condition for quasisteady Floquet states.

A. Pairing instability criterion for arbitrary nonequilibrium states

We start the analysis by revisiting the KB equations for the retarded Nambu propagator using the FSA self-energy and in the Wigner representation

$$[+(i/2) \partial_t + \omega] \hat{\mathcal{G}}_\xi^R(\omega, t) - \xi \hat{\sigma}_z \hat{\mathcal{G}}_\xi^R(\omega, t) = \mathbb{I} + [\hat{\Sigma}^R \star \hat{\mathcal{G}}_\xi^R](\omega, t), \quad (73a)$$

$$[-(i/2) \partial_t + \omega] \hat{\mathcal{G}}_\xi^R(\omega, t) - \xi \hat{\mathcal{G}}_\xi^R(\omega, t) \hat{\sigma}_z = \mathbb{I} + [\hat{\mathcal{G}}_\xi^R \star \hat{\Sigma}^R](\omega, t). \quad (73b)$$

As discussed in the earlier remarks, we assume the following ansatz at the onset of pairing:

$$\begin{aligned} \hat{\Sigma}^R[\phi](\omega, t) &= \Sigma^R(\omega, t) \mathbb{I} + \hat{\phi}(\omega, t), \\ \hat{\mathcal{G}}_\xi^R[\phi](\omega, t) &= \hat{\mathcal{G}}_\xi^R(\omega, t) + \delta \hat{\mathcal{F}}_\xi^R[\phi](\omega, t) + \mathcal{O}(\phi^2), \\ \hat{\mathcal{G}}_\xi^K[\phi](\omega, t) &= \hat{\mathcal{G}}_\xi^K(\omega, t) + \psi_\xi(\omega, t) \delta \hat{\mathcal{A}}_\xi[\phi](\omega, t) + \mathcal{O}(\phi^2), \end{aligned} \quad (74)$$

where $\hat{\phi}$ is the infinitesimal pairing potential, $\hat{\mathcal{G}}_\xi^{R/K}$ and $\Sigma^R \mathbb{I}$ denote the unperturbed Nambu propagators and self-energy in the normal state, respectively, ψ_ξ is the electron statistics in the unperturbed normal state [see Eq. (58)], and $\delta \hat{\mathcal{F}}_\xi^R[\phi]$

and $\delta\hat{A}_\xi[\phi]$ denote the off-diagonal linear response of the retarded propagator and the spectral function, respectively. Using Lemma 1(b) of Appendix B, we have

$$\delta\check{A}_\xi[\phi](\omega, t) = i\hat{\sigma}_x[\delta\hat{\mathcal{F}}_\xi^R[\phi](\omega, t) - \delta\hat{\mathcal{F}}_\xi^R[\phi](\omega, t)^*]\hat{\sigma}_x. \quad (75)$$

Here, we have assumed that the pairs formed at the onset of transition have the same statistics ψ_ξ as the normal electrons. Inserting the ansatz in Eqs. (73a) and (73b), summing the sides, and keeping terms to linear order in $\hat{\phi}$, we find

$$\begin{aligned} 2\omega\delta\hat{\mathcal{F}}_\xi^R[\phi] - \xi\{\hat{\sigma}_z, \delta\hat{\mathcal{F}}_\xi^R[\phi]\} \\ = \hat{\phi} \star \hat{\mathcal{G}}_\xi^R + \hat{\mathcal{G}}_\xi^R \star \hat{\phi} + \Sigma^R \star \delta\hat{\mathcal{F}}_\xi^R[\phi] + \delta\hat{\mathcal{F}}_\xi^R[\phi] \star \Sigma^R. \end{aligned} \quad (76)$$

Since $\delta\hat{\mathcal{F}}_\xi^R$ is fully off diagonal, $\{\hat{\sigma}_z, \delta\hat{\mathcal{F}}_\xi^R\} = 0$. Integrating both sides of Eq. (76) over ξ , using Eq. (61) to replace the ξ -summed normal retarded propagators with the universal value of $-i\pi$, we find

$$2\omega\delta\mathcal{F}^R[\phi] = -2\pi i\phi + \Sigma^R \star \delta\mathcal{F}^R[\phi] + \delta\mathcal{F}^R[\phi] \star \Sigma^R. \quad (77)$$

Without the loss of generality, we have assumed $\hat{\phi} = \phi\hat{\sigma}_x$ and $\delta\hat{\mathcal{F}}^R[\phi] = \delta\mathcal{F}^R[\phi]\hat{\sigma}_x$ to distill the Nambu matrix structure on the last equation.

Solving the equation above for arbitrary $\Sigma(\omega, t)$ and $\phi(\omega, t)$ is a formidable task due to the intricate differential structure of the GM product formula. However, we will show later that it can be reduced to a simpler algebraic structure using the properties of Floquet-Boltzmann states. Here, we proceed with the general observation that $\delta\mathcal{F}^R[\phi]$, and subsequently $\delta\check{A}[\phi]$ as given by Eq. (75), are computable linear functionals of ϕ . Projecting out the off-diagonal component of the retarded Migdal-Eliashberg self-energy [Eq. (52a)], we find

$$\begin{aligned} \phi(\omega, t) = \frac{1}{4} \int_{-\infty}^{+\infty} \frac{d\omega'}{2\pi} \int_{-\infty}^{+\infty} \frac{dv}{\omega - \omega' - v + i0^+} \{iF^K(v, t) \\ \times \text{Tr}[\hat{\sigma}_x \delta\check{A}[\phi](\omega', t)] + F^\rho(v, t) \text{Tr}[\hat{\sigma}_x i\delta\check{\mathcal{G}}^K(\omega', t)]\}. \end{aligned} \quad (78)$$

This is the sought after self-consistency relation between the pairing potential and the induced anomalous response. Equation (75) implies $\text{Tr}[\hat{\sigma}_x \delta\check{A}_\xi[\phi](\omega, t)] = +4 \text{Im} \delta\mathcal{F}_\xi^R[\phi](\omega, t)$. Furthermore, Lemma 1(d) of Appendix B implies that this quantity is a real odd function of ω . These considerations allow us to simplify the pairing self-consistency condition (78) to

$$\phi(\omega, t) = \int_0^{+\infty} \frac{d\omega'}{\omega'} K(\omega, \omega'; t) \Delta[\phi](\omega', t), \quad (79)$$

where

$$\Delta[\phi](\omega, t) \equiv -\frac{\omega}{\pi} \text{Im} \delta\mathcal{F}^R[\phi](\omega, t), \quad (80a)$$

$$\begin{aligned} K(\omega, \omega'; t) \equiv \int_{-\infty}^{+\infty} dv \left[\frac{N^-(\omega', v; T)}{\omega + \omega' - v + i0^+} \right. \\ \left. - \frac{N^+(\omega', v; t)}{\omega - \omega' - v + i0^+} \right]. \end{aligned} \quad (80b)$$

Equation (79) is a functional eigenvalue equation for $\phi(\omega, t)$. As mentioned earlier, the paired state is stable if and only if Eq. (79) admits a nontrivial solution for $\phi(\omega, t)$.

B. Pairing instability criterion for quasisteady Floquet states

As mentioned earlier, solving Eq. (77) for arbitrary nonequilibrium states is a challenging task and requires resorting to numerical methods in general. This task is significantly simpler in special cases such as stationary states where all time derivatives vanish, or quasisteady Floquet states where the Fourier amplitudes of all involved quantities are approximately stationary. In both cases, Eq. (77) can be cast into an algebraic equation and be solved either numerically or by perturbation. To study the case of quasisteady Floquet states, we take a Fourier transform of the sides of Eq. (77) in t and neglect the time derivatives of Fourier amplitudes in convolutions. Physically, the latter is justified if the pair formation rate is faster than the macroscopic time scale over which the quasistationary Floquet-Boltzmann state evolves. Replacing the GM products appearing in the right-hand side of Eq. (77) with the leading-order FGM product formula, we find

$$\begin{aligned} (2\omega - m\Omega)\delta\mathcal{F}_{n,m}^R(\omega; t) \\ = -2\pi i\phi_{n,m}(\omega; t) \\ + \sum_{n'} \Sigma_{n', m-n+n'}^R(\omega; t) \delta\mathcal{F}_{n-n', m+n'}^R(\omega; t) \\ + \sum_{n'} \Sigma_{n', m+n-n'}^R(\omega; t) \delta\mathcal{F}_{n-n', m-n'}^R(\omega; t). \end{aligned} \quad (81a)$$

The FGM product formula mixes different Floquet quasimomentum states of Σ^R and $\delta\mathcal{F}^R$. We have further introduced an arbitrary Floquet quasimomentum label by shifting $\omega \rightarrow \omega - m\Omega/2$ on both sides toward a more uniform notation. The above equation can be thought of as an infinite-dimensional linear system for $\delta\mathcal{F}_{n,m}^R$. In practice, one truncates Floquet bands and quasimomenta to obtain a proper finite linear system (e.g., see Ref. [22]). The finite system is then solved numerically or by perturbation to find an explicit linear relation between the Floquet components of $\delta\mathcal{F}$ and ϕ :

$$\delta\mathcal{F}_{n,m}^R(\omega; t) = \sum_{n', m'} \mathbf{Q}_{n', m'}^{n, m}(\omega; t) \phi_{n', m'}(\omega; t). \quad (81b)$$

We note that $\mathbf{Q}_{n', m'}^{n, m}(\omega; t)$ only depends on the unperturbed retarded self-energy in the normal state. Diagrammatically, this step is equivalent to attaching the pair propagator to ϕ in the right-hand side of Eq. (72). This expression, together with Eq. (80a), yields the sought after explicit relation between the gap and the pairing potential:

$$\begin{aligned} \Delta_n(\omega; t) = \frac{i\omega}{2\pi} \sum_{n', m'} \{ \mathbf{Q}_{n', m'}^{n, 0}(\omega; t) \phi_{n', m'}(\omega; t) \\ - [\mathbf{Q}_{n', m'}^{-n, 0}(\omega; t)]^* \phi_{n', m'}^*(\omega; t) \}. \end{aligned} \quad (82)$$

Taking a Fourier transform of the sides of Eq. (79) in t and neglecting time derivatives as before, we find

$$\phi_{n',m'}(\omega;t) = \sum_{n''} \int_0^{+\infty} \frac{d\omega'}{\omega'} K_{n'',m'}(\omega,\omega';t) \Delta_{n'-n''}(\omega';t), \quad (83)$$

where

$$K_{n,m}(\omega,\omega';t) = \int_{-\infty}^{+\infty} dv \left[\frac{N_n^-(\omega',v;t)}{\omega - m\Omega/2 + \omega' - v + i0^+} - \frac{N_n^+(\omega',v;t)}{\omega - m\Omega/2 - \omega' - v + i0^+} \right]. \quad (84)$$

Plugging $\phi_{n',m'}$ from Eq. (83) into Eq. (82) yields the final functional eigenvalue equation for the Floquet gap at the onset of pairing:

$$\begin{aligned} \Delta_n(\omega;t) = & \frac{i\omega}{2\pi} \sum_{n',n'',m'} \left\{ \mathbf{Q}_{n',m'}^{n,0}(\omega;t) \int_0^{+\infty} \frac{d\omega'}{\omega'} K_{n'',m'}(\omega,\omega';t) \Delta_{n'-n''}(\omega';t) \right. \\ & \left. - [\mathbf{Q}_{n',m'}^{-n,0}(\omega;t)]^* \int_0^{+\infty} \frac{d\omega'}{\omega'} K_{n'',m'}^*(\omega,\omega';t) \Delta_{n'-n''}^*(\omega';t) \right\}. \end{aligned} \quad (85)$$

It is worthwhile to take a moment and study this equation in some detail. We recall that $\mathbf{Q}_{n',m'}^{n,0}$ is derived from the normal-state self-energy and relates the anomalous response to the pairing potential [see Eq. (81b)]. Thus, this quantity brings in the physics of quasiparticle propagation in the normal state such as lifetime and residue. On the other hand, the phonon propagator enters through $K_{n,m}$ and, therefore, it brings in the retarded phonon-mediated attraction between the quasiparticles [see Eqs. (84) and (71)].

Finally, let us consider the static nondriven limit of Eq. (85) as a consistency check where all Floquet indices and summations can be dropped. In this limit, Eq. (81a) admits a simple algebraic solution

$$\delta\mathcal{F}(\omega) = -\frac{i\pi}{\omega - \Sigma^R(\omega)} \phi(\omega), \quad (86)$$

implying $\mathbf{Q}_{n',m'}^{n,0}(\omega) = -i\pi \delta_{n,0} \delta_{n',0} \delta_{m',0} [\omega - \Sigma^R(\omega)]^{-1}$. Plugging this into Eq. (85), we find

$$\Delta(\omega) = \text{Re} \left[\frac{1}{Z(\omega)} \int_0^{+\infty} \frac{d\omega'}{\omega'} K(\omega,\omega') \Delta(\omega') \right], \quad (87)$$

where $Z(\omega) = [\omega - \Sigma^R(\omega)]/\omega$ as it is usually defined in the context of Migdal-Eliashberg theory. This coincides with the result obtained earlier by Scalapino, Schrieffer, and Wilkins [38] for equilibrium systems. Our result is a proper generalization of the static Migdal-Eliashberg pairing criterion to arbitrary nonequilibrium states [Eq. (79)], and particularly to Floquet states [Eq. (85)].

In practice, we monitor the eigenvalue spectrum of the linear functional posed by Eq. (85) as the system evolves in the normal state. The normal state is deemed unstable as soon as the lowest eigenvalue crosses zero. The same procedure applies to equilibrium states, where one calculates the normal-state self-energy of electrons at different temperatures and decreases the temperature until the lowest eigenvalue crosses zero.

VI. REVISITING THE PROBLEM: RESULTS FROM THE FLOQUET-MIGDAL-ELIASHBERG THEORY

The machinery of Floquet-Migdal-Eliashberg (FME) quantum kinetics allows us to fill out the missing details in the

preliminary analysis given in Sec. III. In particular, we can study the role of competing factors such as parametric phonon generation and the heating of electrons in order to assess whether the mechanism laid out in Sec. III persists in transient dynamics.

At this point, we have developed all the necessary tools to solve the problem using the full FME formalism (Fig. 7). As outlined above, the electron-phonon system is initially prepared in an equilibrium normal state with temperature $T_i > T_c$, where T_c is the critical superconducting transition temperature for the given system parameters. The drive is smoothly ramped up according to

$$|F(t)|^2 = \frac{I_0}{2} [1 + \tanh(t/\tau_{\text{drv}})] \cos^2(\Omega_{\text{drv}} t), \quad (88)$$

where I_0 denotes the intensity of the drive. We restrict our numerical analysis to weak and intermediate couplings where the phononic and electronic quantities can be calculated iteratively as described below.

As a first step, the electrons are assumed to remain in the equilibrium state, effectively providing a fixed-temperature Ohmic quantum bath $\Pi_\ell^{(0)}(\omega)$ for the phonons. Explicit expressions for $\Pi_\ell^{(0)}$ are given in Appendix E 1. The Floquet-Boltzmann equations for the lattice displacement $\{\varphi_n(t)\}$ and phonon propagators $\{i\mathcal{D}_n^K(\omega;t), \rho_n(\omega;t)\}$ are then numerically integrated forward in time as described in Appendix F 1. Subsequently, the Floquet-Boltzmann equations for the energy distribution of electrons $\{\psi_n(\omega;t)\}$ are numerically solved as described in Appendix F 2. If deemed necessary, this two-pass iterative calculation is looped until a self-consistent nonequilibrium solution is obtained for both phonons and electrons. For our choice of parameters, we found additional iterations to be unnecessary by the virtue of the large separation of energy scales between phonons and electrons and weak coupling. Finally, we study the FME pairing instability condition throughout the evolution in order to assess whether the normal state exhibits the pairing instability at some time.

We remark that the system is assumed to evolve in the normal state throughout the simulation. The present formalism detects the instability toward Cooper pairing. Studying the full Floquet superconducting gap formation and its dynamics is a

more challenging problem and is better suited to be studied via a Floquet extension of the time-dependent Landau-Ginzburg (TDGL) formalism.

We present the results in two stages. As a first step, in order to gain insight into parameter regimes of maximally enhanced superconductivity, we hold the electrons in thermal states with different temperatures (e.g., by coupling them to a large and infinitely efficient heat bath). We proceed by letting the driven phonons settle to a stationary Floquet driven-dissipative state and calculate the T_c of electrons on its backdrop. This procedure is similar to calculating T_c in equilibrium by studying the eigenvalue spectrum of Eq. (85), however, using the driven phonon propagators.

Finally, we study the full evolution of the coupled system by allowing the electrons to evolve on par with phonons. This allows us to investigate the transient nature of the superconducting instability. We find that the heating of electrons destroys the instability at late times and stabilizes the normal state as seen in the experiments [12].

Choice of physical parameters. The trimmed-down model is fully specified by a few physical parameters: electron-phonon coupling g , electronic density of states at the Fermi level $\nu(0)$, optical phonon frequency ω_0 , the phenomenological damping of the coherent lattice displacement γ_0 , and the drive coupling strength Λ . We trade g and $\nu(0)$ with the mass enhancement factor at equilibrium λ_{eq} and local phonon damping γ_ℓ . These dimensionless quantities are defined in Eqs. (55) and (E17) and we quote them again here for reference:

$$\lambda_{\text{eq}} \equiv \frac{2g^2\nu(0)}{\omega_0}, \quad \gamma_\ell \equiv 4\pi g^2\nu(0)^2. \quad (89)$$

We set $\lambda = 0.5$ and $\gamma_\ell = 0.2$ in the numerics, which correspond to typical values for fulleride superconductors [39]. We study cubic and quartic nonlinearities separately. The

majority of the results are presented for a cubic nonlinearity. As we argued earlier in Sec. III B, both types of nonlinearity lead to qualitatively similar phenomena. We set $\kappa_3 = 0.1 \omega_0$, $\kappa_4 = 0$ for ‘‘cubic results’’, and $\kappa_3 = 0$, $\kappa_4 = 0.1 \omega_0$ for ‘‘quartic results’’. These values are expected to reflect the typical intrinsic lattice nonlinearities.

Normalization constants. Quantities with the dimension of energy are presented in the units of Ω_0 , the renormalized phonon frequency at equilibrium defined in Eq. (F2), and the time axes are scaled with respect to τ_{ph} , the renormalized period of phonons at equilibrium:

$$\Omega_0 \equiv \sqrt{\omega_0^2 + 2\omega_0\bar{\omega}_L + 2\omega_0 U_0}, \quad \tau_{\text{ph}} \equiv \frac{2\pi}{\Omega_0}. \quad (90)$$

Here, $\bar{\omega}_L$ is the effective Lamb shift of phonons as a matter of coupling to electrons which can be neglected in the weak-coupling regime. U_0 is determined by self-consistently solving the set of equations given in Eq. (F1) and represents the phonon frequency correction due to lattice nonlinearities. Finally, we parametrize the fully ramped-up drive amplitude by the dimensionless quantity \mathcal{A} defined as

$$\mathcal{A} \equiv \lim_{t \rightarrow \infty} \frac{\Lambda}{2\omega_0} I_0 F_{\text{env}}^2(t) = \frac{\Lambda I_0}{2\omega_0}, \quad (91)$$

and set $\tau_{\text{drv}} = 5 \tau_{\text{ph}}$ in Eq. (88).

Notation. We often discuss period-averaged quantities along with their temporal variances, respectively defined as

$$\begin{aligned} \langle O(t) \rangle &\equiv \frac{\Omega_{\text{drv}}}{\pi} \int_{-\pi/(2\Omega_{\text{drv}})}^{+\pi/(2\Omega_{\text{drv}})} d\tau O(t + \tau), \\ \text{Var}[O(t)] &\equiv \frac{\Omega_{\text{drv}}}{\pi} \int_{-\pi/(2\Omega_{\text{drv}})}^{+\pi/(2\Omega_{\text{drv}})} d\tau [O(t + \tau) - \langle O(t) \rangle]^2, \end{aligned} \quad (92)$$

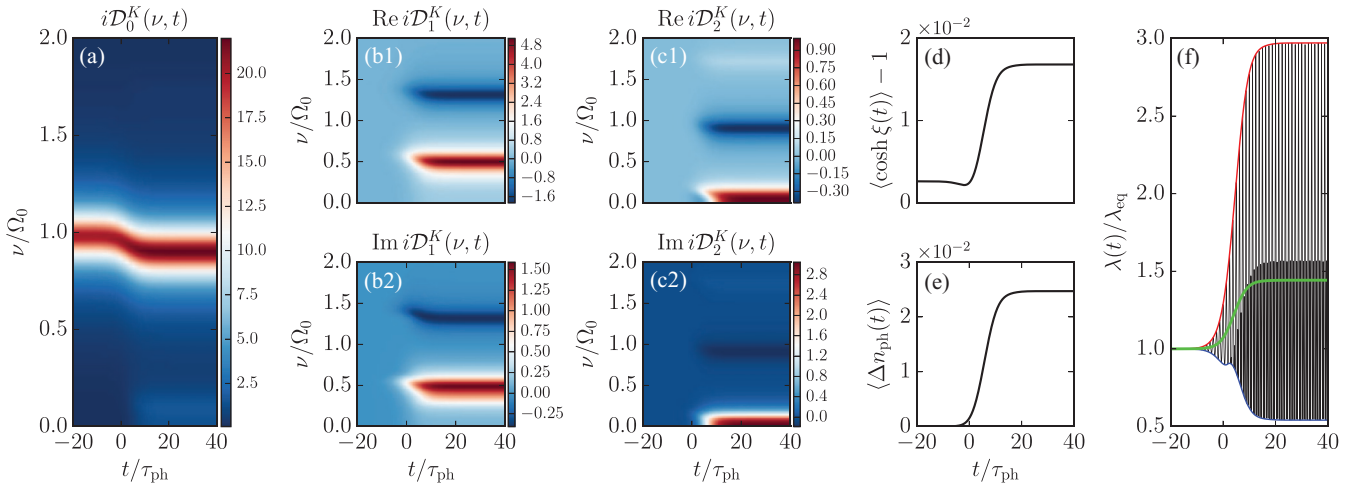


FIG. 9. Evolution of phonon propagators in response to a ramped-up external drive for drive frequency $\Omega_{\text{drv}} = 0.4 \Omega_0$ and maximum drive amplitude $\mathcal{A} = 0.75$. The physical parameters are set to $\kappa_3 = 0.1$, $\kappa_4 = 0$, and $\gamma_\ell = 0.2 \Omega_0$. The leftmost panel shows $n = 0$ (period-averaged) Keldysh phonon propagator. The red-shift of the phonon peak is clearly noticeable. The next two columns show the real and imaginary parts of $n = 1, 2$ propagators. Notice the absence of a single quasiparticle peak. Panels (d) and (e) show the period-averaged squeezing correlations and the density of phonon excitations, respectively. Both quantities increase as the external field is ramped up. Finally, panel (f) shows the time-dependent mass enhancement factor as defined in the text, along with its time average (green solid line) and the lower and upper envelopes (blue and red lines, respectively). Notice the significant increase in the mass enhancement factor, as well as its high-amplitude oscillations.

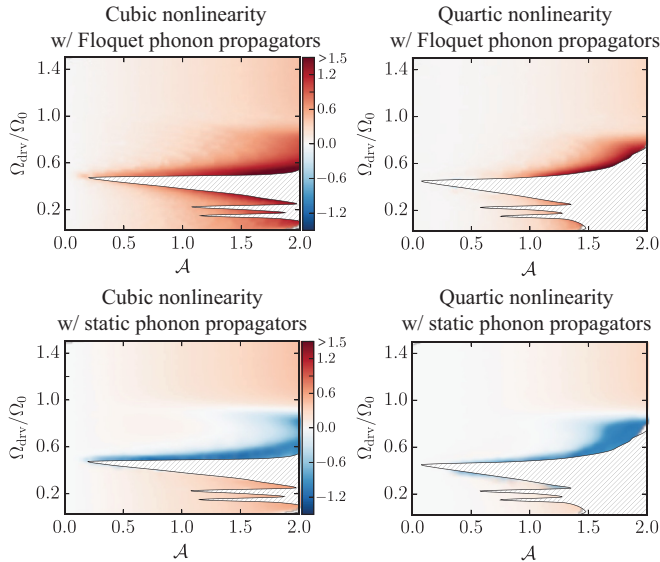


FIG. 10. The relative change of Floquet superconducting transition temperature with respect to equilibrium, $T_c^{\text{Floq}}/T_c^{\text{eq}} - 1$, in the equilibrium electron approximation. The left and right columns show the results for cubic and quartic nonlinearities $\kappa_3 = 0.1 \Omega_0$, $\kappa_4 = 0$ and $\kappa_3 = 0$, $\kappa_4 = 0.1 \Omega_0$, respectively. The top row is obtained using full Floquet phonon propagators whereas $n > 0$ Floquet components (dynamical effects) are neglected in the bottom row. The electrons are kept in a thermal state at temperature $T = 0.04 \Omega_0$.

where $O(t)$ is an arbitrary observable. Note that the effective drive period is π/Ω_{drv} since the principal harmonic of all observables is $2\Omega_{\text{drv}}$ [see the discussion after Eq. (39)]. If $O(t)$ is given as a Fourier series with slowly varying amplitudes, i.e., $O(t) = \sum_{n=-\infty}^{\infty} O_n(t) e^{2ni\Omega_{\text{drv}}t}$, then $\langle O(t) \rangle = O_0(t)$ and $\text{Var}[O(t)] \equiv \sum_{n=1}^{\infty} |O_n(t)|^2$.

A. Stage I: Driven phonons, thermal electrons

Figure 9 shows a typical example of phonon propagators subject to nearly resonant drive in the presence of lattice nonlinearities. Figure 9(a) shows a heat map of the period-averaged Keldysh phonon propagator $iD_{n=0}^K(\nu; t)$ at a function of relative frequency ν and COM time t . The most prominent feature is the red-shift of the phonon peak frequency. The red-shift is a direct consequence of the lattice

nonlinearity: with a cubic nonlinearity $\sim \kappa_3 \hat{\phi}^3$, the drive shifts the equilibrium position of the lattice on average, producing a frequency renormalization $\Delta\omega_{\text{ph}}^2 \sim \kappa_3 \langle \hat{\phi} \rangle$. For a nearly resonant drive, nonlinear effects dominate the value of $\langle \hat{\phi} \rangle$ such that $\text{sign}[\langle \hat{\phi} \rangle] = -\text{sign}(\kappa_3)$. As a result, $\Delta\omega_{\text{ph}}^2 < 0$ regardless of the sign of κ_3 for a strong nearly resonant drive. In other words, the cubic nonlinearity always softens the lattice. This phenomenon resembles the usual physics of thermal expansion where the drive plays the role of heating.

Figures 9(b1) and 9(b2) and 9(c1) and 9(c2) show the higher Floquet components of the Keldysh phonon propagator, both of which show emergent features as the drive is ramped up. It is noticed that $|iD_2^K| < |iD_1^K|$ suggesting that the role of higher Floquet bands becomes increasingly smaller. Most strikingly, it is noticed that $n > 0$ Floquet phonons do not admit a single coherent peak in contrast to the $n = 0$ case. As a consequence, Eqs. (45a)–(46b) do not admit a reliable Boltzmann “quasiparticle” limit, justifying our usage of the more cumbersome *quantum* kinetic formalism.

One consequence of the drive is parametric generation of phonons [46] and squeezing of lattice momentum fluctuation [28]. Figures 9(d) and 9(e) show the evolution of these quantities as a function of COM time t . Appendix D shows how these quantities can be calculated from $iD^K(\omega, t)$. As expected, both of these observables significantly increase as the drive is ramped up. The emergence of squeezed states is a well-known hallmark of parametrically driven harmonic oscillators. Finally, Fig. 9(f) shows the instantaneous mass enhancement factor $\lambda(t)$ defined as

$$\lambda(t) = \omega_0 \lambda_{\text{eq}} \sum_n \int_0^\infty \frac{d\nu}{\nu} \rho_n(\nu; t) e^{2in\Omega_{\text{drv}}t}. \quad (93)$$

This quantity plays a similar role in the Migdal-Eliashberg theory as $\nu(0)U(t)$ in the BCS theory (the latter was defined in Sec. III). For instance, $T_c \approx \omega_0 e^{-1/\lambda_{\text{eq}}}$ in the equilibrium Migdal-Eliashberg theory [18]. It is noticed that $\lambda(t)$ has a strong oscillatory component. The period average of $\lambda(t)$ during one drive period and the lower and upper envelopes are shown as green, blue, and red solid lines.

The Floquet superconducting transition temperature T_c^{Floq} can be determined for each choice of Ω_{drv} and \mathcal{A} by calculating the eigenvalue spectrum of the FME gap functional [Eq. (85)],

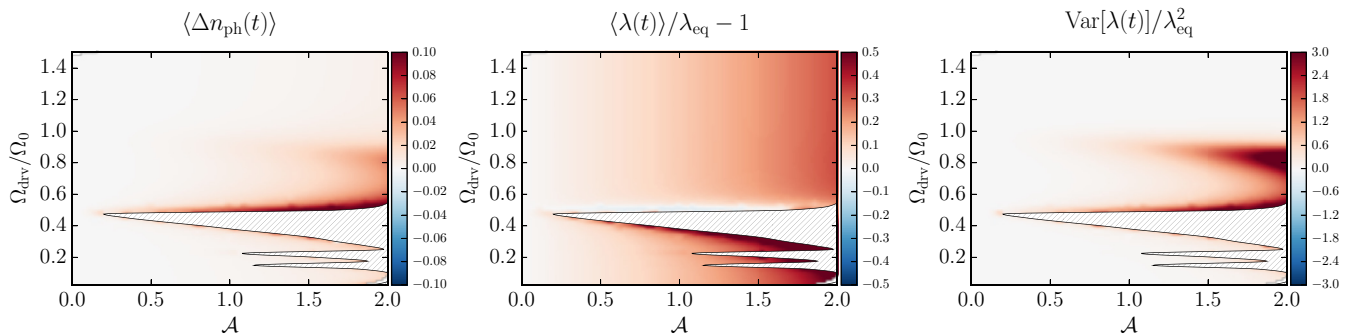


FIG. 11. Density of phonon excitations (left), period average (middle), and time variance (right) of the mass enhancement factor. The electrons are kept in a thermal state at temperature $T = 0.04 \Omega_0$. These quantities are calculated in the stationary driven-dissipative state of phonons.

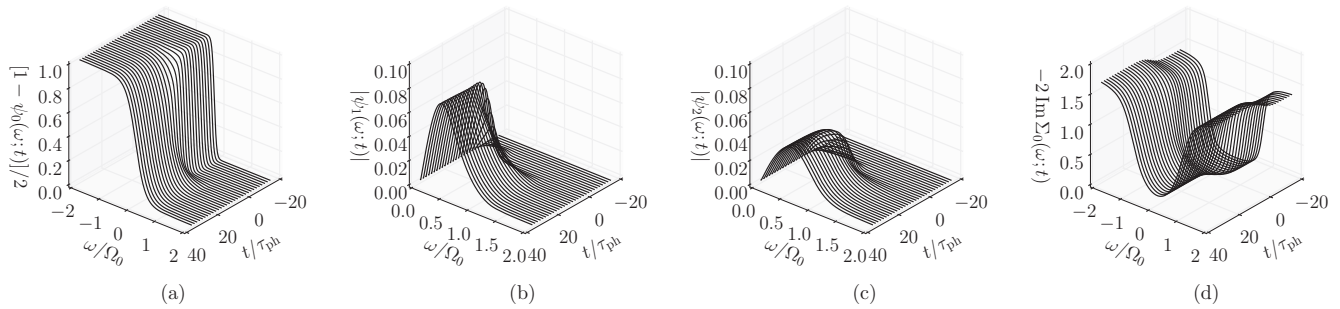


FIG. 12. Time evolution of the energy statistics of electrons for $\Omega_{\text{drv}} = 0.4 \Omega_0$, $\mathcal{A} = 0.75$, and $\tau_{\text{drv}} = 5 \tau_{\text{ph}}$. From left to right, the plots show the period-averaged ($n = 0$) energy statistics, its first and second Floquet components, and the period-averaged scattering rate $\langle \Gamma(\omega, t) \rangle \equiv -2i \text{Im}[\Sigma_{n=0}^R(\omega; t)]$ of electrons. The heating of electrons is noticeable in (a) as the drive is ramped up, as well as the increase in the scattering rate in (d).

eigs $_{\Delta}$, for different electronic temperatures and locating the first zero crossing of the lowest eigenvalue mineigs $_{\Delta}$.

Figure 10 shows the results separately for cubic and quartic nonlinearities. The top row corresponds to a calculation using full Floquet phonon propagators. The bottom row is obtained using only $n = 0$ (period-averaged) phonon propagators. Strong driving near parametric resonances leads to the instability of the lattice due to nonlinearities. This stems from our choice of $\mathcal{V}^{\text{ph}}(\varphi)$ [see Eq. (2)], which is only valid for low-amplitude deformations and becomes unphysical for large deformations. These unstable regions are hatched in the heat map plots and indeed coincide with the three first parametric resonances at $\Omega_{\text{drv}}/\Omega_0 \approx \frac{1}{2}, \frac{1}{4}, \frac{1}{8}$.

The full Floquet result (top row) shows a dramatic enhancement of T_c , reaching beyond three times the equilibrium value near the resonances. Neglecting the ac components, only a moderate enhancement of T_c is found, and only away from the resonances. In particular, T_c is suppressed above the main resonance in the static approximation in contrast to the full Floquet result. This finding is strikingly similar to the analytic Floquet BCS analysis of Sec. III A (see Fig. 6).

To shed light on this finding, we have plotted the density of excited phonons $\langle \Delta n_{\text{ph}}(t) \rangle$ as well as the mean and variance of $\lambda(t)$ during a drive period as a function of Ω_{drv} and \mathcal{A} in Fig. 11. It is noticed that (1) $\langle \lambda(t) \rangle$ is enhanced and suppressed below and above the main resonance, respectively, similar

to the analysis of Sec. III and as summarized in Fig. 5; (2) both $\langle \Delta n_{\text{ph}} \rangle$ and $\text{Var}[\lambda(t)]$ increase significantly above the main resonance. Neglecting $n > 0$ components of the phonon propagator and neglecting $\text{Var}[\lambda(t)]$ go hand in hand. The high density of phonon excitations and the suppression of $\langle \lambda(t) \rangle$ above the resonance imply decreased quasiparticle lifetime and electron-electron attraction, respectively, both of which are unfavorable for Cooper pairing. This explains suppression of T_c above the main resonance in the static approximation. Away from the resonances, the moderate enhancement of $\langle \lambda(t) \rangle$, which has its roots in the phonon frequency red-shift and is present in the static approximation, explains the moderate enhancement of T_c . Finally, we remark that including $n > 0$ components brings in large $\text{Var}[\lambda(t)]$. In the example shown in Fig. 9(f), the upper envelope of $\lambda(t)$ is nearly three times as large as λ_{eq} . As we argued earlier in Sec. III A, T_c is a convex functional of the interaction parameter in the weak-coupling limit such that temporal variation of interaction can increase T_c even if the period average remains fixed or even decreases.

B. Stage II: Driven phonons, evolving electrons

The notion of superconducting transition temperature is only well defined in thermal states. Once the electrons are allowed to evolve as a matter of coupling to phonons, a different diagnostic will be needed to assess the enhancement or suppression of the superconducting transition. Here, we

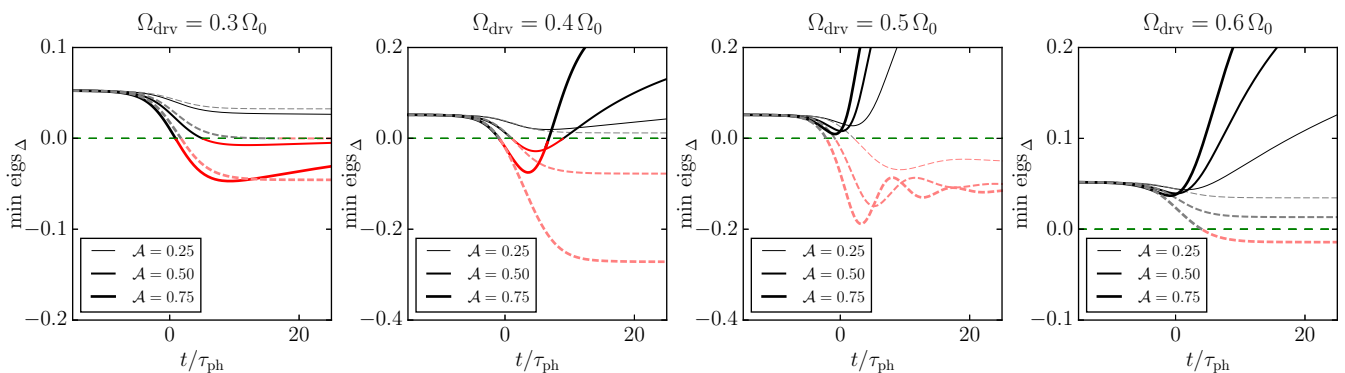


FIG. 13. Assessment of the Floquet-Migdal-Eliashberg (FME) pairing condition for a ramped-up external drive with different frequencies and amplitudes. The red segments indicate regions where the lowest eigenvalue of the FME gap functional is negative, signaling the pairing instability. The dashed lines show the hypothetical case if the electrons were to remain in their initial thermal state (no heating). The nonlinearity is cubic, the initial temperature is set to $T_i = 0.04 \Omega_0 \simeq 1.2 T_c^{\text{eq}}$, and the physical parameters are chosen as described in Sec. VI.

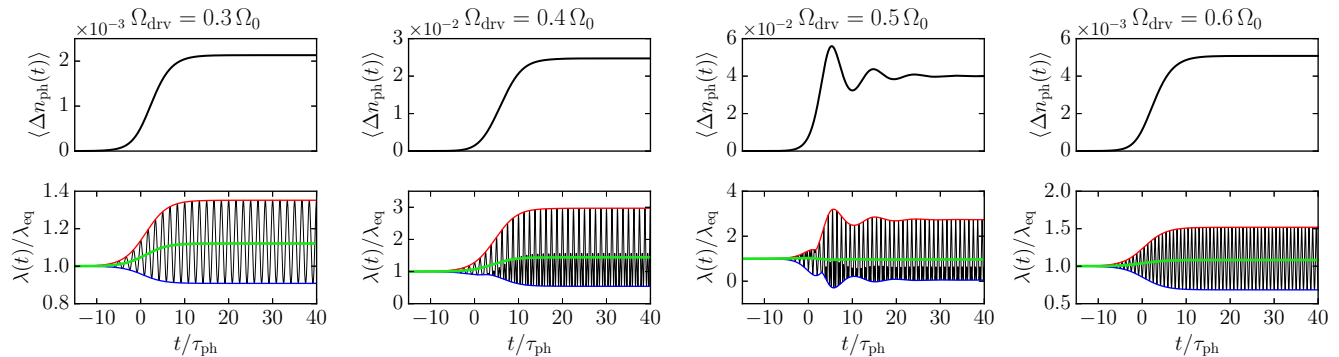


FIG. 14. Evolution of the density of phonon excitations $\langle \Delta n_{\text{ph}}(t) \rangle$ and instantaneous mass enhancement factor $\lambda(t)$ for different drive frequencies and amplitudes. In the bottom row, the green, blue, and red lines correspond to the period-averaged, lower, and upper envelopes of $\lambda(t)$. The nonlinearity is cubic, the initial temperature is $T_i = 0.04 \Omega_0 \simeq 1.2 T_c$. The choice physical parameters are as given in Sec. VI.

attempt to model a realistic experimental scenario: we prepare the electron-phonon system in $T_i > T_{\text{eq}}$, ramp up the drive, and calculate the ensuing nonequilibrium dynamics of phonons and electrons. Since $T_i > T_c$ in the beginning, the lowest eigenvalue of the FME gap functional begins as a positive value. Whether it remains positive throughout the evolution or crosses zero at some point is our diagnostic. This allows us to study the instability of the normal state toward Cooper pair formation but does not describe the physics of gap formation. The latter can be addressed with an extended formalism based on the present developments.

Figure 12 shows an example of the evolution of the Floquet components of the ξ -summed (local) energy statistics of electrons $\{\psi_n(\omega; t)\}$ defined in Eq. (60), along with their period-averaged scattering rate $\langle \Gamma(\omega, t) \rangle \equiv -2i \text{Im}[\Sigma_{n=0}^R(\omega; t)]$. The prominent features are (1) the heating of electrons, manifested as the decreased slope of $\psi_0(\omega; t)$ at $\omega = 0$ as the drive is ramped up, (2) emergence of electrons in $n > 0$ Floquet bands, and (3) increased (decreased) spectral broadening (lifetime) of quasiparticles.

Figure 13 shows the evolution of the lowest eigenvalue of the FME gap functional, $\min \text{eigs}_{\Delta}$, for $\Omega_{\text{drv}}/\Omega_0 = 0.3, 0.4, 0.5, 0.6$ and $\mathcal{A} = 0.25, 0.50, 0.75$. The nonlinearity is cubic and the choice of physical parameters is as described

in the introductory remarks of this section, implying $T_c^{\text{eq}} \simeq 0.034 \Omega_0$. The initial temperature chosen as $T_i = 0.04 \Omega_0 \simeq 1.2 T_c^{\text{eq}}$. The dashed lines show the hypothetical case where the electrons are kept at T_i (no heating). Red segments indicate where $\min \text{eigs}_{\Delta} < 0$. The most favorable outcome occurs for lower frequency driving, e.g., $\Omega_{\text{drv}} = 0.3 \Omega_0$, where the pairing instability persists for a long time. In all cases, heating of electrons tends to stabilize the normal state with long enough driving. This is most easily noticeable for $\Omega_{\text{drv}} = 0.4 \Omega_0$ where the instability is confined to a short interval. For $\Omega_{\text{drv}} = 0.5 \Omega_0, 0.6 \Omega_0$, we find $\min \text{eigs}_{\Delta} > 0$ at all times for all three drive strengths. The strong heating of electrons prohibits pairing even though in the absence of heating (dashed lines), pairing would have ensued.

The desirability of lower-frequency driving for enhancing the pairing instability can be understood by appealing to the different nature the two competing effects: parametric amplification of the retarded response on one hand and parametric phonon generation on the other hand. As we argued early on, the former is the main mechanism for enhancing T_c and the latter is the main suppressant. Heating of electrons and the decreased coherence of quasiparticles are both consequences of the interaction with the generated high-energy phonons.

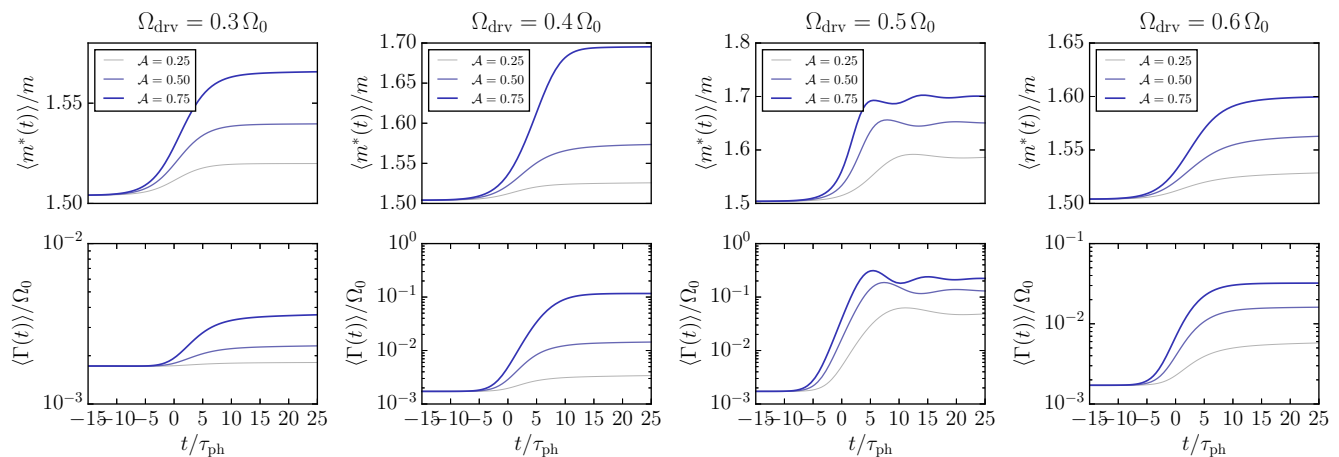


FIG. 15. Evolution of the electronic effective mass $\langle m^*(t) \rangle$ and scattering rate $\langle \Gamma(t) \rangle$ for different drive frequencies and amplitudes. The nonlinearity is cubic, the initial temperature is $T_i = 0.04 \Omega_0 \simeq 1.2 T_c$. The choice physical parameters are as given in Sec. VI.

Parametric generation of phonons is an on-shell process. For low-frequency driving, phonons may only be generated through accumulation of multiple energy quanta from the drive. These higher-order processes, however, become increasingly less probable. In contrast, (1) the retarded response does not need to satisfy an on-shell energetic condition, and (2) the cascade of low-frequency parametric resonances at $\Omega_0/(2n)$ extends the range of parametric amplification to very low frequencies. For a fixed driving strength and finite damping, the infinite cascade of parametric resonance “tongues” will be truncated at a certain lower frequency. This is exemplified in Fig. 4 in which only two resonances are present, or in Fig. 10 where only three lattice instability tongues are found. Nevertheless, the presence of even a few higher-order resonances enables the amplification of the retarded response for reasonably low-frequency drives.

To substantiate these arguments with numerical results, we have plotted the evolution of $\langle \Delta n_{\text{ph}}(t) \rangle$ and $\lambda(t)$ in Fig. 14, and electronic effective mass $\langle m^*(t) \rangle$ and damping $\langle \Gamma(t) \rangle$ in Fig. 15. As before, time averaging is performed during one drive period. We notice that for $\Omega_{\text{drv}} = 0.3 \Omega_0$, both $\langle \Delta n_{\text{ph}}(t) \rangle$ and $\langle \Gamma(t) \rangle$ remain nearly two orders of magnitude smaller than the on-resonance drive $\Omega_{\text{drv}} = 0.5 \Omega_0$. In contrast, $\langle m^*(t) \rangle$ and $\lambda(t)$ are at most a factor of 4 smaller. Thus, we indeed expect a negligible undesirable suppression while still benefiting from parametric amplification of $\lambda(t)$.

The energy distribution of the electrons at $t = 30 \tau_{\text{ph}}$ is shown in Fig. 16. It is noticed that the distribution barely changes from the initial thermal state for $\Omega_{\text{drv}} = 0.3 \Omega_0$, in agreement with the aforementioned arguments regarding suppressed parametric phonon generation below the resonance. In all cases, a decent Fermi-Dirac fit can be obtained. For an on-resonant driving frequency $\Omega_{\text{drv}} = 0.5 \Omega_0$, the effective temperature reaches $T_f^{\text{eff}} \approx 0.22 \Omega_{\text{drv}}$ (see the figure caption). Even in such cases, the energy density of electrons remains low enough, obviating performing a self-consistency feedback loop to phonons (see Fig. 7).

Finally, we note that the light-induced superconducting state is expected to persist beyond the predictions of the present

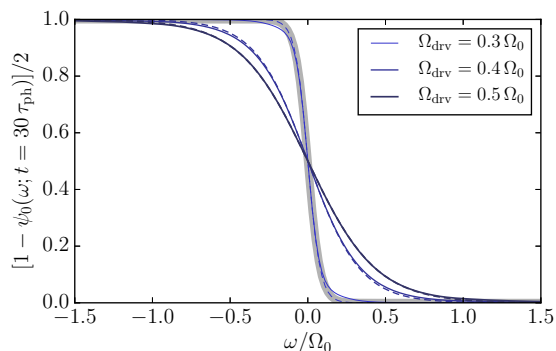


FIG. 16. The energy distribution of electrons after the drive is ramped up. The physical parameters are the same as Fig. 13. The dashed lines show the Fermi-Dirac fits. The thick gray line is the Fermi-Dirac distribution at the initial temperature $T_i = 0.04 \Omega_0$. The thin solid lines correspond to $\Omega_{\text{drv}}/\Omega_0 = 0.3, 0.4, 0.5$ with decreasing slope, respectively. The measurement time is $t = 30 \tau_{\text{ph}}$. The final effective temperatures are $T_f^{\text{eff}}/\Omega_0 \approx 0.04, 0.17, 0.22$ for $\Omega_{\text{drv}}/\Omega_0 = 0.3, 0.4, 0.5$, respectively.

analysis in the experiments. On the one hand, the formation of a superconducting gap leads to increased coherence of electrons and suppresses scatterings. On the other hand, the bulk electrons and phonons that remain unaffected by the pump pulse act as a low-temperature heat bath for the driven subsystem and keep it from excessive heating. Exploring these aspects of the problem is left for future works and is further discussed in Sec. VII.

C. Predictions for time-resolved angle-resolved photoemission spectroscopy experiments (tr-ARPES)

Up to this point, we have developed the theory of parametric amplification of electron-phonon coupling within a model that is general and material agnostic. Whether or not, and how, the mechanism is realized in a specific material depends on a number of factors such as the phonon spectra, strength of nonlinearities, and the selection rules that dictate and the presence or absence of the required nonlinear phonon couplings. These questions can be investigated either by performing *ab initio* calculation or through further experimental scrutiny. The interaction of electrons with periodically driven phonons will necessarily induce a certain degree of periodicity in electronic observables. This can be seen, for example, in Fig. 12 where the energy statistics develops Floquet components as the drive is ramped up. Here, we will show that the signal measured in tr-ARPES experiments will help reveal the formation of Floquet bands. The experimental observation of electronic Floquet bands provides strong evidence for the role of coherent driving in enhancing Cooper pairing.

The tr-ARPES signal can be theoretically calculated from the *lesser* electron Green’s function [55] as follows:

$$I(\mathbf{k}, \omega, t) \propto \text{Im} \frac{1}{2\pi \sigma_{\text{pr}}^2} \int dt_1 \int dt_2 \mathcal{G}_{\xi\mathbf{k}}^<(t, t') e^{-i(t_1 - t)^2/2\sigma_{\text{pr}}^2} \times e^{-(t_2 - t)^2/2\sigma_{\text{pr}}^2} e^{i\omega(t - t')}, \quad (94)$$

where σ_{pr} is the temporal resolution of the probe field which generically satisfies $\sigma_{\text{pr}} \gg \Omega_{\text{drv}}^{-1}$. The Gaussian window functions thus simply serve as picking up the “period-averaged” lesser Green’s function, which coincides with $n = 0$ Floquet component of \mathcal{G} . Thus,

$$I(\mathbf{k}, \omega, t) \propto \text{Im} \mathcal{G}_{\xi\mathbf{k}; n=0, m=0}^<(\omega; t). \quad (95)$$

Up to transitory effects, the lesser Green’s function can be calculated as $\mathcal{G}^< = \mathcal{G}^R \star \Sigma^< \star \mathcal{G}^A$ [26]. To leading order, we may approximate convolutions with zeroth-order FGM product formula. Each of the required ingredients for calculating $\mathcal{G}^<$ can be obtained using the results already available to us. As a first step, we solve the Dyson’s equation for $\mathcal{G}_{n;\xi}^R(\omega; t)$:

$$\begin{aligned} (\omega - m\Omega/2 - \xi) + \mathcal{G}_{\xi;n,m}^R(\omega; t) \\ = \delta_{n,0} + \sum_{n'} \Sigma_{n',n'-n+m}^R(\omega; t) \mathcal{G}_{\xi;n-n',n'+m}^R(\omega; t) + \mathcal{O}(\partial_t). \end{aligned} \quad (96)$$

Having calculated $\Sigma_{n,m}^R(\omega; t)$ previously from solving the Floquet-Boltzmann for electrons, $\mathcal{G}_{\xi;n,m}^R(\omega; t)$ is obtained by truncating the above equations in Floquet bands and solving it as a proper linear system. The advanced Green’s

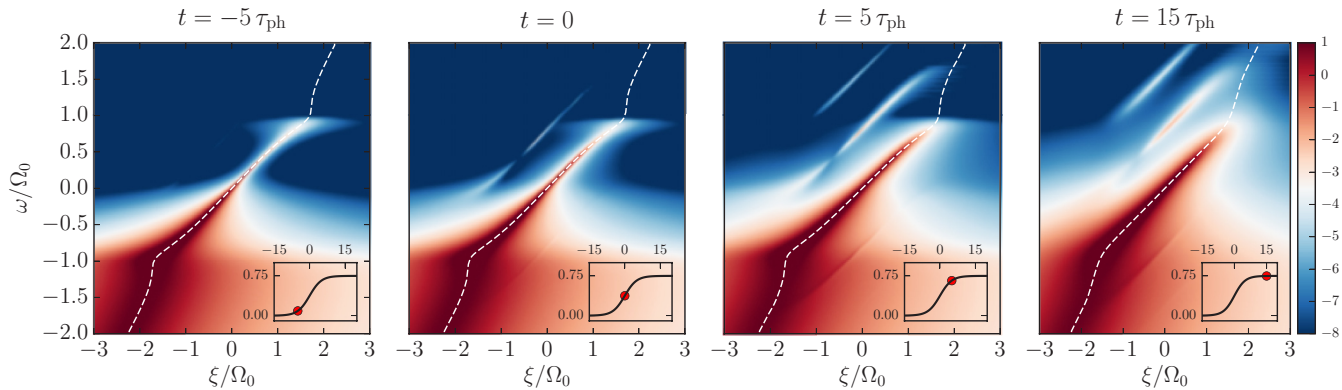


FIG. 17. Probing the formation of electronic Floquet bands via tr-ARPES experiments. The heat map plots show the intensity of the signal at different times in the logarithmic scale. The inset plots show the instantaneous amplitude of the drive during ramp-up. The white dashed lines indicate the dispersion of the main quasiparticle peak. The initial temperature is $T_i = 0.04 \Omega_0$, the drive parameters are chosen as $\Omega_{\text{drv}} = 0.4 \Omega_0$ and $\mathcal{A} = 0.75$. The nonlinearity is cubic, and the physical parameters are chosen as described in Sec. VI. Note the progressive formation of Floquet quasiparticle bands and the softening of the polaronic kink in the main quasiparticle dispersion as the system heats up. The time-averaged effective mass at the Fermi surface is inversely proportional to the slope of the main quasiparticle dispersion at $\xi = 0$ and is shown separately in Fig. 15 for better visibility.

function is found immediately using the identity $\mathcal{G}_{\xi;n,m}^A(\omega;t) = \mathcal{G}_{\xi;-n,m}^{R*}(\omega;t)$. By definition, the lesser electron self-energy $\Sigma^<$ is related to $\Sigma^{R/A/K}$ as $\Sigma^< = (\Sigma^K - \Sigma^R + \Sigma^A)/2$. Taking a FW transform, we find

$$\Sigma_{n,m}^<(\omega;t) = \frac{1}{2} [\Sigma_{n,m}^K(\omega;t) - \Sigma_{n,m}^R(\omega;t) + \Sigma_{-n,m}^{R*}(\omega;t)], \quad (97)$$

where we have used the identity $\Sigma_{n,m}^A(\omega;t) = \Sigma_{-n,m}^{R*}(\omega;t)$. With the knowledge of $\Sigma_{n,m}^<$, $\mathcal{G}_{\xi;n,m}^R$, and $\mathcal{G}_{\xi;n,m}^A$, $\mathcal{G}_{\xi;n=0,m=0}^<$ is calculated by employing the zeroth-order FGM formula twice. The final result is

$$\mathcal{G}_{\xi;0,0}^< = \sum_{n_R, n_L, n_A} \delta(n_R + n_L + n_A) \times \mathcal{G}_{\xi;n_R, -n_L - n_A}^R \Sigma_{n_L, -n_A + n_R}^< \mathcal{G}_{\xi;n_A, n_R + n_L}^A, \quad (98)$$

where we have dropped the common $(\omega;t)$ arguments for brevity. This procedure is formed for a range of ξ , and Eq. (95) is used to find the intensity of the tr-ARPES signal.

Figure 17 shows an example of the predicted tr-ARPES signal for $\Omega_{\text{drv}} = 0.4 \Omega_0$ and $\mathcal{A} = 0.75$ as a function of ω and ξ . We have traded the momentum transfer with $\xi \equiv \varepsilon_{\mathbf{k}} - \varepsilon_F$, the kinetic energy measures from the Fermi surface. The period-averaged quasiparticle dispersion E_{ξ} is obtained by locating the main coherent peak of the period-averaged retarded propagator by solving $\text{Re}[\mathcal{G}_{\xi;n=0}^R(E_{\xi};t)]^{-1} = 0$ and is shown as white dashed lines. Before the drive is ramped up, the signal matches what is expected from a coupled electron/optical phonon system at equilibrium [18]: filled states for $\omega < 0$, decreased quasiparticle coherence at $\omega = \pm \Omega_0$, and a larger effective mass for $|\omega| < \Omega_0$. The effective mass is obtained as $m/\langle m^*(t) \rangle = dE_{\xi}(\omega = 0)/d\xi|_{\xi=0}$ and is shown in the second column of Fig. 15 for the same drive parameters as Fig. 17.

An intriguing feature of Fig. 17 is the progressive formation of electronic Floquet bands as the drive is ramped up. The dynamical formation of Floquet bands in driven systems has been observed before experimentally in tr-ARPES spectroscopy of topological insulators [56]. The frequency spacing between

the emerging Floquet bands is set by $2\Omega_{\text{drv}}$. Therefore, the ARPES experiment along with the available spectroscopic measurements of the phonon spectra will inform about the origin of the persistent drive after the pump pulse is gone. We remark that the higher Floquet bands might be challenging to observe from noisy measurements due to the small weight of these extra features. For example, at $t = 15 \tau_{\text{ph}}$ and for the strong drive parameters used in Fig. 17, the intensity of the first Floquet band is nearly four orders of magnitude smaller than the main quasiparticle peak.

VII. CONCLUSIONS AND OUTLOOK

In this paper, we studied the parametric resonances of driven nonlinear lattices and discussed their role in enhancing the effective phonon-mediated electron-electron attraction. We presented the analysis in two stages. First, we gave a qualitative and intuitive account using perturbation theory, classical dynamics, and the Floquet BCS theory in Sec. III in order to elucidate the mechanism of parametric amplification of phonon-mediated Cooper pairing. Next, we developed a quantum kinetic formalism based on an extension of the Migdal-Eliashberg theory to driven systems and nonlinear lattices in Sec. IV C and revisited the problem one more time and in full detail in Sec. VI. The numerically tractable quantum kinetic formalism allowed us to study both the intricate transient and long-time dynamics of the system following the pump pulse. In particular, we investigated the role of parametric phonon generation and subsequent heating of electrons in destroying the transient superconducting instability. Finally, we predicted the transient formation of electronic Floquet bands as an experimentally observable consequence of parametrically driven phonons in Sec. VI C. This prediction can be tested in time-resolved ARPES experiments and can be used to establish coherent driving at work and better understand material-specific mechanisms of parametric drive generation.

This work can be extended in several directions. So far, we have studied the evolution of the system in the normal-

conducting state and treated Cooper pairing as an instability. An important extension of this work is to take into account dynamical symmetry breaking and the formation of the Floquet superconducting gap. This can be done most naturally by generalizing the Floquet-Boltzmann kinetic equation of electrons to symmetry-broken states and deriving a time-dependent Ginzburg-Landau theory for the slowly varying Floquet components of the gap $\{\Delta_n(\mathbf{x}, t)\}$. This extension allows us to address a broad range of largely unexplored theoretical questions, such as the scaling behavior of the coherently driven system in the critical regime, and the nature of Kibble-Zurek defects [57,58] formed as a result of nonadiabatic preparation of the ordered state. Furthermore, extension to gapped states allows us to calculate the nonequilibrium optical conductivity and make a more direct connection to pump-probe experiments [12]. A related problem is the question of the lifetime of the transient superconducting state. We find superconductivity as a transient phenomenon as shown in Fig. 13. It arises when electron-phonon interaction is already enhanced and before electrons have been heated too much. To give a more detailed analysis of the duration of the transient regime, we need to allow for opening of the quasiparticle gap which we expect to make transient superconductivity last longer.

The role of light-induced changes in the screened Coulomb interaction has been recently highlighted in the phenomenology of the light-induced superconductivity in K_3C_{60} in Refs. [12,32]. Furthermore, the shortcomings of Migdal-Eliashberg theory for providing an accurate description of fullerene superconductors and necessity of beyond-Migdal vertex corrections have been indicated in Ref. [59]. Therefore, it is desirable to extend the present formalism to include both Coulomb interaction and beyond-Migdal vertex corrections [15] and to study their role to the extent relevant to the mechanism discussed in this paper. In equilibrium, the effects of retarded Coulomb interaction can be incorporated in the Migdal-Eliashberg theory using the Morel-Anderson (MA) pseudopotential [41,60,61]. A nonequilibrium extension of this result is lacking and must be worked out. A naive application of the equilibrium result suggests that the MA pseudopotential $\mu^* = \mu_c/[1 + \mu_c \log(\epsilon_F/\omega_{ph})]$ directly decreases the mass enhancement factor, i.e., $\lambda(t) \rightarrow \lambda(t) - \mu^*$. Here, $\mu_c = v(0)U_c$ and U_c is the typical screened Coulomb interaction between conduction electrons. In this paper, we showed that parametric driving enhances Cooper pairing by increasing $\langle \lambda(t) \rangle$ and its temporal variations. Since the Coulomb interaction does not directly play a role in the parametric resonance of the lattice, we expect our conclusions to remain valid. Moreover, Ref. [32] suggests that μ_c effectively decreases in the pumped system, in which case the parametric amplification of $\lambda(t)$ and decreased μ^* both work toward enhancing Cooper pair formation in K_3C_{60} . The role of dynamical vertex corrections and the status of Migdal's theorem, in particular in the presence of the external drive, is less clear and must be carefully reassessed via real-time techniques in the spirit of the analysis provided for dynamical electron-mediated nonlinearities in Appendix E.

We note that photoinduced enhancement of superconductivity has also been observed in high- T_c cuprates [62] along with several theoretical proposals for explaining these experiments [20,63–67]. Cuprate superconductors are consid-

erably more complicated than conventional electron-phonon superconductors that we considered in this paper. Superconductivity in these materials is likely to be of nonphononic origin and there are several competing orders. However, we expect that the ideas explored here may be relevant for light-enhanced superconductivity in these materials as well. For example, periodic lattice modulation changes the strength of magnetic exchange interactions and may lead to parametrically amplified electron-paramagnon coupling. Paramagnons are expected to play the role of phonons in unconventional superconductors.

Last but not least, another intriguing future research direction which is also of much technological interest, is to extend the present analysis to open driven-dissipative systems along with accurate material-specific *ab initio* calculations. The transient light-induced superconducting state can be enhanced further or even stabilized by continuous pumping of the lattice and simultaneous cooling. Such a hybrid “pumped-and-cooled” device may operate more efficiently compared to the usual refrigerated superconductor depending on the highest achievable effective critical temperature and the pump absorption power of the material.

Note added in proof. Recently, the work by Murakami *et al.* appeared [68] that studies nonequilibrium superconductivity via Floquet DMFT approach in a related electron-phonon model which in addition includes coupling to electronic and phononic baths. The study mainly focuses on nonequilibrium steady states in the presence of continuous pumping and finds a net suppression or destruction of superconducting coherence. The paper also explores the initial dynamical instability of the normal state and the decay of superconducting fluctuations, although, an appreciable transient instability is not noticed. Given the significant differences between the two models and the explored parameter regimes, in particular, the high initial temperature $T = 3T_c$ and coupling to thermal baths that lead to significant suppression of pairing coherence, we believe the results of Murakami *et al.* are not in contradiction with ours. Further insights can be attained with a more systematic study of the parameter space of the models.

ACKNOWLEDGMENTS

We thank A. Cavalleri, A. Georges, V. Galitski, C. Kollath, A. Millis, B. Halperin, and D. Huse for useful discussions. M.B. and G.R. are grateful for support from the NSF through Grant No. DMR-1410435, the Institute of Quantum Information and Matter, an NSF Frontier center funded by the Gordon and Betty Moore Foundation, and the Packard Foundation. M.K. acknowledges support from the Technical University of Munich-Institute for Advanced Study, funded by the German Excellence Initiative and the European Union FP7 under Grant Agreement No. 291763, and from the DFG Grant No. KN 1254/1-1. I.M. acknowledges support from the Materials Sciences and Engineering Division, Basic Energy Sciences, Office of Science, US Department of Energy. E.D. acknowledges support from Packard Foundation, Harvard-MIT CUA, NSF (an NSF physics frontiers center) Grant No. DMR-1308435, AFOSR Quantum Simulation MURI, and AFOSR Photonic Quantum Matter MURI.

APPENDIX A: PARAMETRICALLY DRIVEN HARMONIC OSCILLATOR

We studied the problem of parametrically driven harmonic oscillator formally in Sec. III in the context of the resonant amplification of phonon response. Some of the technical details were left out and we present them here.

We presented the solution of the Heisenberg equation in terms of four special functions $\mathfrak{M}_{\alpha\beta}(t, t')$, $\alpha, \beta = P, Q$ [see Eq. (16)]. These functions can be expressed in terms of even and odd Mathieu functions and their derivatives as follows:

$$\begin{aligned}\mathfrak{M}_{QQ}(t, t') &= \frac{s(\Omega_{\text{drv}}t) c'(\Omega_{\text{drv}}t') - c(\Omega_{\text{drv}}t) s'(\Omega_{\text{drv}}t')}{s(\Omega_{\text{drv}}t') c'(\Omega_{\text{drv}}t') - c(\Omega_{\text{drv}}t') s'(\Omega_{\text{drv}}t')}, \\ \mathfrak{M}_{QP}(t, t') &= \frac{s(\Omega_{\text{drv}}t) c(\Omega_{\text{drv}}t') - c(\Omega_{\text{drv}}t) s(\Omega_{\text{drv}}t')}{s(\Omega_{\text{drv}}t') c'(\Omega_{\text{drv}}t') - c(\Omega_{\text{drv}}t') s'(\Omega_{\text{drv}}t')}, \\ \mathfrak{M}_{PQ}(t, t') &= \frac{s'(\Omega_{\text{drv}}t) c'(\Omega_{\text{drv}}t') - c'(\Omega_{\text{drv}}t) s'(\Omega_{\text{drv}}t')}{s(\Omega_{\text{drv}}t') c'(\Omega_{\text{drv}}t') - c(\Omega_{\text{drv}}t') s'(\Omega_{\text{drv}}t')}, \\ \mathfrak{M}_{PP}(t, t') &= \frac{s(\Omega_{\text{drv}}t) c'(\Omega_{\text{drv}}t') - s'(\Omega_{\text{drv}}t) c(\Omega_{\text{drv}}t')}{s(\Omega_{\text{drv}}t') c'(\Omega_{\text{drv}}t') - c(\Omega_{\text{drv}}t') s'(\Omega_{\text{drv}}t')},\end{aligned}\quad (\text{A1})$$

where $s(z) \equiv \text{Se}(\omega_{\mathbf{q}}^2/\Omega_{\text{drv}}^2, -\alpha\omega_{\mathbf{q}}^2/\Omega_{\text{drv}}^2, z)$ and $c(z) \equiv \text{Ce}(\omega_{\mathbf{q}}^2/\Omega_{\text{drv}}^2, -\alpha\omega_{\mathbf{q}}^2/\Omega_{\text{drv}}^2, z)$ denote the odd and even Mathieu functions with characteristic value $\omega_{\mathbf{q}}^2/\Omega_{\text{drv}}^2$ and parameter $-\alpha\omega_{\mathbf{q}}^2/\Omega_{\text{drv}}^2$, respectively, and the prime sign denotes derivatives with respect to z . We showed that $\mathfrak{M}_{QP}(t, t')$ is of particular interest and determines the retarded phonon response $\mathcal{D}_{\mathbf{Q}}^R(t, t')$ [see Eq. (17)]. Here, we present a series expansion of this function in terms of the parameter α [see Eq. (12)], i.e., $\mathfrak{M}_{QP}(t, t') = \sum_{n=0}^{\infty} a^n \mathfrak{M}_{QP}^{(n)}(t, t')$. The first two terms in the series are given as

$$\begin{aligned}\mathfrak{M}_{QP}^{(0)}(t, t') &= \frac{\Omega_{\text{drv}}}{\omega_{\mathbf{q}}} \sin[\omega_{\mathbf{q}}(t - t')], \\ \mathfrak{M}_{QP}^{(1)}(t, t') &= -\frac{\omega_{\mathbf{q}} \cos[\Omega_{\text{drv}}(t + t')]}{2(\omega_{\mathbf{q}}^2 - \Omega_{\text{drv}}^2)} \\ &\quad \times \{(\omega_{\mathbf{q}} + \Omega_{\text{drv}}) \sin[(\omega_{\mathbf{q}} - \Omega_{\text{drv}})(t - t')] \\ &\quad - (\omega_{\mathbf{q}} - \Omega_{\text{drv}}) \sin[(\omega_{\mathbf{q}} + \Omega_{\text{drv}})(t - t')]\}.\end{aligned}\quad (\text{A2})$$

The higher-order terms are increasingly more complex but can be easily worked out using a computer algebra system.

APPENDIX B: DEFINITION AND PROPERTIES OF THE CTP GREEN'S FUNCTIONS

In this Appendix, we briefly review the definition of CTP Green's functions, their various real-time components, and their symmetries. The CTP Nambu electron propagator is defined as

$$\hat{\mathcal{G}}_{\mathbf{k}}(t_1, t_2) = -i \langle T_{\mathcal{C}} [\Psi_{\mathbf{k}}(t_1) \Psi_{\mathbf{k}}^{\dagger}(t_2)] \rangle, \quad (\text{B1})$$

where $\Psi_{\mathbf{k}} = (c_{\mathbf{k}\uparrow}, c_{-\mathbf{k}\downarrow})^T$, $\Psi_{\mathbf{k}}^{\dagger} = (c_{\mathbf{k}\uparrow}^{\dagger}, c_{-\mathbf{k}\downarrow}^{\dagger})$, and $\hat{\mathcal{G}}_{\mathbf{k}}(t_1, t_2)$ is a 2×2 matrix in the Nambu space. Here, $\mathcal{C} = \mathcal{C}^+ \cup \mathcal{C}^-$ denotes the round-trip Keldysh contour where $\mathcal{C}^+ = [t_0, +\infty)$ and $\mathcal{C}^- = (+\infty, t_0]$, and $T_{\mathcal{C}}$ is the fermionic (antisymmetric) time-

ordering operator on \mathcal{C} . Similarly, the real phonon propagator is defined as

$$\mathcal{D}_{\mathbf{q}}(t_1, t_2) = -i \langle T_{\mathcal{C}} [\varphi_{\mathbf{q}}(t_1) \varphi_{-\mathbf{q}}(t_2)] \rangle, \quad (\text{B2})$$

where $\varphi_{\mathbf{q}} = b_{\mathbf{q}}^{\dagger} + b_{-\mathbf{q}}$ is the Fourier transform of the lattice displacement operator, and $T_{\mathcal{C}}$ is the bosonic (symmetric) time-ordering operator in \mathcal{C} . The *lesser* ($<$) and *greater* ($>$) real-time Green's functions are defined as specific orderings of the two contour times where $t_1 <_{\mathcal{C}} t_2$ and $t_1 >_{\mathcal{C}} t_2$, respectively:

$$\hat{\mathcal{G}}_{\mathbf{k}}^{<}(t_1, t_2) = +i \langle \Psi_{\mathbf{k}}^{\dagger}(t_2) \Psi_{\mathbf{k}}(t_1) \rangle, \quad (\text{B3a})$$

$$\hat{\mathcal{G}}_{\mathbf{k}}^{>}(t_1, t_2) = -i \langle \Psi_{\mathbf{k}}(t_1) \Psi_{\mathbf{k}}^{\dagger}(t_2) \rangle, \quad (\text{B3b})$$

$$\mathcal{D}_{\mathbf{q}}^{<}(t_1, t_2) = -i \langle \varphi_{-\mathbf{q}}(t_2) \varphi_{\mathbf{q}}(t_1) \rangle, \quad (\text{B3c})$$

$$\mathcal{D}_{\mathbf{q}}^{>}(t_1, t_2) = -i \langle \varphi_{\mathbf{q}}(t_1) \varphi_{-\mathbf{q}}(t_2) \rangle. \quad (\text{B3d})$$

The retarded (R), advanced (A), and Keldysh (K) propagators are defined as $\mathcal{A}^R(t_1, t_2) = \theta(t_1 - t_2)[\mathcal{A}^{>}(t_1, t_2) - \mathcal{A}^{<}(t_1, t_2)]$, $\mathcal{A}^A(t_1, t_2) = -\theta(t_2 - t_1)[\mathcal{A}^{>}(t_1, t_2) - \mathcal{A}^{<}(t_1, t_2)]$, and $\mathcal{A}^K(t_1, t_2) = \mathcal{A}^{>}(t_1, t_2) + \mathcal{A}^{<}(t_1, t_2)$, respectively, where \mathcal{A} is either $\hat{\mathcal{G}}$ or \mathcal{D} . We define spectral/statical decomposition of lesser/greater electron and phonon Green's functions as follows:

$$i\hat{\mathcal{G}}_{\mathbf{k}}^{\geq}(t_1, t_2) = \frac{1}{2} [i\hat{\mathcal{G}}_{\mathbf{k}}^K(t_1, t_2) \pm \hat{\mathbf{A}}_{\mathbf{k}}(t_1, t_2)], \quad (\text{B4a})$$

$$i\mathcal{D}_{\mathbf{q}}^{\geq}(t_1, t_2) = \frac{1}{2} [i\mathcal{D}_{\mathbf{q}}^K(t_1, t_2) \pm \rho_{\mathbf{q}}(t_1, t_2)]. \quad (\text{B4b})$$

These definitions can be thought of as definitions of electron and phonon spectral functions:

$$\hat{\mathbf{A}}_{\mathbf{k}}(t_1, t_2) \equiv i[\hat{\mathcal{G}}_{\mathbf{k}}^{>}(t_1, t_2) - \hat{\mathcal{G}}_{\mathbf{k}}^{<}(t_1, t_2)], \quad (\text{B5a})$$

$$\rho_{\mathbf{q}}(t_1, t_2) \equiv i[\mathcal{D}_{\mathbf{q}}^{>}(t_1, t_2) - \mathcal{D}_{\mathbf{q}}^{<}(t_1, t_2)]. \quad (\text{B5b})$$

Similar definitions apply to Green's functions in (Floquet-) Wigner representation, and for momentum-summed Green's functions. For all Nambu matrix quantities such as $\hat{\mathbf{A}}$, $i\hat{\mathcal{G}}^K$, etc., we define *capped* Nambu matrices as

$$\check{\mathbf{A}} \equiv \hat{\sigma}_z \hat{\mathbf{A}} \hat{\sigma}_z. \quad (\text{B6})$$

We finish this Appendix by listing a number of useful symmetry relations in the Wigner representation.

Lemma 1 (Symmetries of Nambu functions). We define time-reversal-symmetric (TRS) states as being invariant under operation $(\mathbf{k}, \uparrow) \leftrightarrow (-\mathbf{k}, \downarrow)$. The following identities hold for a TRS state:

$$\hat{\mathbf{A}}_{\mathbf{k}}(\omega, t)^{\dagger} = \hat{\mathbf{A}}_{\mathbf{k}}(\omega, t), \quad (\text{B7a})$$

$$\hat{\mathbf{A}}_{\mathbf{k}}(\omega, t) = i[\hat{\mathcal{G}}_{\mathbf{k}}^R(\omega, t) - \hat{\mathcal{G}}_{\mathbf{k}}^R(\omega, t)^{\dagger}], \quad (\text{B7b})$$

$$[i\hat{\mathcal{G}}_{\mathbf{k}}^K(\omega, t)]^{\dagger} = i\check{\mathcal{G}}_{\mathbf{k}}^K(\omega, t), \quad (\text{B7c})$$

$$\hat{\mathbf{A}}_{\mathbf{k}}(-\omega, t) = \hat{\sigma}_x \check{\mathbf{A}}_{\mathbf{k}}(\omega, t)^* \hat{\sigma}_x, \quad (\text{B7d})$$

$$i\hat{\mathcal{G}}_{\mathbf{k}}^K(-\omega, t) = -\hat{\sigma}_x [i\check{\mathcal{G}}_{\mathbf{k}}^K(\omega, t)]^* \hat{\sigma}_x. \quad (\text{B7e})$$

Proof. The proofs are elementary and readily follow from the definitions. The last two identities are less trivial and require a careful examination of the matrix elements of $\hat{\mathcal{G}}_{\mathbf{k}}(\omega, t)$. ■

Lemma 2 (Symmetries of Eliashberg functions). We define an inversion-symmetric (IS) state as being invariant under operation $\mathbf{q} \leftrightarrow -\mathbf{q}$. The following identities hold exactly for inversion symmetric states:

$$F_{\xi,\xi'}^\rho(v,t) = [F_{\xi,\xi'}^\rho(v,t)]^* = -F_{\xi,\xi'}^\rho(-v,t), \quad (\text{B8a})$$

$$iF_{\xi,\xi'}^K(v,t) = [iF_{\xi,\xi'}^K(v,t)]^* = iF_{\xi,\xi'}^K(-v,t). \quad (\text{B8b})$$

Proof. The proofs are elementary and follow from the definition of Eliashberg functions [Eqs. (48a) and (48b)] and phonon propagators. ■

Lemma 3 (Symmetries of the Nambu self-energy). The following identities hold for TRS and IS states:

$$\hat{\Sigma}^R(-\omega, T) = -\hat{\sigma}_x [\hat{\Sigma}^R(\omega, T)]^* \hat{\sigma}_x, \quad (\text{B9a})$$

$$i\hat{\Sigma}^K(-\omega, T) = -\hat{\sigma}_x [i\hat{\Sigma}^K(\omega, T)]^* \hat{\sigma}_x. \quad (\text{B9b})$$

Proof. Both identities are easily established by calculating $\hat{\Sigma}^{R/K}(-\omega, T)$ using Eqs. (52a) and (52b), changing integration variables $\omega', \nu \rightarrow -\omega', -\nu$ and using Lemmas 1 and 2 identities to change the sign of the frequencies that appear in the electron and phonon propagators. ■

APPENDIX C: PROOF OF \mathcal{G}^R MOMENTUM SUMMATION FORMULA

In this Appendix, we give a proof for \mathcal{G}^R momentum summation formula [Eq. (61)] using perturbation theory. One of the assumptions of the lemma is the independence of Σ^R from the momentum variable \mathbf{k} . As a result, \mathcal{G}^R depends on \mathbf{k} only via the electronic dispersion $\xi_{\mathbf{k}}$. Therefore, we may trade the momentum variable in \mathcal{G}^R with ξ without loss of generality. The Dyson series for \mathcal{G}^R is

$$\begin{aligned} \mathcal{G}_\xi^R &= \mathcal{G}_{0,\xi}^R + \mathcal{G}_{0,\xi}^R \star \Sigma^R \star \mathcal{G}_{0,\xi}^R \\ &+ \mathcal{G}_{0,\xi}^R \star \Sigma^R \star \mathcal{G}_{0,\xi}^R \star \Sigma^R \star \mathcal{G}_{0,\xi}^R + \dots, \end{aligned} \quad (\text{C1})$$

where

$$\mathcal{G}_{0,\xi}^R = \frac{1}{\omega - \xi - i0^+} \quad (\text{C2})$$

is the noninteracting retarded Green's function. Let us consider the second term in the series:

$$\begin{aligned} \mathcal{G}_{0,\xi}^R \star \Sigma^R \star \mathcal{G}_{0,\xi}^R &= \mathcal{G}_{0,\xi}^R \exp \left[\frac{i}{2} \bar{\partial}_t \bar{\partial}_\omega - \frac{i}{2} \bar{\partial}_t \bar{\partial}_\omega \right] \\ &\times \left(\Sigma^R \exp \left[\frac{i}{2} \bar{\partial}_t \bar{\partial}_\omega - \frac{i}{2} \bar{\partial}_t \bar{\partial}_\omega \right] \mathcal{G}_{\xi,0}^R \right). \end{aligned} \quad (\text{C3})$$

Since $\partial_t \mathcal{G}_{\xi,0}^R = 0$, if in addition we had $\partial_t \Sigma^R(\omega, t) = 0$, we would simply get $[\mathcal{G}_{0,\xi}^R]^2 \Sigma^R$. Expanding the differential operators in the exponents, it is easily noticed that every t derivative of Σ^R is accompanied either by $\partial_\omega \mathcal{G}_{0,\xi}^R = -[\mathcal{G}_{0,\xi}^R]^2$ or by $\mathcal{G}_{0,\xi}^R \partial_\omega \Sigma^R$. Therefore, derivative corrections due to t dependence of Σ^R are accompanied by *at least* one extra power of $\mathcal{G}_{0,\xi}^R$. Thus,

$$\mathcal{G}_{0,\xi}^R \star \Sigma^R \star \mathcal{G}_{0,\xi}^R = [\mathcal{G}_{0,\xi}^R]^2 \Sigma^R + [\mathcal{G}_{0,\xi}^R]^3 \times \mathcal{O}(\partial_t \Sigma^R) + \dots \quad (\text{C4})$$

This result is easily generalized to the n th term in the Dyson series:

$$\begin{aligned} \mathcal{G}_{0,\xi}^R \star \Sigma^R \star \mathcal{G}_{0,\xi}^R \star \dots \star \mathcal{G}_{0,\xi}^R \\ = [\mathcal{G}_{0,\xi}^R]^n [\Sigma^R]^{n-1} + [\mathcal{G}_{0,\xi}^R]^{n+1} \times \mathcal{O}(\partial_t \Sigma^R) + \dots \end{aligned} \quad (\text{C5})$$

With this observation, let us integrate the sides of Eq. (C1) over ξ , considering only the first n terms in the series. The integral over the first term is trivial:

$$\int_{-\infty}^{+\infty} d\xi \mathcal{G}_{0,\xi}^R = \int_{-\infty}^{+\infty} \frac{d\xi}{\xi - \omega + i0^+} = -i\pi. \quad (\text{C6})$$

Using Eq. (C4), it is easily shown that the integral over the second term vanishes:

$$\begin{aligned} \int_{-\infty}^{+\infty} d\xi \mathcal{G}_{0,\xi}^R \star \Sigma^R \star \mathcal{G}_{0,\xi}^R \\ = \Sigma^R \int_{-\infty}^{+\infty} \frac{d\xi}{(\omega - \xi + i0^+)^2} \\ + \mathcal{O}(\partial_t \Sigma^R) \int_{-\infty}^{+\infty} \frac{d\xi}{(\omega - \xi + i0^+)^3} + [\dots] = 0. \end{aligned} \quad (\text{C7})$$

This result is due to the fact that every term in the expansion of the Groenewold-Moyal series has at least a second-order pole. The same result holds for all higher-order terms in the Dyson series. Assuming that the order of limit and integrations can be interchanged, and that the Dyson series converges, we find that the only nontrivial contribution stems from the noninteracting Green's function. This proves the sought after result

$$\int_{-\infty}^{+\infty} d\xi \mathcal{G}_\xi^R = \int_{-\infty}^{+\infty} d\xi \mathcal{G}_{0,\xi}^R = -i\pi. \quad (\text{C8})$$

APPENDIX D: CALCULATING PHONON EXCITATION DENSITY AND PHONON SQUEEZING FROM $i\mathcal{D}^K$

We formulated the problem in Sec. IV in terms of the real phonon propagator $\mathcal{D}_{\mathbf{q}}(t_1, t_2) \equiv -i\langle T_C[\varphi_{\mathbf{q}}(t_1)\varphi_{-\mathbf{q}}(t_2)] \rangle$. While this formulation is convenient and compact, it does not immediately yield useful physical observables for such a phonon number $n_{\mathbf{q}}(t) \equiv \langle b_{\mathbf{q}}^\dagger(t)b_{\mathbf{q}}(t) \rangle$ or the anomalous correlations $\kappa_{\mathbf{q}}(t) \equiv \text{Re}[\langle b_{\mathbf{q}}(t)b_{-\mathbf{q}}(t) \rangle]$. Here, we show that both quantities can be readily calculated from the Keldysh phonon correlator in the Wigner representation $\mathcal{D}_{\mathbf{q}}^K(\omega, t)$ by performing appropriate frequency integrations. This is enabled by the observation that the interaction and drive terms in the Hamiltonian both commute with $\hat{\varphi}_{\mathbf{q}}$. The only noncommuting term is the lattice kinetic energy. Thus, the Heisenberg equation for $\hat{\varphi}_{\mathbf{q}}$ takes the following simple form:

$$\partial_t \hat{\varphi}_{\mathbf{q}}(t) = 2\omega_{\mathbf{q}} \hat{\pi}_{\mathbf{q}}(t). \quad (\text{D1})$$

We assume the $\mathbf{q} \leftrightarrow -\mathbf{q}$ symmetry in this section and set $\hbar = 1$. The last equation allows us to obtain $\pi\pi$ correlators by calculating appropriate time derivatives of \mathcal{D}^K . Defining $\mathcal{P}_{\mathbf{q}}(t_1, t_2) \equiv -i\langle T_C[\pi_{\mathbf{q}}(t_1)\pi_{-\mathbf{q}}(t_2)] \rangle$, Eq. (D1) immediately implies

$$\mathcal{P}_{\mathbf{q}}(t_1, t_2) = \frac{1}{4\omega_{\mathbf{q}}^2} \partial_{t_1} \partial_{t_2} \mathcal{D}_{\mathbf{q}}(t_1, t_2). \quad (\text{D2})$$

At equal times, the Keldysh $\varphi\varphi$ and $\pi\pi$ correlators evaluate to a combination of our sought after observables $n_{\mathbf{q}}$ and $\kappa_{\mathbf{q}}$:

$$(i/2)\mathcal{D}_{\mathbf{q}}^K(t,t) \equiv 1 + 2n_{\mathbf{q}}(t) + 2\kappa_{\mathbf{q}}(t), \quad (\text{D3a})$$

$$(2i)\mathcal{P}_{\mathbf{q}}^K(t,t) \equiv 1 + 2n_{\mathbf{q}}(t) - 2\kappa_{\mathbf{q}}(t), \quad (\text{D3b})$$

which together with Eq. (D2) yields

$$n_{\mathbf{q}}(t) = \frac{1}{4} i\mathcal{D}_{\mathbf{q}}^K(t,t) + \frac{1}{4} \partial_{t_1} \partial_{t_2} i\mathcal{D}_{\mathbf{q}}^K(t_1,t_2)|_{t_1=t_2=t} - \frac{1}{2}, \quad (\text{D4a})$$

$$\kappa_{\mathbf{q}}(t) = \frac{1}{4} i\mathcal{D}_{\mathbf{q}}^K(t,t) - \frac{1}{4} \partial_{t_1} \partial_{t_2} i\mathcal{D}_{\mathbf{q}}^K(t_1,t_2)|_{t_1=t_2=t}. \quad (\text{D4b})$$

In the Wigner representation, $\partial_{t_1} \partial_{t_2} \rightarrow v^2$ and we find

$$n_{\mathbf{q}}(t) = \frac{1}{4} \int_{-\infty}^{+\infty} \frac{dv}{2\pi} \left(1 + \frac{v^2}{\omega_{\mathbf{q}}^2} \right) i\mathcal{D}_{\mathbf{q}}^K(v,t) - \frac{1}{2}, \quad (\text{D5a})$$

$$\kappa_{\mathbf{q}}(t) = \frac{1}{4} \int_{-\infty}^{+\infty} \frac{dv}{2\pi} \left(1 - \frac{v^2}{\omega_{\mathbf{q}}^2} \right) i\mathcal{D}_{\mathbf{q}}^K(v,t). \quad (\text{D5b})$$

The anomalous phonon density can be related to phonon squeezing with additional considerations. First, we observe $\text{Im}[\langle b_{\mathbf{q}}(t)b_{-\mathbf{q}}(t) \rangle] = 0$ in our problem since nonlinearities produce modulation of $\varphi_{\mathbf{q}}\varphi_{-\mathbf{q}}$ (as opposed to $\pi_{\mathbf{q}}\pi_{-\mathbf{q}}$; see Sec. III). Assuming that a low-temperature state is maintained at all times and weak electron-phonon coupling, the phonon state can be approximated as product of two-mode squeezed states of $\pm\mathbf{q}$ on the top of a coherent state for $\mathbf{q} = 0$, i.e., $|\Phi(t)\rangle \sim \{[\prod_{\mathbf{q}} \exp[\xi_{\mathbf{q}}(t)(b_{\mathbf{q}}^\dagger b_{-\mathbf{q}}^\dagger - b_{-\mathbf{q}} b_{\mathbf{q}})]\} \exp[\sqrt{N}\varphi_0(t)(b_0^\dagger - b_0)/2] |0\rangle$ throughout the evolution. Here, $\xi_{\mathbf{q}}(t)$ is the momentum-squeezing strength and $\varphi_0(t)$ is the coherent displacement. For $\mathbf{q} \neq 0$, this ansatz provides the following relation between the squeezing parameter $\xi_{\mathbf{q}}(t)$ and the anomalous phonon density:

$$\kappa_{\mathbf{q}}(t) = \frac{1}{2} \sinh[2\xi_{\mathbf{q}}(t)]. \quad (\text{D6})$$

For weak nonlinearities, the squeezing is also weak $|\xi_{\mathbf{q}}(t)| \ll 1$ and we find $\xi_{\mathbf{q}}(t) = \kappa_{\mathbf{q}}(t) + \mathcal{O}(\kappa_{\mathbf{q}}^3)$. Thus, the anomalous phonon density directly yields the squeezing parameter. We have shown the period averaged $\langle \cosh[\xi_{\mathbf{q}}(t)] \rangle - 1 \approx 2\langle \kappa_{\mathbf{q}}^2(t) \rangle$ in Fig. 9(d). It is noticed that squeezing significantly increases as the drive is ramped up, consistent with the physics of the parametrically driven harmonic oscillator.

APPENDIX E: ELECTRON-MEDIATED PHONON DISSIPATION AND NONLINEARITIES

The evolution equation for phonon propagators was derived in Sec. IV A as well as their counterparts in the Floquet-Boltzmann kinetic approximation in Sec. IV D. So long as the evolution of phonons is concerned, electrons play the role of a *quantum bath* through memory convolution integrals $\Pi_{\mathbf{q}} \star \mathcal{D}_{\mathbf{q}}$ and $\mathcal{D}_{\mathbf{q}} \star \Pi_{\mathbf{q}}$ appearing in Eqs. (31a) and (31b), respectively.

In this Appendix, we derive approximate expressions for $\Pi_{\mathbf{q}}$ assuming that the electrons remain in the initial low-temperature degenerate regime. Meanwhile, we also study the contribution of electrons to phonon nonlinearities. Both objectives can be achieved by integrating out the electrons from the Lagrangian $\mathcal{L}[\varphi, \Psi]$ and obtaining a phonon-only effective

action $S_{\text{eff}}[\varphi]$. Expanding the effective action in the electron-phonon coupling, we obtain the bath term at the second order. Higher-order terms give the electronic contribution to lattice nonlinearities. Since these corrections have a strong dynamical nature, it is conceivable that they could become large when certain resonance conditions are met; indeed, we find this to be case. In other words, even though the *intrinsic* lattice nonlinearities might be small, coupling to conduction electrons effectively produces large nonlinearities in the presence of a near-resonant drive.

We start our discussion with the electron-phonon Lagrangian

$$\mathcal{L}[\varphi, \Psi] = \mathcal{L}_0[\varphi] + \sum_{\mathbf{k}} \Psi_{\mathbf{k}}^\dagger (i\partial_t \mathbb{I} - \xi_{\mathbf{k}} \hat{\sigma}_3) \Psi_{\mathbf{k}} - \frac{1}{\sqrt{N}} \sum_{\mathbf{k}, \mathbf{k}'} g_{\mathbf{k}, \mathbf{k}'} \varphi_{\mathbf{k}-\mathbf{k}'} \Psi_{\mathbf{k}'}^\dagger \hat{\sigma}_3 \Psi_{\mathbf{k}}, \quad (\text{E1})$$

where $\mathcal{L}_0[\varphi] = -\sum_{\mathbf{q}} (2\omega_{\mathbf{q}})^{-1} \varphi_{\mathbf{q}} (\partial_t^2 + \omega_{\mathbf{q}}^2) \varphi_{-\mathbf{q}}/2 + (\Lambda/2) |F(t)|^2 \sqrt{N} \varphi_{\mathbf{q}=0}$ is the quadratic part, including the external drive. It is most convenient to perform the calculations in the real-time formalism in order to avoid tedious analytical continuation procedure required in the Matsubara formalism. Integrating out the electrons, we find

$$S_{\text{eff}}[\varphi] = \int_{\mathcal{C}} dt \mathcal{L}_0[\varphi] - i \text{Tr} \ln \left[\hat{\mathcal{G}}_{0, \mathbf{k}}^{-1}(t, t') \delta_{\mathbf{k}, \mathbf{k}'} - \frac{1}{\sqrt{N}} g_{\mathbf{k}, \mathbf{k}'} \hat{\sigma}_3 \varphi_{\mathbf{k}-\mathbf{k}'}(t) \delta_{\mathcal{C}}(t, t') \right]. \quad (\text{E2})$$

Here, $\hat{\mathcal{G}}_{0, \mathbf{k}}^{-1}(t, t') = (i\partial_t - \xi_{\mathbf{k}} \hat{\sigma}_3) \delta_{\mathcal{C}}(t, t')$ and the trace implies momentum summation, contour time integration, and Nambu space summation. Expanding the second term in powers of g , we find

$$S_{\text{eff}}[\varphi] = S_0[\varphi] + \sum_{n=1}^{\infty} S_n[\varphi],$$

$$S_n[\varphi] = \frac{i}{nN^{n/2}} \sum_{\mathbf{k}_i} \int_{\mathcal{C}} dt_1 \dots dt_n \text{Tr} [\hat{\mathcal{G}}_{0, \mathbf{k}_1}^{-1}(t_1, t_2) \hat{\sigma}_z \times \hat{\mathcal{G}}_{0, \mathbf{k}_2}^{-1}(t_2, t_3) \hat{\sigma}_z \dots \hat{\mathcal{G}}_{0, \mathbf{k}_n}^{-1}(t_n, t_1) \hat{\sigma}_z] \times g_{\mathbf{k}_1, \mathbf{k}_2} g_{\mathbf{k}_2, \mathbf{k}_3} \dots g_{\mathbf{k}_n, \mathbf{k}_1} \times \varphi_{\mathbf{k}_1 - \mathbf{k}_2}(t_2) \varphi_{\mathbf{k}_2 - \mathbf{k}_3}(t_3) \dots \varphi_{\mathbf{k}_n - \mathbf{k}_1}(t_1). \quad (\text{E3})$$

The first-order correction $S_1[\varphi]$ vanishes for Holstein-type screened electron-phonon couplings [see the discussion after Eq. (35)]. The sum of higher-order vertices can be diagrammatically represented as

$$\sum_{n=2}^{\infty} S_n[\varphi] = \text{diagram 1} + \text{diagram 2} + \text{diagram 3} + \dots \quad (\text{E4})$$

It is convenient to make the forward/backward contour time indices explicit and perform a Keldysh rotation of φ^\pm fields into symmetric (“classical”) and antisymmetric (“quantum”)

components $\bar{\varphi}^\alpha = U_{\alpha\beta} \varphi_\beta$:

$$\begin{pmatrix} \bar{\varphi}^c \\ \bar{\varphi}^q \end{pmatrix} = \frac{1}{\sqrt{2}} \begin{pmatrix} 1 & 1 \\ 1 & -1 \end{pmatrix} \begin{pmatrix} \varphi^+ \\ \varphi^- \end{pmatrix}. \quad (\text{E5})$$

The bare action in Keldysh representation reads as

$$S_0[\varphi] = -\frac{1}{2} \sum_{\mathbf{q}} \frac{1}{2\omega_{\mathbf{q}}} \int_{-\infty}^{\infty} dt [\bar{\varphi}_{\mathbf{q}}^c (\partial_t^2 + \omega_{\mathbf{q}}^2) \bar{\varphi}_{-\mathbf{q}}^q + \bar{\varphi}_{\mathbf{q}}^q (\partial_t^2 + \omega_{\mathbf{q}}^2) \bar{\varphi}_{-\mathbf{q}}^c] + \frac{\Lambda}{2} \int_{-\infty}^{\infty} dt |F(t)|^2 \sqrt{2N} \bar{\varphi}_{\mathbf{q}=0}^q(t). \quad (\text{E6})$$

Likewise, the higher-order terms in the Keldysh representation read as

$$S_n[\varphi] = \frac{1}{n! N^{n/2-1}} \sum_{\mathbf{q}_i} \int_{-\infty}^{\infty} dt_1 \dots dt_n V_{\mathbf{q}_1 \dots \mathbf{q}_n}^{\alpha_1 \dots \alpha_n}(t_1, \dots, t_n) \bar{\varphi}_{\mathbf{q}_1}^{\alpha_1}(t_1) \dots \bar{\varphi}_{\mathbf{q}_n}^{\alpha_n}(t_n) \delta\left(\sum_i \mathbf{q}_i\right), \quad (\text{E7})$$

where

$$V_{\mathbf{q}_1 \dots \mathbf{q}_n}^{\alpha_1 \dots \alpha_n}(t_1, \dots, t_n) = \frac{i(n-1)!}{N} \sum_{\mathbf{k}} \text{Tr}[\bar{\mathcal{G}}_{0, \mathbf{k}+\mathbf{q}_1}^{\mu_1 \nu_2}(t_1, t_2) \hat{\sigma}_z \bar{\mathcal{G}}_{0, \mathbf{k}+\mathbf{q}_1+\mathbf{q}_2}^{\mu_2 \nu_3}(t_2, t_3) \hat{\sigma}_z \dots \bar{\mathcal{G}}_{0, \mathbf{k}}^{\mu_n \nu_1}(t_n, t_1) \hat{\sigma}_z] \\ \times g_{\mathbf{k}, \mathbf{k}+\mathbf{q}_1} g_{\mathbf{k}+\mathbf{q}_1, \mathbf{k}+\mathbf{q}_1+\mathbf{q}_2} \dots g_{\mathbf{k}+\mathbf{q}_1+\dots+\mathbf{q}_{n-1}, \mathbf{k}} \Gamma_{\alpha_1 \mu_1 \nu_1} \dots \Gamma_{\alpha_n \mu_n \nu_n}, \quad (\text{E8})$$

and $\Gamma_{\alpha\mu\nu} = \sum_{\beta} U_{\alpha\beta} U_{\mu\beta} U_{\nu\beta} \sigma_{\beta\beta}^z$ is a vertex in the Keldysh space. Finally, $\bar{\mathcal{G}}_0$ is the bare propagator in the Keldysh space:

$$\bar{\mathcal{G}} = \begin{pmatrix} \hat{\mathcal{G}}^K & \hat{\mathcal{G}}^R \\ \hat{\mathcal{G}}^A & 0 \end{pmatrix}. \quad (\text{E9})$$

Note that each matrix element additionally carries a 2×2 Nambu structure. We restrict our analysis to the normal state hereafter, in which case the Nambu structure is immaterial. The Nambu space traces reduce to a multiplicative factor of 2 (= total spin degeneracy) for each electron loop. In the following sections, we briefly study the first few vertices in succession.

1. Second-order correction: Landau damping

A direct calculation using Eq. (E8) gives the matrix elements of $\Pi_{\mathbf{q}}^{\alpha_1 \alpha_2}(t_1, t_2) \equiv -V_{\mathbf{q}, -\mathbf{q}}^{\alpha_1 \alpha_2}(t_1, t_2)$:

$$\Pi_{\mathbf{q}, -\mathbf{q}}^{\alpha_1 \alpha_2}(t_1, t_2) = \begin{pmatrix} 0 & \Pi_{\mathbf{q}}^A(t_1, t_2) \\ \Pi_{\mathbf{q}}^R(t_1, t_2) & \Pi_{\mathbf{q}}^K(t_1, t_2) \end{pmatrix}, \quad (\text{E10})$$

where

$$\Pi_{\mathbf{q}}^A(t_1, t_2) = -\frac{i}{N} \sum_{\mathbf{k}} |g_{\mathbf{k}, \mathbf{k}+\mathbf{q}}|^2 [\mathcal{G}_{0, \mathbf{k}+\mathbf{q}}^A(t_1, t_2) \mathcal{G}_{0, \mathbf{k}}^K(t_2, t_1) + \mathcal{G}_{0, \mathbf{k}+\mathbf{q}}^K(t_1, t_2) \mathcal{G}_{0, \mathbf{k}}^R(t_2, t_1)], \\ \Pi_{\mathbf{q}}^R(t_1, t_2) = -\frac{i}{N} \sum_{\mathbf{k}} |g_{\mathbf{k}, \mathbf{k}+\mathbf{q}}|^2 [\mathcal{G}_{0, \mathbf{k}+\mathbf{q}}^K(t_1, t_2) \mathcal{G}_{0, \mathbf{k}}^A(t_2, t_1) + \mathcal{G}_{0, \mathbf{k}+\mathbf{q}}^R(t_1, t_2) \mathcal{G}_{0, \mathbf{k}}^K(t_2, t_1)], \\ \Pi_{\mathbf{q}}^K(t_1, t_2) = -\frac{i}{N} \sum_{\mathbf{k}} |g_{\mathbf{k}, \mathbf{k}+\mathbf{q}}|^2 [\mathcal{G}_{0, \mathbf{k}+\mathbf{q}}^R(t_1, t_2) \mathcal{G}_{0, \mathbf{k}}^A(t_2, t_1) + \mathcal{G}_{0, \mathbf{k}+\mathbf{q}}^A(t_1, t_2) \mathcal{G}_{0, \mathbf{k}}^R(t_2, t_1) + \mathcal{G}_{0, \mathbf{k}+\mathbf{q}}^K(t_1, t_2) \mathcal{G}_{0, \mathbf{k}}^K(t_2, t_1)]. \quad (\text{E11})$$

The bare propagators in equilibrium are functions of $t_1 - t_2$ and admit the following standard Fourier representation:

$$\mathcal{G}_{\mathbf{k}}^{R/A}(\omega) = \frac{1}{\omega - \xi_{\mathbf{k}} \pm i0^+}, \quad \mathcal{G}_{\mathbf{k}}^K(\omega) = -2\pi i \delta(\omega - \xi_{\mathbf{k}}) [1 - 2n_F(\xi_{\mathbf{k}})]. \quad (\text{E12})$$

Calculating $\Pi_{\mathbf{q}}^{R/A/K}$ in equilibrium is standard and yields the well-known Lindhard function [43]

$$\Pi_{\mathbf{q}}^{R/A}(\omega) = \frac{2}{N} \sum_{\mathbf{k}} |g_{\mathbf{k}, \mathbf{k}+\mathbf{q}}|^2 \frac{n_F(\xi_{\mathbf{k}}) - n_F(\xi_{\mathbf{k}+\mathbf{q}})}{\omega - \xi_{\mathbf{k}+\mathbf{q}} + \xi_{\mathbf{k}} \pm i0^+}, \quad (\text{E13a})$$

$$i\Pi_{\mathbf{q}}^K(\omega) = -2\text{Im}[\Pi_{\mathbf{q}}^R(\omega)] \coth(\beta\omega/2). \quad (\text{E13b})$$

Combining $S_2[\varphi]$ with the bare action $S_0[\varphi]$ yields the full quadratic part of the effective phonon-only action $S_{\text{quad}}[\varphi]$:

$$S_{\text{quad}}[\varphi] = -\frac{1}{2} \sum_{\mathbf{q}} \frac{1}{2\omega_{\mathbf{q}}} \int_{-\infty}^{\infty} dt_1 dt_2 \bar{\varphi}_{\mathbf{q}}^{\alpha_1}(t_1) [(\partial_{t_1}^2 + \omega_{\mathbf{q}}^2) \hat{\sigma}_x^{\alpha_1 \alpha_2} \delta(t_1 - t_2) + 2\omega_{\mathbf{q}} \Pi^{\alpha_1 \beta_1}(t_1, t_2)] \bar{\varphi}_{-\mathbf{q}}^{\alpha_2}(t_2) + (\Lambda/2) \\ \times \int_{-\infty}^{\infty} dt |F(t)|^2 \sqrt{2N} \bar{\varphi}_{\mathbf{q}=0}^q(t). \quad (\text{E14})$$

The quantity $\Gamma_{\mathbf{q}}^{(\text{ph})}(\omega) \equiv -2 \text{Im}[\Pi_{\mathbf{q}}^R(\omega)]$ is of particular interest and represents the spectrum of the dissipative bath the electronic degrees of freedom provide for phonons. We observe that $\Gamma_{\mathbf{q}=0}(\omega) = 0$ for finite ω , which is an expected consequence of momentum conservation. Thus, the uniform lattice displacement $\langle \bar{\varphi}^c(t) \rangle$ experiences no friction from electrons. Employing the simplifications introduced in Sec. IV B, i.e., flat EDOS, local approximation for Π , and (\mathbf{k}, \mathbf{q}) -independent el-ph coupling, we can calculate the local bath spectrum $\Gamma_{\ell}^{(\text{ph})}$ analytically at $T = 0$:

$$\begin{aligned} \Gamma_{\ell}^{(\text{ph})}(\omega; T = 0) &\equiv \frac{1}{N} \sum_{\mathbf{q}} \Gamma_{\mathbf{q}}(\omega; T = 0) \\ &\approx 4\pi |g|^2 \int_{-\omega}^0 d\xi v(\xi) v(\xi + \omega) \\ &\approx (4\pi |g|^2 v(0)^2) \omega. \end{aligned} \quad (\text{E15})$$

Given that the energy density of electrons is much lower than Einstein phonon energy scale in the present context, it is an excellent approximation to use the last equation even for nonequilibrium electronic states. The last result is akin to the well-known Allen's formula [69] which is often used to infer electron-phonon coupling from the phonon linewidth broadening. Finally, one can calculate $\text{Re} \Pi^{(\ell)}(\omega; T = 0)$ within the same approximations to find

$$\begin{aligned} \text{Re} \Pi_{\ell}^R(\omega) &\approx 2|g|^2 v(0)^2 \int_0^{W_{\text{el}}/2} \int_0^{W_{\text{el}}/2} \frac{(\xi_1 + \xi_2) d\xi_1 d\xi_2}{(\omega + i0^+)^2 - (\xi_1 + \xi_2)^2}. \end{aligned} \quad (\text{E16})$$

In the Migdal limit, $\omega \ll W_{\text{el}}$ for all ω of interest. To leading order in ω/W_{el} , we find $\text{Re} \Pi_{\ell}^R(\omega) \approx -4|g|^2 v(0)^2 \ln(2) W_{\text{el}}$ which corresponds to a constant Lamb shift.

In summary, within the validity limits of the simplified model of Sec. IV B, the dissipative effect of electrons on the dynamics of optical phonons can be modeled as a local

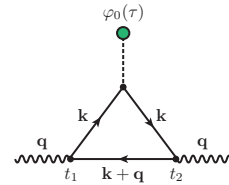
quantum Ohmic bath:

$$\begin{aligned} \Pi_{\ell}^R(\omega) &\simeq \omega_L - i\gamma_{\ell}\omega/2, \\ \Pi_{\ell}^K(\omega) &\simeq \gamma_{\ell}\omega \coth(\beta\omega/2), \end{aligned} \quad (\text{E17})$$

where $\omega_L \approx -4|g|^2 v(0)^2 \ln(2) W$ is the Lamb shift and $\gamma_{\ell} = 2\pi \omega_0 v(0) \lambda$ is the dimensionless friction constant expressed in terms of the mass enhancement factor λ [see Eq. (55)]. Furthermore, the above expressions remain valid as long as the electrons approximately remain in a quantum degenerate state.

2. Third-order correction: Electron-mediated cubic nonlinearity

The cubic vertex $V_{\mathbf{q}_1, \mathbf{q}_2, \mathbf{q}_3}^{\alpha_1, \alpha_2, \alpha_3}$ has a complicated spatial and temporal structure due the nonlocality of electrons. Here, we rather focus on calculating the retarded phonon self-energy correction that arises from this cubic vertex rather than a general analysis. Recalling that the lattice has a large coherent uniform displacement in our problem, we find that the leading self-energy correction is obtained by contracting one of the legs (the third leg without the loss of generality) with the classical displacement φ_0 . The resulting self-energy correction $\Pi_{\Delta, \mathbf{q}}(t_1, t_2)$ has the following diagrammatic representation:



Integration over τ , the time argument of $\varphi_0(\tau)$, is implied. Contracting the third leg with φ_0 sets α_3 to 1, i.e., to the “classical” Keldysh index. The retarded phonon self-energy is obtained by further choosing $\alpha_1 = 2$ and $\alpha_2 = 1$ [e.g., see Eq. (E10)]. Performing the intermediate Keldysh space traces in Eq. (E8), we find

$$\begin{aligned} V_{\mathbf{q}, -\mathbf{q}, 0}^{2,1,1}(t_1, t_2, \tau) &= \frac{i\sqrt{2}}{N} \sum_{\mathbf{k}} |g_{\mathbf{k}, \mathbf{k}+\mathbf{q}}|^2 g_{\mathbf{k}, \mathbf{k}} [\mathcal{G}_{\mathbf{k}+\mathbf{q}}^K(t_1, t_2) \mathcal{G}_{\mathbf{k}}^A(t_2, \tau) \mathcal{G}_{\mathbf{k}}^A(\tau, t_1) + \mathcal{G}_{\mathbf{k}+\mathbf{q}}^R(t_1, t_2) \mathcal{G}_{\mathbf{k}}^K(t_2, \tau) \mathcal{G}_{\mathbf{k}}^A(\tau, t_1) \\ &\quad + \mathcal{G}_{\mathbf{k}+\mathbf{q}}^R(t_1, t_2) \mathcal{G}_{\mathbf{k}}^R(t_2, \tau) \mathcal{G}_{\mathbf{k}}^K(\tau, t_1)]. \end{aligned} \quad (\text{E18})$$

Notice that the electron lines, starting from the $\mathbf{k} + \mathbf{q}$ line and traversing counterclockwise, assume the following Keldysh space labels: $KA A, RKA, R R K$. It can be shown that the same structure applies to higher-order single-electron-loop vertices: with N fermion propagators in a loop and $N - 2$ classical field contractions, the retarded self-energy comprises N terms, and the electron propagators in each term have Keldysh space labels $[R \dots R]K[A \dots A]$ in a counterclockwise fashion. The index subsets $[R \dots R]$ and $[A \dots A]$ comprise $N - 1$ indices, and either subset can be empty (for example, see the next section for the quartic vertex).

The overall symmetry factor can be worked out as follows: $1/3!$ from the definition of $S_3[\varphi]$, three choices for the classical

leg, two choices for attaching one of the two remaining legs to the left external point, and a factor of i^2 from the two phonon propagators, amounting to $2 \times 3 \times i^2/3! = -1$. Thus, we obtain

$$\Pi_{\Delta, \mathbf{q}}^R(t_1, t_2) = - \int_{-\infty}^{+\infty} d\tau \frac{2\sqrt{N}\varphi_0(\tau)}{\sqrt{2}} V_{\mathbf{q}, -\mathbf{q}, 0}^{2,1,1}(t_1, t_2, \tau). \quad (\text{E19})$$

Note that $\varphi_{\mathbf{q}=0}(\tau) = (1/\sqrt{N}) \sum_j \varphi_j(\tau) = \sqrt{N}\varphi_0(\tau)$, where $\varphi_j(\tau) = \varphi_0(\tau)$ is the uniform ionic displacement at site j . Also, the factor $2/\sqrt{2}$ arises from the definition of the “classical” component, i.e., $\bar{\varphi}^c = (\varphi_0^+ + \varphi_0^-)\sqrt{2} = 2\varphi_0/\sqrt{2}$. To proceed,

we assume $\varphi_0(\tau) = A e^{i\Omega\tau}$ and a thermal state for electrons. Taking a Wigner transform $(t_1, t_2) \rightarrow (\omega, t)$, we find

$$\begin{aligned} \Pi_{\Delta, \mathbf{q}}^R(\omega, t) = & (-2i) A \frac{1}{N} \sum_{\mathbf{k}} |g_{\mathbf{k}, \mathbf{k}+\mathbf{q}}|^2 g_{\mathbf{k}, \mathbf{k}} \int_{-\infty}^{+\infty} d\tau e^{i\Omega\tau} \int_{-\infty}^{+\infty} dt e^{i\omega s} \int \frac{d\omega_1}{2\pi} \frac{d\omega_2}{2\pi} \frac{d\omega_3}{2\pi} e^{-i\omega_1 s} e^{-i\omega_2(t-s/2-\tau)} e^{-i\omega_3(\tau-t-s/2)} \\ & \times [\mathcal{G}_{\mathbf{k}+\mathbf{q}}^K(\omega_1) \mathcal{G}_{\mathbf{k}}^A(\omega_2) \mathcal{G}_{\mathbf{k}}^A(\omega_3) + \mathcal{G}_{\mathbf{k}+\mathbf{q}}^R(\omega_1) \mathcal{G}_{\mathbf{k}}^K(\omega_2) \mathcal{G}_{\mathbf{k}}^A(\omega_3) + \mathcal{G}_{\mathbf{k}+\mathbf{q}}^R(\omega_1) \mathcal{G}_{\mathbf{k}}^R(\omega_2) \mathcal{G}_{\mathbf{k}}^K(\omega_3)]. \end{aligned} \quad (\text{E20})$$

Performing the time integrals and subsequently the frequency integrals over ω_1 and ω_2 is a lengthy calculation and we quote the final result:

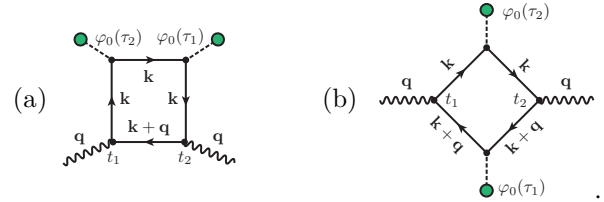
$$\Pi_{\Delta, \mathbf{q}}^R(\omega, t) = -4A e^{i\Omega t} \frac{1}{N} \sum_{\mathbf{k}} |g_{\mathbf{k}, \mathbf{k}+\mathbf{q}}|^2 g_{\mathbf{k}, \mathbf{k}} \frac{n_F(\xi_{\mathbf{k}}) - n_F(\xi_{\mathbf{k}+\mathbf{q}})}{(\omega - \xi_{\mathbf{k}+\mathbf{q}} + \xi_{\mathbf{k}} + i0^+)^2 - \Omega^2/4}. \quad (\text{E21})$$

We recall that the uniform displacement $\varphi_0(\tau)$ approximately takes the form $\varphi_0(\tau) \approx \varphi_0 + \varphi_1 \cos(2\Omega_{\text{drv}}\tau) = \varphi_0 + (\varphi_1/2)e^{2i\Omega_{\text{drv}}\tau} + (\varphi_1/2)e^{-2i\Omega_{\text{drv}}\tau}$ for a slowly ramped-up drive [see Eq. (5)]. Accordingly, the complete cubic self-energy correction is the sum of three terms obtained from replacing $(A, \Omega) \rightarrow (\varphi_0, 0)$, $(\varphi_1/2, +2\Omega_{\text{drv}})$, and $(\varphi_1/2, -2\Omega_{\text{drv}})$ in Eq. (E21).

Since $\Pi_{\Delta, \mathbf{q}}^R(\omega, t) \propto g_{\mathbf{k}, \mathbf{k}}$, it vanishes for screened Holstein-type electron-phonon couplings. Had $g_{\mathbf{k}, \mathbf{k}}$ been finite, however, $\Pi_{\Delta, \mathbf{q}}^R(\omega, t)$ would show a divergent behavior for $\mathbf{q} \approx 0$ and $\omega \simeq \Omega_{\text{drv}} \simeq \omega_{\mathbf{q}}$. In any event, $\Pi_{\Delta, \mathbf{q}}^R(\omega, t)$ remains $\mathcal{O}(g^3)$ and nondivergent for $\Omega_{\text{drv}} \sim \omega_{\mathbf{q}}/2$. Therefore, the electronic contribution to cubic lattice nonlinearity and its corresponding phonon self-energy corrections are negligible. We show in the next section that the situation is very different for the fourth-order correction.

3. Fourth-order correction: Electron-mediated quartic nonlinearity

We can similarly calculate the contribution of the quartic vertex [the last diagram in Eq. (E4)] to the phonon self-energy. In this case, two diagrams with different topologies comprise the leading-order contribution to the quartic self-energy correction:



We attach $A_1 e^{i\Omega_1 \tau_1}$ and $A_2 e^{i\Omega_2 \tau_2}$ to two of the external legs. This can be done in $3 \times 2 = 6$ and $2 \times 2 = 4$ different ways for (a) and (b) topologies, respectively:

$$\begin{aligned} \Pi_{\square, \mathbf{q}}^R(\omega, t) = & -\frac{1}{4!N} \int ds e^{i\omega s} \int d\tau_1 \sqrt{2N} A_1 e^{i\Omega_1 \tau_1} \int d\tau_2 \sqrt{2N} A_2 e^{i\Omega_2 \tau_2} [6 V_{\mathbf{q}, -\mathbf{q}, \mathbf{0}, \mathbf{0}}^{2,1,1,1}(t+s/2, t-s/2, \tau_1, \tau_2) \\ & + 4 V_{\mathbf{q}, \mathbf{0}, -\mathbf{q}, \mathbf{0}}^{2,1,1,1}(t+s/2, \tau_1, t-s/2, \tau_2)]. \end{aligned} \quad (\text{E22})$$

Performing the intermediate Keldysh space summations in Eq. (E8), we find

$$\begin{aligned} V_{\mathbf{q}, -\mathbf{q}, \mathbf{0}, \mathbf{0}}^{2,1,1,1}(t_1, t_2, \tau_1, \tau_2) = & \frac{3i}{N} \sum_{\mathbf{k}} \sum_{(a_1 \dots a_4) \in \mathcal{I}_4} |g_{\mathbf{k}, \mathbf{k}+\mathbf{q}}|^2 |g_{\mathbf{k}, \mathbf{k}}|^2 \mathcal{G}_{\mathbf{k}+\mathbf{q}}^{a_1}(t_1, t_2) \mathcal{G}_{\mathbf{k}}^{a_2}(t_2, \tau_1) \mathcal{G}_{\mathbf{k}}^{a_3}(\tau_1, \tau_2) \mathcal{G}_{\mathbf{k}}^{a_4}(\tau_2, t_2), \\ V_{\mathbf{q}, \mathbf{0}, -\mathbf{q}, \mathbf{0}}^{2,1,1,1}(t_1, \tau_1, t_2, \tau_2) = & \frac{3i}{N} \sum_{\mathbf{k}} \sum_{(a_1 \dots a_4) \in \mathcal{I}_4} |g_{\mathbf{k}, \mathbf{k}+\mathbf{q}}|^2 |g_{\mathbf{k}, \mathbf{k}}|^2 \mathcal{G}_{\mathbf{k}+\mathbf{q}}^{a_1}(t_1, \tau_1) \mathcal{G}_{\mathbf{k}+\mathbf{q}}^{a_2}(\tau_1, t_2) \mathcal{G}_{\mathbf{k}}^{a_3}(t_2, \tau_2) \mathcal{G}_{\mathbf{k}}^{a_4}(\tau_2, t_1), \end{aligned} \quad (\text{E23})$$

where $\mathcal{I}_4 = \{KAAA, RKAA, RRAA, RRRK\}$ denotes the set of Keldysh space labels of the four electron propagators. After a lengthy but straightforward calculation, we find the contribution of the first diagram to be

$$\begin{aligned} \Pi_{\square, \mathbf{q}}^{(a), R}(\omega, t) = & -\frac{3i}{2} A_1 A_2 e^{i(\Omega_1 + \Omega_2)t} \frac{1}{N} \sum_{\mathbf{k}} |g_{\mathbf{k}, \mathbf{k}+\mathbf{q}}|^2 |g_{\mathbf{k}, \mathbf{k}}|^2 \sum_{(a_1 \dots a_4) \in \mathcal{I}_4} \int \frac{d\omega_4}{2\pi} \mathcal{G}_{\mathbf{k}+\mathbf{q}}^{a_1}(\omega + \omega_4 - \Omega_1/2 - \Omega_2/2) \\ & \times \mathcal{G}_{\mathbf{k}}^{a_2}(\omega_4 - \Omega_1 - \Omega_2) \mathcal{G}_{\mathbf{k}}^{a_3}(\omega_4 - \Omega_2) \mathcal{G}_{\mathbf{k}}^{a_4}(\omega_4). \end{aligned} \quad (\text{E24})$$

Similarly, the contribution of the second diagram is found as

$$\begin{aligned} \Pi_{\square, \mathbf{q}}^{(b), R}(\omega, t) = & -2i A_1 A_2 e^{i(\Omega_1 + \Omega_2)t} \frac{1}{N} \sum_{\mathbf{k}} |g_{\mathbf{k}, \mathbf{k}+\mathbf{q}}|^2 |g_{\mathbf{k}, \mathbf{k}}|^2 \sum_{(a_1 \dots a_4) \in \mathcal{I}_4} \int \frac{d\omega_4}{2\pi} \mathcal{G}_{\mathbf{k}+\mathbf{q}}^{a_1}(\omega + \omega_4 - \Omega_1/2 - \Omega_2/2) \\ & \times \mathcal{G}_{\mathbf{k}+\mathbf{q}}^{a_2}(\omega + \omega_4 + \Omega_1/2 - \Omega_2/2) \mathcal{G}_{\mathbf{k}}^{a_3}(\omega_4 - \Omega_2) \mathcal{G}_{\mathbf{k}}^{a_4}(\omega_4). \end{aligned} \quad (\text{E25})$$

The ω_4 integration is easily performed since for each choice of Keldysh space labels $(a_1 \dots a_4) \in \mathcal{I}_4$, one of the electrons is on shell (Keldysh) and fixes the value of ω_4 . Assuming a coherent displacement like $\varphi_0(\tau) = \varphi_0 + \varphi_1 \cos(2\Omega_{\text{drv}}\tau)$, the

resulting self-energy contributions will have three contributions: a constant (dc) contribution, a contribution $\propto \cos(2\Omega_{\text{drv}}t)$, and a contribution $\propto \cos(4\Omega_{\text{drv}}t)$. Each contribution can be found by making appropriate choices for (A_1, Ω_1) and (A_2, Ω_2) . The most interesting contribution is the one $\propto \cos(4\Omega_{\text{drv}}t)$ which is found by substituting $(A_1, A_2; \Omega_1, \Omega_2) \rightarrow (\varphi_1/2, \varphi_1/2; \pm 2\Omega_{\text{drv}}, \pm \Omega_{\text{drv}})$ in Eqs. (E24) and (E25) and summing up the four contributions. We quote the final result from this lengthy calculation:

$$\Pi_{\square, \mathbf{q}}^{R, \text{ac}}(\omega, t) = \frac{3}{4} \varphi_1^2 \cos(4\Omega_{\text{drv}}t) \frac{1}{N} \sum_{\mathbf{k}} |g_{\mathbf{k}, \mathbf{k}+\mathbf{q}}|^2 |g_{\mathbf{k}, \mathbf{k}}|^2 \left\{ [1 - 2n_F(\xi_{\mathbf{k}})] \frac{A_{\mathbf{k}, \mathbf{q}}}{B_{\mathbf{k}, \mathbf{q}}} + [1 - 2n_F(\xi_{\mathbf{k}+\mathbf{q}})] \frac{C_{\mathbf{k}, \mathbf{q}}}{D_{\mathbf{k}, \mathbf{q}}} \right\}, \quad (\text{E26})$$

where

$$\begin{aligned} A_{\mathbf{k}, \mathbf{q}} &= \xi_{\mathbf{k}}^2 (\xi_{\mathbf{k}+\mathbf{q}} - \omega)(2\xi_{\mathbf{k}} + 3\xi_{\mathbf{k}+\mathbf{q}} - 3\omega) + 4\xi_{\mathbf{k}} \Omega_{\text{drv}}^2 (\xi_{\mathbf{k}} - 2\xi_{\mathbf{k}+\mathbf{q}} + 2\omega) - 64\Omega_{\text{drv}}^4, \\ B_{\mathbf{k}, \mathbf{q}} &= (\xi_{\mathbf{k}}^4 - 20\xi_{\mathbf{k}}^2 \Omega_{\text{drv}}^2 + 64\Omega_{\text{drv}}^4)(\xi_{\mathbf{k}+\mathbf{q}} - \omega)[(\xi_{\mathbf{k}+\mathbf{q}} - \omega)^2 - 4\Omega_{\text{drv}}^2], \\ C_{\mathbf{k}, \mathbf{q}} &= \xi_{\mathbf{k}+\mathbf{q}}(2\xi_{\mathbf{k}} + \xi_{\mathbf{k}+\mathbf{q}} + 2\omega) + 4\Omega_{\text{drv}}^2, \\ D_{\mathbf{k}, \mathbf{q}} &= (\xi_{\mathbf{k}} + \omega)(\xi_{\mathbf{k}+\mathbf{q}}^4 - 4\Omega_{\text{drv}}^2)[(\xi_{\mathbf{k}+\mathbf{q}} + \omega)^2 - 4\Omega_{\text{drv}}^2]. \end{aligned} \quad (\text{E27})$$

As in the cubic vertex case, this contribution also vanishes for a perfectly screened Holstein-type electron-phonon coupling since $\Pi_{\square, \mathbf{q}}^{R, \text{ac}}(\omega, t) \propto |g_{\mathbf{k}, \mathbf{k}}|^2$. In a more realistic model, $g_{\mathbf{k}, \mathbf{k}}$ is generically nonvanishing.

The \mathbf{k} integral in Eq. (E26) can be calculated in the limit $\mathbf{q} \approx 0$ and assuming a constant electronic density of states and zero temperature. In the vicinity of the parametric resonance $\Omega_{\text{drv}} \sim \omega_{\mathbf{q}}/2$, we find

$$\Pi_{\square, \mathbf{q} \approx 0}^{R, \text{ac}}(\omega_{\mathbf{q}}, t) \simeq \cos(2\omega_{\mathbf{q}}t) \frac{3\nu(0) |g_{\mathbf{k}, \mathbf{k}}|^4 \varphi_1^2}{2\omega_{\mathbf{q}}^2} \ln \left[\frac{2\Omega_{\text{drv}} - \omega_{\mathbf{q}}}{4\omega_{\mathbf{q}}} \right] + \mathcal{O}(1). \quad (\text{E28})$$

The logarithmic divergence could be anticipated from $D_{\mathbf{k}, \mathbf{q}} \propto (\omega_{\mathbf{q}}^2 - 4\Omega_{\text{drv}}^2)$ in the limit $\omega = \omega_{\mathbf{q}}$ and $\mathbf{q} \approx 0$.

The above finding has a consequential implication: the electronic contribution to the lattice nonlinearity, even though it is $\sim \mathcal{O}(g^2)$ and small in general, in the presence of coherent lattice oscillations leads to a self-energy correction that diverges logarithmically in the vicinity of $\Omega_{\text{drv}} \sim \omega_{\mathbf{q}}/2$. Thus, even if purely ionic contributions to the lattice nonlinearity are small, large nonlinearities will be *dynamically generated* as a matter of coupling to electrons. Also, note that $\Pi_{\square, \mathbf{q} \approx 0}^{R, \text{ac}}(\omega_{\mathbf{q}}, t) \propto \cos(2\omega_{\mathbf{q}}t)$ which is precisely the COM time dependence required for giving rise to parametric amplification of the lattice response as discussed in Sec. III.

APPENDIX F: SUMMARY OF NUMERICAL METHODS

In this Appendix, we provide a summary of numerical methods for solving the quantum Floquet-Boltzmann kinetic equations for the lattice and electronic degrees of freedom. In reality, the two systems are coupled and must propagate forward in time self-consistently. The perturbative framework adopted in this work (when physically permissible) allows us to study the two systems in iterations: the dynamics of the lattice is worked out assuming unperturbed equilibrium electron propagators, the nonequilibrium correction to electron propagators electrons are worked out on the backdrop of the driven lattice, and so on; see Fig. 7. This iterative procedure is expected to converge to the self-consistent solution of the fully coupled system in the weak-coupling limit.

1. Solving the quantum Floquet-Boltzmann kinetic equation for lattice displacement and phonon propagators

The quantum Floquet-Boltzmann kinetic equations for the lattice displacement and phonon propagators were worked

out in Sec. IV D. The final result is the coupled system of equations given in Eqs. (44a), (45a) and (45b), and (46a) and (46b). Coupling to electrons only appears in the bath term $\Pi_{n, m}^{(\ell); R/A/K}(\omega; t)$, which we assume is given to us in this section. We take a further simplifying step and neglect the COM time dependence of $\Pi^{(\ell)}$ which is indeed the case if the bath is approximately calculated using equilibrium electron propagators (see Appendix E 1). The following analysis can be easily generalized for time-dependent baths, e.g., as required for the next iterations if one were to follow the perturbative decoupling recipe mentioned above.

The major difficulty in time stepping Eqs. (45a) and (45b) and (46a) and (46b) using ordinary differential equation (ODE) solvers is threefold:

(1) Time derivatives appear on both sides of equations, and ∂_t of different Floquet components $\partial_t \mathcal{D}_{n, m}^{R/K}(\omega; t)$ are coupled due to the lattice nonlinearity and the bath. In other words, $\partial_t \mathcal{D}_{n, m}^{R/K}(\omega; t)$ is only *implicitly* given by Eqs. (45a) and (45b) and (46a) and (46b).

(2) We have two sets of evolution equations for the retarded and Keldysh propagators: one obtained from the forward KB equation [Eqs. (45a) and (46a)] and another from the backward KB equation [Eqs. (45b) and (46b)]. In general, these two are complementary. For instance, the direct numerical solution of two-time propagators requires the forward and backward equations to step the propagators forward in the first and second times, respectively (e.g., see Ref. [70]). In the kinetic approximation, however, only the COM time is stepped forward while the relative time is transformed to the frequency domain and is carried as a label. In theory, one may choose to work with either of the forward or backward equations for time stepping as both are correct to $\mathcal{O}(\partial_t)$. However, the mixing of large nongradient terms and small gradient terms leads to undesirable numerical errors.

(3) We found the system to be marginally stiff, requiring a robust ODE solver with adaptive time stepping and local error control. This leads to unavoidably long run times. The application of stiff solvers is challenging as the Jacobian of the system is dense and is difficult to calculate.

Let us note that we do not need to calculate \mathcal{D}^A as a separate quantity since the identity $\mathcal{D}^R(t_1, t_2) = \mathcal{D}^A(t_2, t_1)$ implies $\mathcal{D}^A(\omega; t) = \mathcal{D}^R(-\omega; t)$. Furthermore, the exact identities $\mathcal{D}_{-n}^R(\omega) = [\mathcal{D}_n^R(-\omega)]^*$, $i\mathcal{D}_{-n}^K(\omega) = [i\mathcal{D}_n^K(-\omega)]^*$, and $i\mathcal{D}_n^K(-\omega) = i\mathcal{D}_n^K(\omega)$ allow us to restrict the numerical calculation to non-negative Floquet indices.

Setting up the linear system and calculating the explicit $\partial_t \mathcal{D}_{n,m}^{R/K}(\omega; t)$. The second issue mentioned above can be circumvented using antisymmetric and symmetric combinations of Eqs. (45a), (45b) and (46a), (46b), respectively. The issue of implicitness, however, remains challenging. In particular, the ω integral appearing in $\chi_n(t)$ and the appearance of $\partial_t U_n(t)$ in the kinetic equations implies that neither Floquet indices nor ω are “good” numbers. In other words, the kinetic equations of the lattice displacement and phonon propagators pose a dense linear system for $\partial_t \mathcal{D}_{n,m}^{R/K}(\omega; t)$ and $\partial_t \varphi_n(t)$. In order to find $\partial_t \varphi_n(t)$ and $\partial_t \mathcal{D}_{n,m}^{R/K}(\omega; t)$ explicitly, at each time t , we carefully index $\partial_t \mathcal{D}_{n,m}^{R/K}(\pm\omega; t)$ and $\partial_t \varphi_n(t)$ for all (ω, n, m) , cast the coupled kinetic equations into a linear system, and solve it via LU decomposition.

We perform the calculations on a regular frequency grid $\omega \in [-\omega_M, \omega_M]$ where ω_M is a high-frequency cutoff. The grid spacing is chosen as rational fraction of $\Omega/2$ close to 0.1 γ_ℓ in order to ensure that $\omega \pm n\Omega/2$ belongs to the grid. This allows us to identify a large fraction of unknown time derivatives and matrix elements with one another and greatly reduce the dimension of the linear system. The ω derivatives are calculated using the five-point finite-difference approximation, and the ω integral appearing in Eq. (44c) is approximated using the trapezoid rule. We choose the Floquet cutoff $n_D = 2$, and the frequency cutoff $\omega_M = 2\omega_0 + 5\gamma_\ell + (n_D + 1)\Omega$. This choice ensures that all involved propagators remain small and negligible for $|\omega| > \omega_M$. We carefully checked that increasing ω_M and n_D had a negligible and controllably small effect on the results. For an ω grid with ~ 500 points, one needs to solve a linear system of size $\sim 6000 \times 6000$ for each calculation of the explicit time derivatives.

Initial thermal state and renormalized phonon frequency. The lattice is in a thermal equilibrium state at the bath temperature before the drive ramped up. To find conditions describing

the equilibrium state, we set the external drive and time derivatives to zero in the described evolution equations, assume $\varphi_n(t) \rightarrow \varphi_0 \delta_{n,0}$, $U_n(t) \rightarrow U_0 \delta_{n,0}$, $\chi_n(t) \rightarrow \chi_0 \delta_{n,0}$, and $\mathcal{D}_n^{R/A/K}(\omega) \rightarrow \delta_{n,0} \mathcal{D}_0^{R/A/K}(\omega)$. This leads to the following set of coupled equations:

$$\begin{aligned} & \left(\omega_0^2 - \frac{1}{3} \omega_0 \kappa_4 \varphi_0^2 - \omega_0 \kappa_4 \chi_0 - \omega_0 \kappa_3 \varphi_0 \right) \varphi_0 - \omega_0 \kappa_3 \chi_0 = 0, \\ & \mathcal{D}_0^{R/A}(\omega) = \frac{2\omega_0}{\omega^2 - \omega_0^2 - 2\omega_0 \omega_L - 2\omega_0 U_0 \pm i\gamma_\ell \omega}, \\ & i\mathcal{D}_0^K(\omega) = \frac{4\omega_0 \gamma_\ell \omega \coth(\beta\omega/2)}{(\omega^2 - \omega_0^2 - 2\omega_0 \omega_L - 2\omega_0 U_0)^2 + \gamma_\ell^2 \omega^2}, \\ & U_0 = -\frac{\kappa_4}{2} \varphi_0^2 - \frac{\kappa_4}{2} \chi_0 - \kappa_3 \varphi_0, \\ & \chi_0 = \frac{1}{2} \int_{-\infty}^{+\infty} \frac{d\omega}{2\pi} i\mathcal{D}_0^K(\omega). \end{aligned} \quad (\text{F1})$$

The first and last two equations must be solved self-consistently, leading to a renormalized phonon frequency:

$$\Omega_0 \equiv \sqrt{\omega_0^2 + 2\omega_0 \bar{\omega}_L + 2\omega_0 U_0}. \quad (\text{F2})$$

Numerical time stepping. Provided that $\{\varphi_n(t)\}$, $\{U_n(t)\}$, $\{\chi_n(t)\}$ and $\{i\mathcal{D}_n^{R/K}(\omega; t)\}$ are known for all ω on a regular grid, we obtain the explicit time derivatives of these quantities using by solving a linear system as described earlier. We can then invoke an explicit ODE solver to perform time stepping. Here, we integrated the ODE using the adaptive Runge-Kutta-Fehlberg(4,5) method with local relative error tolerance of 10^{-6} .

2. Solving the quantum Floquet-Boltzmann kinetic equation for electrons

The quantum Floquet-Boltzmann kinetic equation for $\{\psi_n(\omega; t)\}$ [see Eq. (58)] was derived in Sec. IV E 3. Similar to the kinetic equation for the phonons, this kinetic equation is also a formidably dense implicit integral equation for $\{\partial_t \psi_n(\omega; t)\}$ in which all frequencies and Floquet indices are coupled and defy the immediate application of an explicit ODE solver. In this section, we describe a numerical strategy for solving this equation.

Preliminaries. As a first step, we use the exact identities $\psi_{n,m}^*(\omega) = \psi_{-n,m}(\omega)$ and $\Sigma_{n,m}^A(\omega) = [\Sigma_{-n,m}^R(\omega)]^*$ to cast Eq. (69) into a more useful form:

$$\begin{aligned} \partial_t \psi_n &= in\Omega \psi_n + i\Sigma_n^K - i\Sigma_{n',n'-n}^R \psi_{n',n'-n}^* + i\Sigma_{n',n'+n}^{R,*} \psi_{n',n'+n} + \frac{1}{2} \partial_\omega \Sigma_{n',n'-n}^R \partial_t \psi_{n',n'-n}^* + \frac{1}{2} \partial_\omega \Sigma_{n',n'+n}^{R,*} \partial_t \psi_{n',n'+n} \\ &\quad - \frac{1}{2} \partial_t \Sigma_{n',n'-n}^R \partial_\omega \psi_{n',n'-n}^* - \frac{1}{2} \partial_t \Sigma_{n',n'+n}^{R,*} \partial_\omega \psi_{n',n'+n}. \end{aligned} \quad (\text{F3})$$

We have dropped the common $(\omega; t)$ argument from all quantities for brevity. Summation over repeated indices is implied everywhere in this section. The numerical integration of this equation is complicated by the fact that the self-energies are functionals of ψ , so that $\partial_t \Sigma^R$ terms implicitly involve $\partial_t \psi$. This functional dependence can be made explicit using Eqs. (70a) and (70b):

$$\begin{aligned} \Sigma_n^R(\omega; t) &= \text{F}[i\mathcal{D}_n^K]_n(t) + \int_0^\infty d\omega' \text{K}[\rho]_{n-n'}(\omega, \omega'; t) \psi_n(\omega'; t), \\ i\Sigma_n^K(\omega; t) &= \pi \int_{-\infty}^{+\infty} d\nu i\text{F}_{n-n'}^K(\nu; t) \psi_n(\omega - \nu; t), \end{aligned} \quad (\text{F4})$$

where

$$\begin{aligned}
F[i\mathcal{D}^K]_n(t) &= -i\pi \int_0^\infty dv iF_n^K(v;t), \\
\mathbf{K}[\rho]_n(\omega, \omega'; t) &= \mathbf{K}[\rho]_n^{PV,+}(\omega, \omega'; t) + \mathbf{K}[\rho]_n^{\delta,+}(\omega, \omega'; t) + \mathbf{K}[\rho]_n^{PV,-}(\omega, \omega'; t) + \mathbf{K}[\rho]_n^{\delta,-}(\omega, \omega'; t), \\
\mathbf{K}[\rho]_n^{PV,\pm}(\omega, \omega'; t) &= PV \int_{-\infty}^{+\infty} dv \frac{\rho_n(v;t)}{\omega \mp \omega' - v}, \\
\mathbf{K}[\rho]_n^{\delta,\pm}(\omega, \omega'; t) &\equiv -i\pi \int_{-\infty}^{+\infty} dv \rho_n(v;t) \delta(\omega \mp \omega' - v).
\end{aligned} \tag{F5}$$

The following useful identities can be established using the symmetries of ψ , $F^{K/\rho}$, and the properties of Kramers-Kronig transforms:

$$\mathbf{K}[\rho]_n^{PV,\pm}(-\omega, \omega'; T) = \mathbf{K}[\rho]_n^{PV,\mp}(\omega, \omega'; T) \tag{F6}$$

$$= [\mathbf{K}[\rho]_{-n}^{PV,\pm}(-\omega, \omega'; T)]^*, \tag{F7}$$

$$\mathbf{K}[\rho]_n^{\delta,\pm}(-\omega, \omega'; T) = -\mathbf{K}[\rho]_n^{\delta,\mp}(\omega, \omega'; T) \tag{F8}$$

$$= -[\mathbf{K}[\rho]_{-n}^{\delta,\pm}(-\omega, \omega'; T)]^*, \tag{F9}$$

$$\Sigma_n^R(-\omega; T) = -[\Sigma_{-n}^R(\omega; T)]^*, \tag{F10}$$

$$i\Sigma_n^K(-\omega; T) = -i\Sigma_n^K(\omega; T) = [i\Sigma_{-n}^K(\omega; T)]^*. \tag{F11}$$

As a result, we only need to calculate each quantity only for $\omega > 0$. Also, save for Σ_n^R , all other quantities can be calculated for $n \geq 0$.

The frequency grid. We proceed by generating a grid X_ω in the interval $[0, \omega_c]$. Here, ω_c is an appropriate cutoff $\omega_c \gg 1/\beta, \omega_0, \Omega$. We generate the grid X_ω such that for all $\omega \in X_\omega$, if $\omega_m \equiv \omega + m\Omega/2 < \omega_c$, then $\omega_m \in X_\omega$. We call such a grid X_ω as a *Floquet-closed* grid. We will shortly see that a Floquet-closed grid leads to a significant reduction in computational complexity by allowing us to reuse previously calculated integrals. In practice, it is necessary to generate a nonuniform grid that emphasizes on the $\omega \lesssim 1/\beta$ region. To this end, we create two uniform grids, $X_\omega^{\text{th}} \in [0, c/\beta]$ and $X_\omega^> \in [c/\beta, \omega_c]$, and concatenate them. Crucially, we choose the grid spacings $\delta\omega^{\text{th}}$ and $\delta\omega^>$ such that both are integer multiples of $\Omega/(2N)$ for some N . Once we have this basic two-scale grid, we pool together $|X_\omega^> \cup X_\omega^{\text{th}} + m\Omega/2|$ for $|m| < m_c$ and keep the unique points to find X_ω .

Calculating the required matrix elements. We assume that $\{\psi_n(\omega; t)\}$ are known for $\omega \in X_\omega$ and $0 \leq n \leq N_\psi$ for some cutoff $N_\psi \geq N_D$. It is trivial to calculate $i\Sigma^K$ numerically based on Eq. (F4) using a quadrature formula. To find Σ^R and $\partial_t \Sigma^R$, we first calculate $F[i\mathcal{D}^K]_n$ and $\partial_t F[i\mathcal{D}^K]_n$, both of which are trivial. To calculate the contribution from $\{\rho_n\}$, we calculate the following quantities:

$$\mathbf{K}_{n,jk}[\rho](t) \equiv \int_{\omega_j}^{\omega_{j+1}} d\omega' \mathbf{K}_n[\rho](\omega_j, \omega_k; t),$$

$$\partial_t \mathbf{K}[\rho]_{n,jk}(t) \equiv \int_{\omega_j}^{\omega_{j+1}} d\omega' \mathbf{K}_n[\partial_t \rho](\omega_j, \omega_k; t),$$

$$\tilde{\mathbf{K}}[\rho]_{n,jk}(t) \equiv \int_{\omega_c}^{\infty} d\omega' \mathbf{K}_n[\rho](\omega_j, \omega_k; t),$$

$$\partial_t \tilde{\mathbf{K}}[\rho]_{n,jk}(t) \equiv \int_{\omega_c}^{\infty} d\omega' \mathbf{K}_n[\partial_t \rho](\omega_j, \omega_k; t), \tag{F12}$$

for $\omega_j, \omega_k \in X_\omega$. The $\tilde{\mathbf{K}}$ terms stem from $\int_{\omega_c}^{\infty} d\omega'$ assuming $\psi_n(\omega') \approx \delta_{n,0}$ for $\omega' > \omega_c$. The proper ω' integrals must be approximated with quadratures much finer than X_ω grid spacing, and this is necessary since the integrands can vary on shorter scales than the grid spacing of a practically sized X_ω . The improper ω' integrals can be calculated using Möbius transformation and then using standard proper quadratures. Calculating $\mathbf{K}_{n,jk}[\rho](t)$ and $\mathbf{K}_{n,jk}[\partial_t \rho](t)$ is quite expensive as the integrand is given by a Kramers-Kronig integral and must be obtained numerically for every integration point. Having calculated these quantities, we may compose the full expression for $\Sigma_n^R(\omega_j; t)$ and $\partial_t \Sigma_n^R(\omega_j; t)$ approximately as

$$\begin{aligned}
\Sigma^R(\omega_j; t) &\simeq F[i\mathcal{D}^K]_n(t) + \sum_{k=0}^{N_\omega-1} \mathbf{K}[\rho]_{n-n',jk}(t) \frac{\psi_{n'}(\omega_k; t) + \psi_{n'}(\omega_{k+1}; t)}{2} + \tilde{\mathbf{K}}_{n,j}[\rho](t), \\
\partial_t \Sigma^R(\omega_j; t) &\simeq F[\partial_t i\mathcal{D}^K]_n(t) + \sum_{k=0}^{N_\omega-1} \partial_t \mathbf{K}[\rho]_{n-n',jk}(t) \frac{\psi_{n'}(\omega_k; t) + \psi_{n'}(\omega_{k+1}; t)}{2} \\
&\quad + \sum_{k=0}^{N_\omega-1} \mathbf{K}[\rho]_{n-n',jk}(t) \frac{\partial_t \psi_{n'}(\omega_k; t) + \partial_t \psi_{n'}(\omega_{k+1}; t)}{2} + \partial_t \tilde{\mathbf{K}}_{n,j}[\rho](t).
\end{aligned} \tag{F13}$$

Here, N_ω is the number of grid points in X_ω . We have also used linear interpolation for the values of ψ between consecutive grid points. If $\omega_c \gg 1/\beta$, the high-energy tail of Fermi distribution indeed remains intact (i.e., we assume ω_c is large enough so that no particles will be excited to energies above ω_c). The important point about using the Floquet closed X_ω is that once we

calculate $K_n(\omega_j, \omega_k)$ for $\omega_j \in X_\omega$, we immediately get $K_n(\omega_j + m\Omega/2, \omega_k)$ for all m using a combination of shifts, inversions, and conjugation [see Eq. (F6)]. In other words, we do not need to perform the expensive calculation of K for all m -shifted ω points.

Setting up the linear system and time stepping. Plugging Eq. (F13) expression into Eq. (F3), we find an explicit linear system for $\partial_t \psi_n(\omega_j; t)$ for $\omega_j \in X_\omega$. The ω derivatives are found using five-point finite-difference approximation on the X_ω grid. This system can be mapped to a matrix equation by (1) indexing $\{\text{Re } \psi_n(\omega_j; t), \text{Im } \psi_n(\omega_j; t)\}$ for all n and $\omega_j \in X_\omega$, and (2) setting up a mapping from $\{\text{Re } \psi_n(\omega_j + m\Omega/2; t), \text{Im } \psi_n(\omega_j + m\Omega/2; t)\}$ to the corresponding indexed values for all m using the symmetries of ψ . Having a recipe to calculate $\partial_t \psi_n(\omega; t)$, we proceed and integrate the ODE using the adaptive Runge-Kutta-Fehlberg(4,5) method with local relative error tolerance of 10^{-6} .

3. Numerical analysis of the spectrum of Floquet-Migdal-Eliashberg gap functional

Calculating the spectrum of the Floquet-Migdal-Eliashberg (FME) gap functional, given in Eq. (85), involves three steps: (1) calculating $\Sigma_{n,m}^{R/K}(\omega; t)$ in the normal state, (2) calculating the Floquet matrix elements of the anomalous response $\mathbf{Q}_{n',m'}^{n,m}(\omega; t)$, and (3) calculating the spectrum of the FME gap functional.

The first step is identical to the procedure described in Appendix F2. In the equilibrium-electron approximation, we use $\psi_{n,m}(\omega; t) \rightarrow \delta_{n,0} \tanh[\beta(\omega - m\Omega/2)/2]$ in calculating the self-energies rather than using $\psi_{n,m}(\omega; t)$ found from solving the Floquet-Boltzmann equation for electrons.

The second step involves inverting the coefficient matrix of $\delta\mathcal{F}_{n,m}^R(\omega; t)$ which can be read from Eq. (81a). To this end, we truncate the intermediate n' Floquet band index summation to $|n'| \leq N_\phi$ and Floquet quasimomentum indices to $|m| \leq N_m$. The truncated system of equations is then carefully mapped to a proper linear system $\sum_{n'=-N_\phi}^{+N_\phi} \sum_{m'=-N_m}^{+N_m} C_{n',m'}^{n,m}(\omega; t) \delta\mathcal{F}_{n,m}^R(\omega; t) = -2\pi i \phi_{n,m}(\omega; t)$. The Floquet matrix elements of the anomalous response are readily found by inverting $C_{n',m'}^{n,m}$ in the space of paired Floquet indices (n, m) :

$$\mathbf{Q}_{n',m'}^{n,m}(\omega; t) = -2\pi i [C^{-1}]_{n',m'}^{n,m}. \quad (\text{F14})$$

In practice, we found the final results to be accurate to 10^{-4} with the choice $N_\phi = N_m = N_D + 2$ where N_Σ is the previously chosen Floquet band cutoff in calculating the retarded self-energy.

The last step is slightly more involved. The overall strategy is to formally interpolate $\Delta_n(\omega; t)$ over a finite grid G_ω , plug the interpolation formula in Eq. (85), read off the coefficients of $\Delta_n(\omega \in G_\omega; t)$, and calculate its spectrum. Even though a brute-force discretization is equally applicable in principle, the uniform grid must be very dense in order to obtain accurate results, leading to calculating the spectrum of intractably large matrices. The interpolation procedure allows us to obtain accurate results using much coarser grids.

Setting up the grid. We generate G_ω by concatenating three grids $G_\omega = G_\omega^{(1)} \cup G_\omega^{(2)} \cup G_\omega^{(3)}$ where $G_\omega^{(1)}$ is a uniform grid for $\omega \in [0, 10/\beta)$ where $\beta^{-1} \sim 0.05 \Omega_0$ is the typical effective temperature of electrons, $G_\omega^{(2)}$ in another uniform grid for $\omega \in [10/\beta, \omega_c)$ where $\omega_c \sim 10 \Omega_0$ is a typical scale beyond which variations of $\Delta_n(\omega; t)$ becomes negligible, and, finally, $G_\omega^{(3)}$ is a log-scaled grid for $\omega \in [\omega_c, \infty)$. In practice, we found allocating 100 points for each subgrid produced results accurate to 10^{-4} .

Setting up the coefficient matrix. We approximate $\Delta_n(\omega; t)$ over G_ω using a linear interpolant:

$$\Delta_n(\omega; t) \approx \frac{\omega_{j_\omega+1} - \omega}{\omega_{j_\omega+1} - \omega_{j_\omega}} \Delta_n(\omega_{j_\omega}; t) + \frac{\omega - \omega_{j_\omega}}{\omega_{j_\omega+1} - \omega_{j_\omega}} \Delta_n(\omega_{j_\omega+1}; t), \quad (\text{F15})$$

where j_ω is the nearest grid point to the left of ω . Plugging this ansatz into Eq. (85), we find

$$\Delta_n(\omega_j; t) = \frac{i\omega_j}{2\pi} \sum_{n', n'', m'}^{|G_\omega|} \{ \mathbf{Q}_{n',m'}^{n,0}(\omega_j; t) \mathbf{K}_{n'',m'}^\Delta(\omega_j, \omega_k; t) \Delta_{n'-n''}(\omega_k; t) - [\mathbf{Q}_{n',m'}^{-n,0}(\omega; t)]^* \mathbf{K}_{n'',m'}^{\Delta*}(\omega_j, \omega_k; t) \Delta_{n'-n''}^*(\omega_k; t) \}, \quad (\text{F16})$$

where

$$\mathbf{K}_{n,m}^\Delta(\omega_j, \omega_k; t) = \int_{\omega_{k-1}}^{\omega_k} \frac{d\omega'}{\omega'} K_{n,m}(\omega_j, \omega'; t) \frac{\omega' - \omega_{k-1}}{\omega_k - \omega_{k-1}} + \int_{\omega_k}^{\omega_{k+1}} \frac{d\omega'}{\omega'} K_{n,m}(\omega_j, \omega'; t) \frac{\omega_{k+1} - \omega'}{\omega_{k+1} - \omega_k}. \quad (\text{F17})$$

The end points $k = |G_\omega|$ and 1 only get contributions from the first and second integrals, respectively. The ω' integrals are performed via an adaptive Gauss-Kronrod quadrature and are refined until a tolerance of 10^{-6} is achieved. The kernel $K_{n,m}(\omega, \omega'; t)$ is given by Eq. (84) and each evaluation requires performing a numerical Kramers-Kronig transform. Calculating the matrix elements $\mathbf{K}_{n,m}^\Delta(\omega_j, \omega_k; t)$ is the most computationally expensive part of this section. Finally, we decompose $\Delta_n(\omega; t)$ into real and imaginary parts and use

the relations $\text{Re}[\Delta_n(\omega; t)] = \text{Re}[\Delta_{-n}(\omega; t)]$, $\text{Im}[\Delta_n(\omega; t)] = -\text{Im}[\Delta_{-n}(\omega; t)]$ to cast Eq. (F16) as a matrix equation. The coefficient matrix acts on space of bundled labels (n, j, o) where n is the Floquet index, j is the grid point index, and $o = 0, 1$ indicates real and imaginary components of Δ_n .

Finally, we impose cutoffs N_Δ and N_m over the Floquet band index of Δ and the internal m' quasimomentum summation. The Floquet cutoff for K is $N_K = N_D + N_\psi$ where N_D

and N_ψ are the previously chosen Floquet cutoffs for phonon propagators and electron energy statistics, respectively. We found $N_\Delta = N_m = N_K + 2$ to produce results accurate to

10^{-4} . Assuming $N_\psi = N_D = 2$ and $|G_\omega| = 300$, the final coefficient matrix has a dimension 3900×3900 and its spectrum can be easily found numerically.

-
- [1] D. N. Basov, R. D. Averitt, D. Van Der Marel, M. Dressel, and K. Haule, Electrodynamics of correlated electron materials, *Rev. Mod. Phys.* **83**, 471 (2011).
- [2] C. Giannetti, M. Capone, D. Fausti, M. Fabrizio, F. Parmigiani, and D. Mihailovic, Ultrafast optical spectroscopy of strongly correlated materials and high-temperature superconductors: A non-equilibrium approach, *Adv. Phys.* **65**, 58 (2016).
- [3] A. F. G. Wyatt, V. M. Dmitriev, W. S. Moore, and F. W. Sheard, Microwave-Enhanced Critical Supercurrents in Constricted Tin Films, *Phys. Rev. Lett.* **16**, 1166 (1966).
- [4] A. H. Dayem and J. J. Wiegand, Behavior of thin-film superconducting bridges in a microwave field, *Phys. Rev.* **155**, 419 (1967).
- [5] G. M. Eliashberg, Sverkhprovodimost' plenok, stimulirovannaya vysokochastotnym polem, Pis'ma v ZhETF **11**, 186 (1970) [Film superconductivity stimulated by a high-frequency field, JETP Lett. **11**, 114 (1970)].
- [6] J.-J. Chang and D. J. Scalapino, Nonequilibrium superconductivity, *J. Low Temp. Phys.* **31**, 1 (1978).
- [7] J. A. Pals and J. Dobben, Measurements of microwave-enhanced superconductivity in aluminum strips, *Phys. Rev. B* **20**, 935 (1979).
- [8] M. G. Blamire, E. C. G. Kirk, J. E. Evetts, and T. M. Klapwijk, Extreme Critical-Temperature Enhancement of Al by Tunneling in Nb/AlO_x/Al/AlO_x/Nb Tunnel Junctions, *Phys. Rev. Lett.* **66**, 220 (1991).
- [9] D. R. Heslinga and T. M. Klapwijk, Enhancement of superconductivity far above the critical temperature in double-barrier tunnel junctions, *Phys. Rev. B* **47**, 5157 (1993).
- [10] P. V. Komissinski and G. A. Ovsyannikov, Superconductivity enhancement in thin films of niobium in superconducting double-barrier structures, *Phys. Rev. B* **54**, 13184 (1996).
- [11] A. Robertson and V. M. Galitski, Nonequilibrium enhancement of cooper pairing in cold fermion systems, *Phys. Rev. A* **80**, 063609 (2009).
- [12] M. Mitrano, A. Cantaluppi, D. Nicoletti, S. Kaiser, A. Perucchi, S. Lupi, P. Di Pietro, D. Pontiroli, M. Riccò, S. R. Clark *et al.*, Possible light-induced superconductivity in K₃C₆₀ at high temperature, *Nature (London)* **530**, 461 (2016).
- [13] O. Gunnarsson, Alkali-Doped Fullerenes, *Narrow-Band Solids with Unusual Properties* (World Scientific, Singapore, 2004), Vol. 10.
- [14] O. Gunnarsson, Superconductivity in fullerides, *Rev. Mod. Phys.* **69**, 575 (1997).
- [15] C. Grimaldi, L. Pietronero, and S. Strässler, Nonadiabatic superconductivity. II. generalized eliashberg equations beyond migdals theorem, *Phys. Rev. B* **52**, 10530 (1995).
- [16] A. B. Migdal, Vzaimodeistvie elektronov s kolebaniyami reshetki v normal'nom metalle, ZhETF **34**, 1438 (1958) [Interaction between electrons and lattice vibrations in a normal metal, Sov. Phys.–JETP **7**, 996 (1958)].
- [17] G. M. Eliashberg, Vzaimodeistvie elektronov s kolebaniyami reshetki v sverkhprovodnike, ZhETF **38**, 966 (1960) [Interactions between electrons and lattice vibrations in a superconductor, Sov. Phys.–JETP **11**, 696 (1960)].
- [18] K.-H. Bennemann and J. B. Ketterson, *Superconductivity: Volume 1: Conventional and Unconventional Superconductors, Volume 2: Novel Superconductors* (Springer, Berlin, 2008).
- [19] A. F. Kemper, M. A. Sentef, B. Moritz, J. K. Freericks, and T. P. Devereaux, Direct observation of Higgs mode oscillations in the pump-probe photoemission spectra of electron-phonon mediated superconductors, *Phys. Rev. B* **92**, 224517 (2015).
- [20] M. A. Sentef, A. F. Kemper, A. Georges, and C. Kollath, Theory of light-enhanced phonon-mediated superconductivity, *Phys. Rev. B* **93**, 144506 (2016).
- [21] D. F. Martinez, Floquet–Green function formalism for harmonically driven hamiltonians, *J. Phys. A: Math. Gen.* **36**, 9827 (2003).
- [22] N. Tsuji, T. Oka, and H. Aoki, Correlated electron systems periodically driven out of equilibrium: Floquet + DMFT formalism, *Phys. Rev. B* **78**, 235124 (2008).
- [23] H. Aoki, N. Tsuji, M. Eckstein, M. Kollar, T. Oka, and P. Werner, Nonequilibrium dynamical mean-field theory and its applications, *Rev. Mod. Phys.* **86**, 779 (2014).
- [24] M. Genske and A. Rosch, Floquet-Boltzmann equation for periodically driven fermi systems, *Phys. Rev. A* **92**, 062108 (2015).
- [25] L. P. Kadanoff and G. A. Baym, *Quantum Statistical Mechanics* (Perseus, Cambridge, MA, 1962).
- [26] P. Danielewicz, Quantum theory of nonequilibrium processes, I, *Ann. Phys. (NY)* **152**, 239 (1984).
- [27] J. Berges, Introduction to nonequilibrium quantum field theory, *AIP Conf. Proc.* **739**, 3 (2004).
- [28] M. Knap, M. Babadi, G. Refael, I. Martin, and E. Demler, Dynamical cooper pairing in non-equilibrium electron-phonon systems, *Phys. Rev. B* **94**, 214504 (2016).
- [29] A. Komnik and M. Thorwart, BCS theory of driven superconductivity, *Eur. Phys. J. B* **89**, 244 (2016).
- [30] D. M. Kennes, E. Y. Wilner, D. R. Reichman, and A. J. Millis, Transient superconductivity from electronic squeezing of optically pumped phonons, *Nat. Phys.* **13**, 479 (2017).
- [31] M. A. Sentef, Light-enhanced electron-phonon coupling from nonlinear electron-phonon coupling, *Phys. Rev. B* **95**, 205111 (2017).
- [32] M. Kim, Y. Nomura, M. Ferrero, P. Seth, O. Parcollet, and A. Georges, Enhancing superconductivity in A₃C₆₀ fullerides, *Phys. Rev. B* **94**, 155152 (2016).
- [33] E. Pomarico, M. Mitrano, H. Bromberger, M. A. Sentef, A. Al-Temimy, C. Coletti, A. Stöhr, S. Link, U. Starke, C. Cacho, R. Chapman, E. Springate, A. Cavalleri, and I. Gierz, Enhanced electron-phonon coupling in graphene with periodically distorted lattice, *Phys. Rev. B* **95**, 024304 (2017).
- [34] X. Xu, M. Gullans, and J. M. Taylor, Quantum nonlinear optics near optomechanical instabilities, *Phys. Rev. A* **91**, 013818 (2015).

- [35] M.-A. Lemonde, N. Didier, and A. A. Clerk, Enhanced non-linear interactions in quantum optomechanics via mechanical amplification, *Nat. Commun.* **7**, 11338 (2016).
- [36] J. Stehlik, Y.-Y. Liu, C. Eichler, T. R. Hartke, X. Mi, M. J. Gullans, J. M. Taylor, and J. R. Petta, Double Quantum Dot Floquet Gain Medium, *Phys. Rev. X* **6**, 041027 (2016).
- [37] S. Zeytinoglu, A. Imamoglu, and S. Huber, Engineering Matter Interactions Using Squeezed Vacuum, *Phys. Rev. X* **7**, 021041 (2017).
- [38] D. J. Scalapino, J. R. Schrieffer, and J. W. Wilkins, Strong-coupling superconductivity. I, *Phys. Rev.* **148**, 263 (1966).
- [39] C. M. Varma, J. Zaanen, and K. Raghavachari, Superconductivity in the fullerenes, *Science* **254**, 989 (1991).
- [40] S. Fujita, K. Ito, and S. Godoy, *Quantum Theory of Conducting Matter: Superconductivity* (Springer, New York, 2010).
- [41] J. R. Schrieffer, *Theory of Superconductivity*, Advanced Book Program Series (Perseus, Cambridge, MA, 1983).
- [42] A. Polkovnikov, Phase space representation of quantum dynamics, *Ann. Phys. (NY)* **325**, 1790 (2010).
- [43] G. D. Mahan, *Many-particle Physics* (Springer, New York, 2013).
- [44] A. Sofroniou and S. Bishop, Dynamics of a parametrically excited system with two forcing terms, *Mathematics* **2**, 172 (2014).
- [45] H. Gunderson, H. Rigas, and F. S. VanVleck, A technique for determining stability regions for the damped mathieu equation, *SIAM J. Appl. Math.* **26**, 345 (1974).
- [46] J. Berges and J. Serreau, Parametric Resonance in Quantum Field Theory, *Phys. Rev. Lett.* **91**, 111601 (2003).
- [47] S. Engelsberg and J. R. Schrieffer, Coupled electron-phonon system, *Phys. Rev.* **131**, 993 (1963).
- [48] J. Rammer, *Quantum Field Theory of Nonequilibrium States* (Cambridge University Press, Cambridge, UK, 2007).
- [49] A. Georges, G. Kotliar, W. Krauth, and M. J. Rozenberg, Dynamical mean-field theory of strongly correlated fermion systems and the limit of infinite dimensions, *Rev. Mod. Phys.* **68**, 13 (1996).
- [50] J. K. Freericks, V. M. Turkowski, and V. Zlatić, Nonequilibrium Dynamical Mean-Field Theory, *Phys. Rev. Lett.* **97**, 266408 (2006).
- [51] S. Mallat, *A Wavelet Tour of Signal Processing* (Academic, New York, 1999).
- [52] H. J. Groenewold, On the principles of elementary quantum mechanics, *Physica (Amsterdam)* **12**, 405 (1946).
- [53] J. Moyal, Quantum mechanics as a statistical theory, in *Mathematical Proceedings of the Cambridge Philosophical Society* (Cambridge University Press, Cambridge, 1949), Vol. 45, pp. 99–124.
- [54] D. J. Thouless, Perturbation theory in statistical mechanics and the theory of superconductivity, *Ann. Phys. (NY)* **10**, 553 (1960).
- [55] M. Sentef, A. F. Kemper, B. Moritz, J. K. Freericks, Z.-X. Shen, and T. P. Devereaux, Examining Electron-Boson Coupling Using Time-Resolved Spectroscopy, *Phys. Rev. X* **3**, 041033 (2013).
- [56] Y. H. Wang, H. Steinberg, P. Jarillo-Herrero, and N. Gedik, Observation of floquet-bloch states on the surface of a topological insulator, *Science* **342**, 453 (2013).
- [57] T. W. B. Kibble, Some implications of a cosmological phase transition, *Phys. Rep.* **67**, 183 (1980).
- [58] W. H. Zurek, Cosmological experiments in condensed matter systems, *Phys. Rep.* **276**, 177 (1996).
- [59] E. Cappelluti, C. Grimaldi, L. Pietronero, S. Strässler, and G. A. Ummarino, Superconductivity of Rb_3C_{60} : Breakdown of the migdal-eliasberg theory, *Eur. Phys. J. B* **21**, 383 (2001).
- [60] P. Morel and P. W. Anderson, Calculation of the superconducting state parameters with retarded electron-phonon interaction, *Phys. Rev.* **125**, 1263 (1962).
- [61] J. Bauer, J. E. Han, and O. Gunnarsson, The theory of electron-phonon superconductivity: Does retardation really lead to a small coulomb pseudopotential? *J. Phys.: Condens. Matter* **24**, 492202 (2012).
- [62] R. Mankowsky, A. Subedi, M. Först, S. O. Mariager, M. Chollet, H. T. Lemke, J. S. Robinson, J. M. Glowia, M. P. Minitti, A. Frano *et al.*, Nonlinear lattice dynamics as a basis for enhanced superconductivity in $\text{YBa}_2\text{Cu}_3\text{O}_{6.5}$, *Nature (London)* **516**, 71 (2014).
- [63] Z. M. Raines, V. Stanev, and V. M. Galitski, Enhancement of superconductivity via periodic modulation in a three-dimensional model of cuprates, *Phys. Rev. B* **91**, 184506 (2015).
- [64] J.-i. Okamoto, A. Cavalleri, and L. Mathey, Theory of Enhanced Interlayer Tunneling in Optically Driven High- T_c Superconductors, *Phys. Rev. Lett.* **117**, 227001 (2016).
- [65] R. Höppner, B. Zhu, T. Rexin, A. Cavalleri, and L. Mathey, Redistribution of phase fluctuations in a periodically driven cuprate superconductor, *Phys. Rev. B* **91**, 104507 (2015).
- [66] J. Coulthard, S. R. Clark, S. Al-Assam, A. Cavalleri, and D. Jaksch, Enhancement of super-exchange pairing in the periodically-driven Hubbard model, [arXiv:1608.03964](https://arxiv.org/abs/1608.03964).
- [67] A. A. Patel and A. Eberlein, Light-induced enhancement of superconductivity via melting of competing bond-density wave order in underdoped cuprates, *Phys. Rev. B* **93**, 195139 (2016).
- [68] Y. Murakami, N. Tsuji, M. Eckstein, and P. Werner, Nonequilibrium steady states and transient dynamics of conventional superconductors under phonon driving, *Phys. Rev. B* **96**, 045125 (2017).
- [69] P. B. Allen, Theory of Thermal Relaxation of Electrons in Metals, *Phys. Rev. Lett.* **59**, 1460 (1987).
- [70] D. Semkat, D. Kremp, and M. Bonitz, Kadanoff-Baym equations with initial correlations, *Phys. Rev. E* **59**, 1557 (1999).